Distribution Agreement

In presenting this thesis or dissertation as a partial fulfillment of the requirements for an advanced degree from Emory University, I hereby grant to Emory University and its agents the non-exclusive license to archive, make accessible, and display my thesis or dissertation in whole or in part in all forms of media, now or hereafter known, including display on the world wide web. I understand that I may select some access restrictions as part of the online submission of this thesis or dissertation. I retain all ownership rights to the copyright of the thesis or dissertation. I also retain the right to use in future works (such as articles or books) all or part of this thesis or dissertation.

Signature:

_____ _____

Tao Jiang Date

Two-Dimensional Self-Assembly of Collagen-Mimetic Peptides

By

Tao Jiang
Doctor of Philosophy

Chemistry

_____
Dr. Vincent P. Conticello
Advisor

_____
Dr. Emily E. Weinert
Committee Member

_____
Dr. Stefan Lutz
Committee Member

Accepted:

_____
Lisa A. Tedesco, Ph.D.
Dean of the James T. Laney School of Graduate Studies

_____
Date

Two-Dimensional Self-Assembly of Collagen-Mimetic Peptides

By

Tao Jiang

B.S., Nanjing University, 2007

Advisor: Vincent P. Conticello, Ph.D.

An abstract of
A dissertation submitted to the Faculty of the
James T. Laney School of Graduate Studies of Emory University
in partial fulfillment of the requirements for the degree of
Doctor of Philosophy
in Chemistry
2015

Abstract

Two-Dimensional Self-Assembly of Collagen-Mimetic Peptides

By Tao Jiang

Peptide self-assembly has intrigued researchers for decades, as it offers a practical way for fabrication of biomaterials with defined structure and function. Challenge and opportunity still exist in this field where de novo peptide design cannot afford structures as sophisticated as natural ones in cells. This dissertation described the effort we have made in controlling self-assembly on scaffold of collagen-mimetic peptides.

We first demonstrated the design of two collagen-mimetic peptides, **NSI** and **NSII** comprising three sequential blocks with positive, neutral, and negative charges. Both peptides self-assembled into structurally defined sheets. Characterizations suggested a self-assembly mechanism that the triblock configuration enforced an anti-parallel alignment of collagen triple helices through complementary electrostatic interactions. Lateral extension and layered packing of triple helices afforded the two-dimensional assembly formation. A clear understanding of the underlying structures provided an attractive platform for fabrication of two-dimensional structures by mediating electrostatic interactions.

We then investigated the effects of positions and conformations of charged residues on self-assembly morphology. **NSIII** was described in this chapter, which self-assembled into monolayer sheets of uniform size and shape. It was proposed that the sequence change in **NSIII** introduced an energy penalty against Coulombic attraction energy among triple helices. The assembly force was balanced by the disassociation force, which resulted in the formation of small and uniform assemblies.

Finally, we presented a rational peptide design on the basis of the previous sheet model. Two asymmetric peptides, **CP**$^{+}$ and **CP**$^{-}$ were described that could form monolayer sheets with positive and negative surface charge, respectively. We took advantage of the difference in rates of assembly between **CP**$^{+}$ and **CP**$^{-}$, and grew **CP**$^{-}$ layers on faces of **CP**$^{+}$ sheets with the aid of electrostatic interactions. Using this strategy, we generated an ordered sandwich structure, with **CP**$^{+}$ sheet as core, buried by **CP**$^{-}$ layers. The results suggested an exciting possibility of building complex structures with compositional and structural control.

Two-Dimensional Self-Assembly of Collagen-Mimetic Peptides

By

Tao Jiang

B.S., Nanjing University, 2007

Advisor: Vincent P. Conticello, Ph.D.

A dissertation submitted to the Faculty of the
James T. Laney School of Graduate Studies of Emory University
in partial fulfillment of the requirements for the degree of
Doctor of Philosophy
in Chemistry
2015

ACKNOWLEDGEMENT

I would like to express my sincere gratitude to my advisor Dr. Vincent Conticello for his continuous support and guidance in my Ph.D study. He is intuitive, insightful, and impresses me with his immense knowledge. His enthusiasm for research and high standard in experiments will continue to influence me in my future career. I am incredibly lucky to have obtained training in his lab. I would like to earnestly thank my committee members Dr. Stefan Lutz and Dr. Emily Weinert for keeping track of my research progress. Their insightful comments and suggestions broaden my research perspective, and benefit my career development.

I am very grateful to the current members of Conticello's lab, Elizabeth Magnotti, Charles Modlin, Becky Bartlett, Spencer Hughes, Olivia Dhaliwal, and Lily Hough for making our lab like a family. Special thanks go to Elizabeth and Charles for help in proofreading. I also want to sincerely thank graduated colleagues, Dr. Melissa Patterson, Dr. Weilin Peng, Dr. I-Lin Wu, and Dr. Chunfu Xu, who taught me a lot when I joined the lab. From time to time, I still remember those early days when Weilin and I-lin introduced me skills for protein-based projects, and Chunfu trained me for peptide-based experiments. I want to acknowledge Dr. Yajing Lian and Dr. Aifang Li, who helped me in personal life when I arrived in Atlanta.

My sincere appreciation also goes to our collaborators, Dr. David Lynn, (Emory University), Dr. Anil Mehta (Emory University), Dr. Yonggang Ke (Emory University), Tianquan Lian (Emory University), Dr. Khalid Salaita, (Emory University), Dr. Elizabeth Wright (Emory University), Hong Yi (Emory University), Jeannette Taylor (Emory University) Dr. Zhigang Jiang (Georgia Institute of Technology), Dr. Ingeborg Schmidt-

Krey (Georgia Institute of Technology), Dr. Yury Chernoff (Georgia Institute of Technology), Dr. Xiaobing Zuo (Argonne National Laboratory), Dr. Joseph Wall (Brookhaven National Laboratory), Darrin Pochan (University of Delaware), Chaoying Ni (University of Delaware).

Last but not least, I would like to acknowledge my family members, my parents, my wife's parents, my wife, my son, and my daughter for their continuous support. My deepest gratitude goes to my wife, who devotes herself to the family, understands and encourages me all the time.

Table of Contents

List of Figures

List of Table

1 Introduction

1.1 Self-assembly in nature

Self-assembly defines a process in which monomers spontaneously organize into ordered patterns or structures through local interactions among the components, without outside instructions.[1] Self-assembly is ubiquitous in nature. At macroscopic scales, flocks of birds and schools of fishes often exhibit self-assembly behaviors to maximize the benefit of individuals.[2] Looking inside cells at microscopic scales, self-assembly underlies the basis of life, as a great number of cellular structures and functions arise from elaborated interactions between monomers through years of evolution. The study of self-assembly is thus of vital importance in understanding nature, and for de novo design of unnatural systems.[3]

With considerable advancement in molecular synthesis and manipulation, higher ordered architectures can be fabricated from diverse types of building blocks, ranging from small organic molecules to engineered proteins.[4-7] The resulting macrostructures or patterns in human designed assemblies provide attractive platforms for researchers to explore novel functions that cannot be achieved from individual monomers. Even though molecular self-assembly has been widely employed as one of the practical strategies in material synthesis and fabrication,[3] to date, synthetic systems still cannot reach the level of structural complexity in cells, which offers challenges and opportunities to researchers.

1.2 Molecular self-assembly using nature-inspired building blocks

Nature has an enormous variety of self-assembling systems, inspiring the fundamental studies of molecular recognition and interaction, and also spurring bottom-up fabrication using biopolymers. Polypeptides and polynucleotides represent attractive building blocks for fabricating ordered biomaterials, as the folding and assembling actions can be encoded within their primary sequences. Indeed, the elucidation of the Watson-Crick base pairing rules for DNA double-helix structures[8] has rendered DNA as a tractable design target. DNA helices have been widely exploited as a structural motif instead of as a message carrier. Many programmable assembly routes have been designed to direct DNA self-assembly into a wide range of one-, two-, and three-dimensional architectures with controlled shape and symmetry.[9-11] As one of the dominant methods,[11] DNA origami was first raised by Rothemund's group.[12] It provides a general way to create diverse structures from the folding of a single strand DNA scaffold, with the help of short staple strands. As for constructing polyhedra-like structures, Seeman's group first introduced a strategy that relies on DNA duplexes for polyhedral edges, and branched junctions for the vertices.[13] Yin's lab put forward a modular strategy that uses "DNA bricks" to construct structures.[14] Each "DNA brick" is equipped with one single strand as sticky ends. Designed structural morphology can be achieved by pairing the sticky ends of those modular components. The DNA structural engineering is a rapidly progressing field that provides benefits in many areas such as drug delivery and disease diagnosis.[15]

Using a similar strategy, the only reported protein polyhedra structure was achieved in Jerala's group.[16] It was fabricated from the folding of a single-chain polypeptide

containing coiled coil-forming domains for polyhedral edges, and flexible peptide hinges for polyhedral vertices. The diversity of amino acids and the sequence specificity of proteins and peptides makes these substrates excellent for exploration of structural complexities. However, compared to the straightforward base pairing mechanism in DNA, rational sequence design for order protein structures remains challenging. Weak nonconvalent interactions dominate in driving protein folding and assembly. The low energy interacting interfaces would generate multiple competing pathways, resulting in complex outcomes. Furthermore, researchers are still seeking a complete understanding on how multiple nonconvalent forces in proteins synergistically lead to discrete protein folding and assembly states.[17]

Recently, a more clear understanding has been gained about in vitro folding of short peptides.[17] Using a reductionist approach, synthetic peptides containing only structural motifs (such as sequences for α-helix, β-sheet) derived from natural proteins have been recruited as building units for fabrication of higher order structures.[17] The de novo peptide design process often employs those nature-inspired peptides, which follow the self-assembly pathways of their natural counterparts. It is also believed that in vitro chemical and physical modifications may allow molecular editing of peptides beyond nature's capability, which may drive the peptide assembly into architectures never found in nature. In this dissertation, we presented investigations into controlled self-assembly behaviors of synthetic peptides derived from native collagen proteins.

1.3 Collagen-mimetic peptides

As the most abundant protein in mammals (more than 25%), collagen constitutes a big protein family. To date, different supramolecular morphologies have been identified in 28 types of collagen.[18-20] For example, fibrillar collagens (type I, II, and III) are primarily observed in connective tissues, and network-forming collagens (type IV and VIII) are prevalent in the extracellular matrix (ECM). The most distinct feature about collagen is that they share a triple helix secondary structure. The homotrimeric or heterotrimeric right-handed triple helix is formed by intertwining three collagen strands along the direction of strand axis. Each strand is staggered by one residue, and the individual strands adopt a left-handed polyproline II-type conformation.[21] A stable triple helix requires a tight packing between polypeptide strands, which is promoted by an invariant periodic triplet of Xaa-Yaa-Gly in the primary sequence.[19] For the amino acids at the Xaa and Yaa postions, the most common ones in nature are proline (Pro) for Xaa and (2S, 4R)-4-hydroxylproline (Hyp) for Yaa.[22] Structure studies indicated that proline and its derivatives have two pyrrolidine ring conformations, termed C^{γ}-exo and C^{γ}-endo puckers. The Pro at the Xaa positions of collagen triads favors the C^{γ}-endo pucker, while the Hyp at the Yaa positions adopts a C^{γ}-exo pucker.[23]

In recent years, synthetic collagen-mimetic peptides containing Pro-Hyp-Gly repeating triads are emerging as an important model for study of collagen triple helical structures and thermal stabilities.[19,20] Single crystals of collagen-mimetic peptides displayed interstrand hydrogen bonds between the glycine amino group N-H and the Xaa carbonyl O=C, which provide the major force to hold the triple helix together.[21] Crystal analysis of proline-rich collagen-mimetic peptides suggested that the triple helical structure

has a 7/2 symmetry (seven triads in two turns) with a 20 Å axial repeat.[24] The structure of proline-poor collagen sequences were found to prefer a 10/3 symmetry (ten triads in three turns) with a 28.6 Å axial repeat.[25]

The thermal stability of collagen-mimetic peptides were found to depend on the repeating number of triads and the composition of residues at the Xaa and Yaa positions. Peptides comprising more Pro-Hyp-Gly triads had higher melting temperatures compared to shorter peptides.[20] Influence of amino acids combinations for the Xaa andYaa positions on peptide thermal stability has been extensively investigated in Brodsky's lab.[26,27] Mutations at the Xaa-Yaa positions of peptides using natural amino acids destabilized the triple helix stability to different extents, compared to the canonical Pro-Hyp-Gly triads. Furthermore, it has long been hypothesized that higher content of Hyp at the Yaa positions correlates with a more stable triple helix. It was observed in crystals that the hydroxyl group of Hyp is involved in intra-strand and inter-strand "water bridges", which contributes to the enhanced thermal stability.[21,28] Another interpretation is that the stereoelectronic properties of Hyp stabilize the trans peptide bond and favor a C^{γ}-exo pucker, which are more structurally favorable in the triple helix structure.[29]

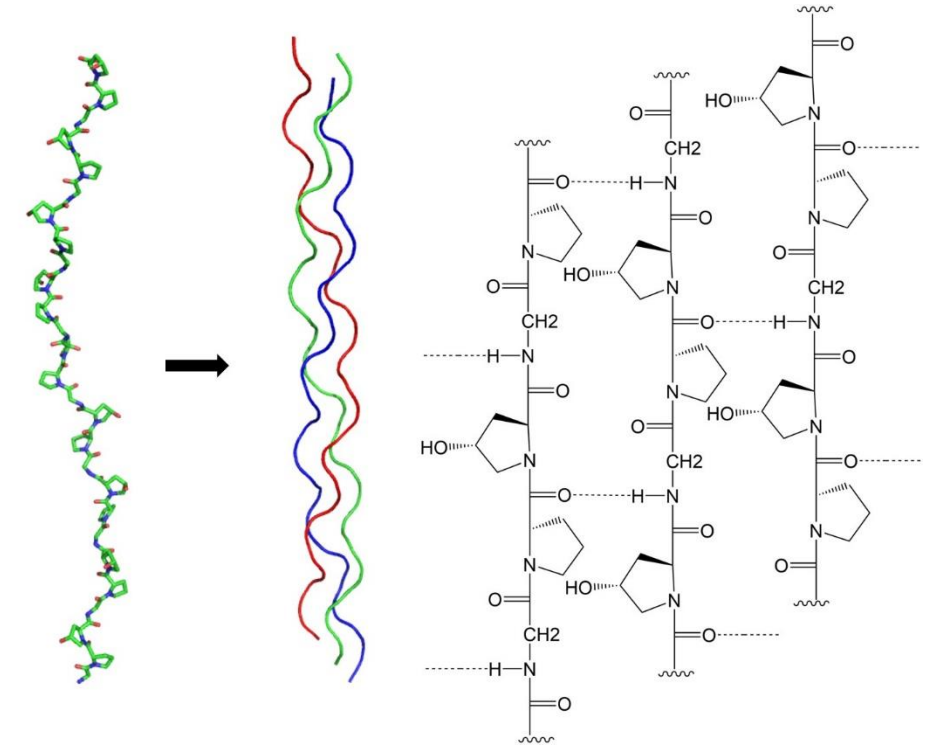

Figure 1.1 Collagen triple helix from (Gly-Pro-Hyp)$_9$, (Protein Data Bank entry 3B0S from ref.[24]) and inter-molecular hydrogen bonds within staggered strands.

1.4 Supramolecular assembly of collagen-mimetic peptides

Collagens extracted from animal tissues have been widely utilized for construction of biomaterials for food and medical industries.[30] However, the difficulty of specific chemical modification, the larger variation in protein composition from natural sources, and the potential risk of impurities in process of tissue extractions limit natural collagen's utility. In this regard, self-assembly of low-cost and simple synthetic collagen-mimetic peptides offers an alternative option.[19,20,31] In this introductory chapter, several representative strategies for construction of ordered assemblies using collagen-mimetic peptides were described.

The first investigation into self-assembly of collagen-mimetic peptides comprising only Pro-Hyp-Gly triads was performed by Brodsky's group.[32] At a temperature slightly below the melting temperature of the triple helix, $(Pro\text{-}Hyp\text{-}Gly)_{10}$ self-associated into branched fibrillar structures. It was proposed that at higher temperature, structured water shell around individual triple helices became more flexible (Figure 1.2 N to I), which allowed for formation of hybrid hydration layers between adjacent triple helices (Figure 1.2 I to A), and thus drove the self-assembly of peptides. Fibrils with uniform diameters were also obtained in the same lab by replacing triads in the middle of $(Pro\text{-}Hyp\text{-}Gly)_{10}$.with Hyp-rich sequences, derived from type IV collagens.[33] The results indicate that Pro-Hyp-Gly repeating triads can be enough to afford higher order one-dimensional assemblies.

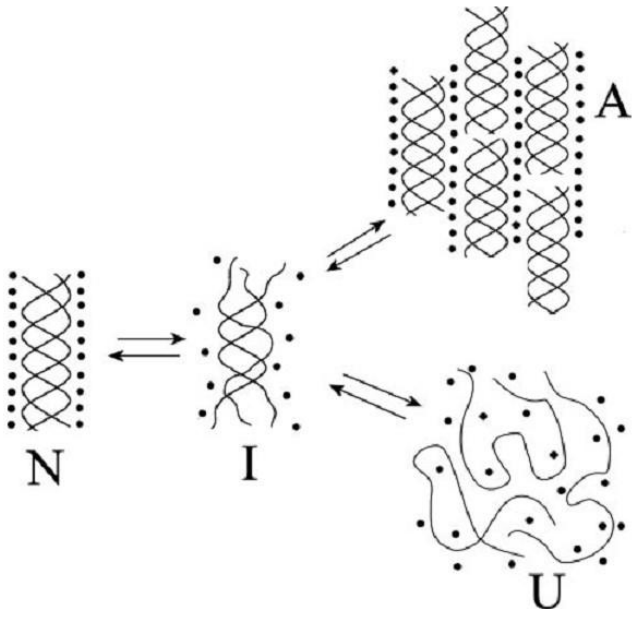

Figure 1.2 The self-assembly process of $(Pro\text{-}Hyp\text{-}Gly)_{10}$. Reprinted with permission from ref. [32] Copyright © 2006, by the American Society for Biochemistry and Molecular Biology

Raine's group reported a different strategy for fibril formation.[34] Two pairs of disulfide bonds were introduced to link two types of Pro-Hyp-Gly repeating peptides into a triple helix. Cysteines were positioned in a specific way that enforced a "Y-shaped" staggered alignment of peptides. (Figure 1.3A) The resulting "sticky-ended" configuration was believed to guide protomer elongation along the helical axis in a head-to-tail fashion, which was stabilized by side-associations between Pro-Hyp-Gly triads. (Figure 1.3B) The tethered peptides self-assembled into long fibrils that could go beyond the length of natural collagen fibers (400 nm here versus 300 nm for native collagen fibers). The diameters of synthetic collagen fibrils were measured to range from 0.5 to 1 nm, which were close to values for native collagen helices. A similar strategy was also reported by Koide's lab.[35] Inter-peptide disulfide bonds were employed to manipulate the registry of the triple helical strands. The resultant triple helix resembles a set of stairs. The proposed head-to-tail assembly among triple helices led the peptides to form aggregates at high concentrations. A later sequence modification with hydrophilic residues (arginine) added to the C-terminus led to hydrogel formation.[36] The results implied that complementary "step-shaped" peptides may adopt a different self-assembly mechanism compared to the "Y-shaped" peptides [34]. The feasibility of bridging heterotrimeric helices using cysteine knots make it possible to modulate the spatial distribution of amino acids in peptides. Recently, Koide's lab reported an arginine-rich heterotrimeric collagen helix.[37] Unlike homotrimers that place residues in symmetry, arginines in the heterotrimeric helix could be positioned on one side of the triple helix. We believe that asymmetric distributions of residues on triple helices would expand our design toolbox for higher order self-assembly.

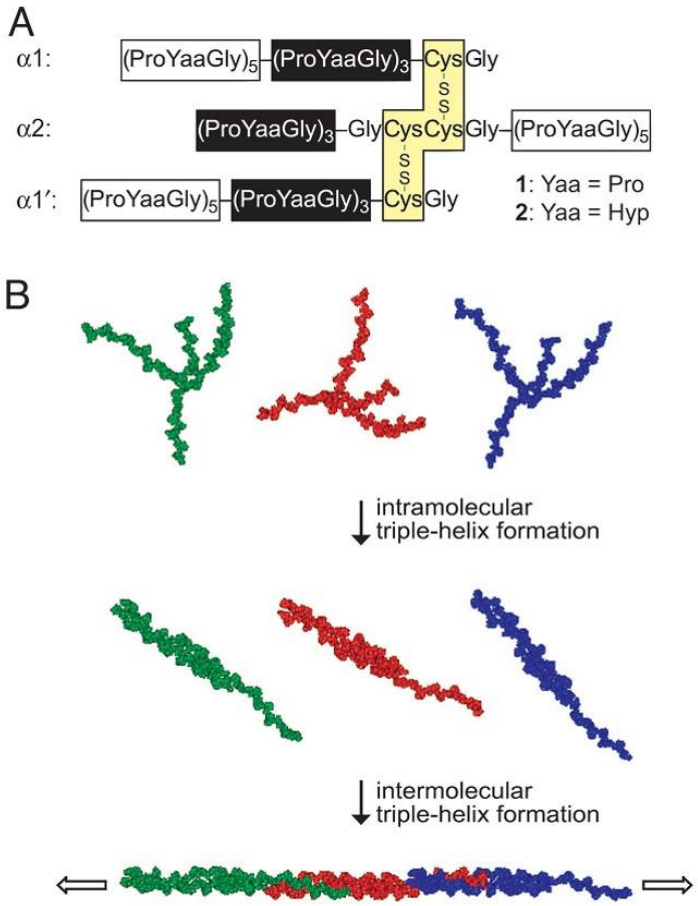

Figure 1.3 (A) Sequence of the sticky-ended collagen triple helix. (B) the proposed head-to-tail elongation. Reprinted with permission from ref. [34] Copyright (2006) National Academy of Sciences, U.S.A.

Metal ions has been exploited to template the association of collagen-mimetic peptides into versatile architectures.[38-45] Metal-ligand interactions were employed to drive intermolecular associations, and maintain metal coordination geometric arrangements. Chmielewski's lab introduced the bipyridyl (byp) group to a residue side chain within the central triad of a Pro-Hyp-Gly repeating peptide.[38] They relied on the byp-Fe(II) coordination to guide side-by-side associations of the peptide. (Figure 1.4) Incubating the peptide with Fe(II) lead to formation of fibrils. Peptide sequences with two

or three byp insertions were further investigated, which resulted in formation of disk [41] or vesicle [44] structures. Furthermore, the Chmielewski [39,40,42] and Horng [45] labs generated a series of collagen-mimetic peptides with histidine and nitrilotriacetic acid (NTA) at the ends, which also generated ordered structures due to metal ion induced end-to-end interactions. Indeed, employing metal coordination to template peptide self-assembly provides superior driving energy compared to other noncovalent forces.[46,47] Because of the prevalence of metal ions in biological samples and their redox properties, the metal-peptide self-assembly approach may serve as an interesting tool to design in vivo stimulus-responsive complex or metalloenzymes based on collagen scaffolds.

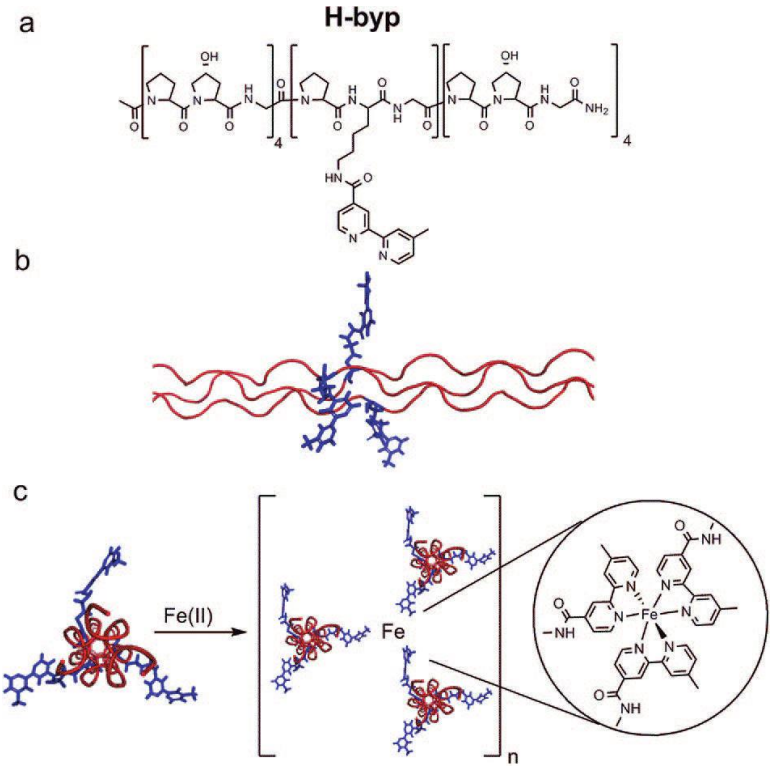

Figure 1.4 (A) The sequence of the byp modified collagen-mimetic peptide. (B) (C) The proposed lateral association of peptides induced by metal ions. Reprinted with permission from ref. [38] Copyright © 2008, American Chemical Society

Maryanoff's group employed aromatic interactions to dictate fibril formation. [48,49] Phenylalanine and pentafluorophenylalanine were added to the C- and the N-terminus of a collagen-mimetic peptide respectively. π-π stacking pair of pentafluorophenyl/phenyl ligands was speculated to induce a head-to-tail association among triple helices. The peptide formed microfibrils with a banded pattern. The diameter and length of fibrils were larger than the ones for individual triple helices, (fibrils were micrometers in length and around 250 nm in diameter), which implied that the self-assembly occurred at both axial and lateral directions. The peptide was capable of activating platelet aggregation, which mimicked natural collagen's thrombogenic properties.[49] A similar strategy was also reported in Horng's studies.[50] Arginine and phenylalanine were attached to the N- and the C- terminus of a collagen-mimetic peptide. End-to-end cation/π interactions from the pair of arginine/phenylalanine resulted in fibril formation. Brodsky's group studied a short collagen sequence flanked by an aromatic residue (tyrosine) at one terminus [33], or aromatic residues (tyrosine or phenylalanine) at each terminus [51]. Microfibrils were formed from both peptides without observing the banding feature, as in Maryanoff's assemblies [48,49]. It was proposed that CH-π interactions between aromatic residues at the end of peptides and imino acids within adjacent peptides drive lateral association, while end-to-end aromatic interactions promoted axial associations. (Figure 1.5) Due to the abundant imino acids within collagen peptides, CH-π interactions were nonspecific. Therefore, highly ordered peptide packing within the fibrils was precluded, and the banded feature was not observed.[51]

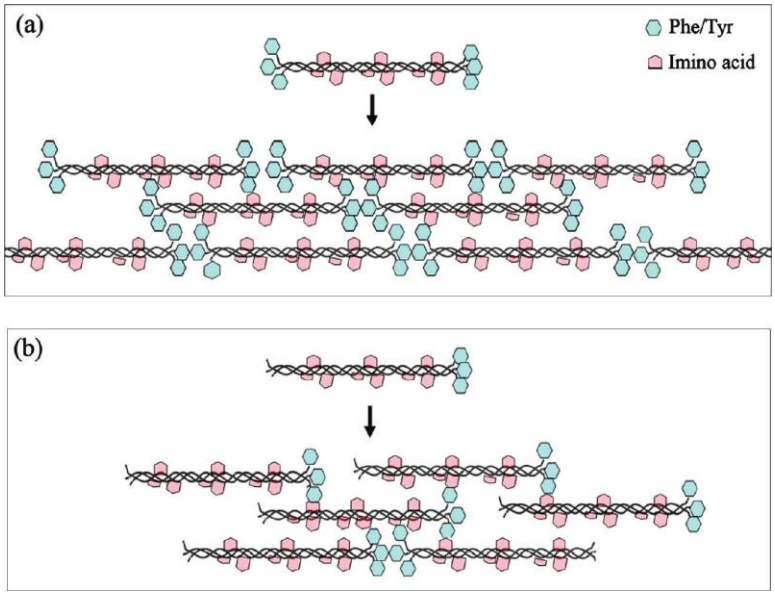

Figure 1.5 The proposed associations among (A) the triple helices with aromatic residues (tyrosine and phenylalanineone) attached to each terminus of the peptide, and (B) the triple helices containing one aromatic reside (tyrosine) at the C-terminus of peptides. Reprinted with permission from ref. [51] Copyright © 2009, American Chemical Society

Nanda's lab explored the use of hydrophobic interactions for peptide self-assembly.[52] Within a Pro-Hyp-Gly repeating triads, leucine and isoleucine were incorporated to afford an overall hydrophilic/hydrophobic/hydrophilic block configuration. Disc-like structures were formed, with thickness close to peptide length. When increasing the length of the hydrophobic domain, the morphology of peptide assemblies changed from disc to fibril. Computer simulation suggested that the disc was assembled from side-by-side association of triple helices, primarily through hydrophobic interactions. (Figure 1.6A) The fibril-like structure (helical tape) was formed by lateral triple helix packing with an angle. (Figure 1.6A) In both structures, hydrophobic regions were buried inside, and only exposed to solvents at ends of fibrils and edges of discs. As a result, mixing discs and fibrils

resulted in “nanostar” formation due to hydrophobic interactions between different shapes. (Figure 1.6A) The same group also applied the ridges-in-grooves packing mechanism [53] to self-assembly of collagen peptides.[54] The $[(_{L}P_{L}PG)_{10}]_3$ peptide from levorotatory isomers and the $[(_{D}P_{D}PG)_{10}]_3$ peptide that contain dextrorotatory isomers had the opposite helical handedness. The opposite-handed helical shapes functioned as complementary interfaces for tighter packing between L- and D-trimers over LL- and DD- ones. Lamellar structures were obtained from the mixture of L- and D- peptides, while no higher order assemblies was observed from L- or D-peptide only solutions.[54] (Figure 1.6 B)

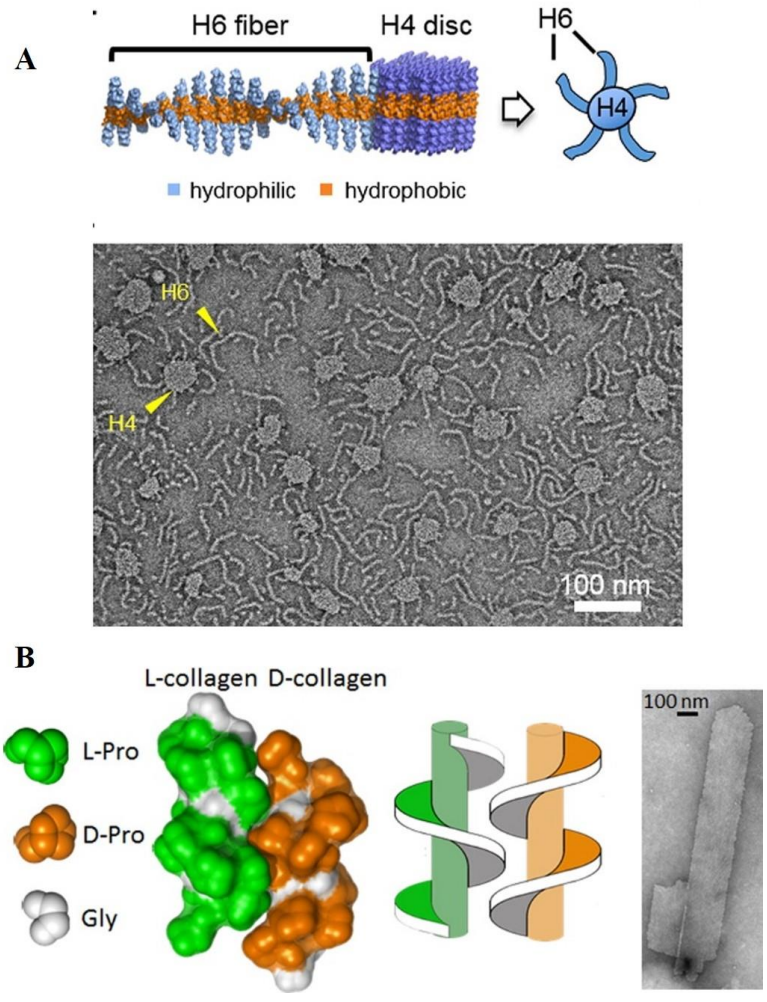

Figure 1.6 Proposed models and TEM images for (A) disc, fibril, and nanostar structures and (B) the complementary packing between left- and right-handed screws. Reprinted with permission from ref. [52,54] Copyright © 2013&2014, American Chemical Society

Charged residues are often present at both Xaa and Yaa positions in natural collagens [55], which motivated researchers to investigate the roles of electrostatic interactions in collagen structures and functions [56-59]. Conticello's group recruited Coulombic interactions to guide self-assembly of a collagen-mimetic peptide into banded fibrils [60], reminiscent of type I collagen fibers with D-periodicity (Figure 1.7) [19]. The periodic banding pattern of natural type I collagen fibers (termed D-periodicity) stems from the staggering of triple helices. (Figure 1.7) The helices are staggered from each other by 67 nm, which results in an overlap region comprising five triple helices and a gap region containing four helices.[19] D-periodicity requires highly ordered internal packing, which was first achieved in vitro using a triblock collagen-mimetic peptide in Conticello's group.[60] (Figure 1.8) Pro-Arg-Gly and Glu-Hyp-Gly triads were measured to have the greatest thermal stabilities among Pro-Yaa-Gly and Xaa-Hyp-Gly repeats.[26] A collagen-mimetic peptide was then designed with a central Pro-Hyp-Gly block flanked by a positively charged block comprising arginine at the Yaa position and a negatively charged domain containing glutamic acid at the Xaa position. In a collagen fiber forming buffer (ionic strength 0.225), banded microfibrils were observed in solution after annealing, with a D-periodicity of 18 nm.[60] Hartgerink's group reported nanofibril and hydrogel formation from a similar sequence, comprising a pair of lysine/asparagine instead of arginine/glutamic acid. Inter-peptide lysine/asparagine charged pairs were more efficient in generating sticky-ended triple helix, and lead to formation of fibrils and hydrogels.[61]

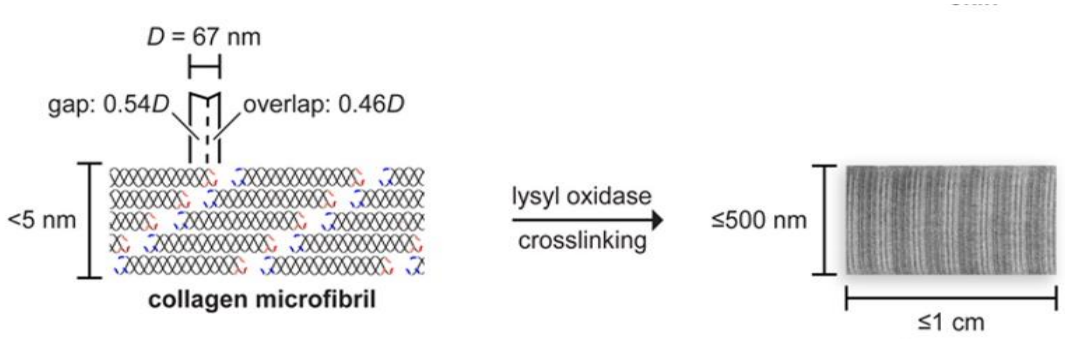

Figure 1.7 The process of collagen assembly into fibers with D-periodicity. Reprinted with permission from ref. [19] Copyright © 2009, Annual Reviews

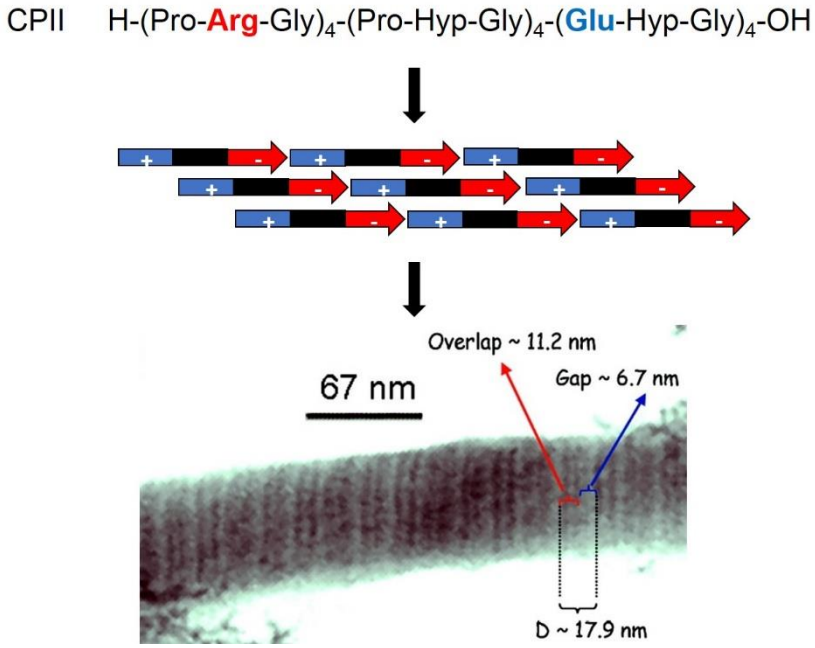

Figure 1.8 The proposed axial alignment among peptides through complementary electrostatic interactions, and the observed banded feature of fibrils under TEM. Reprinted with permission from ref. [60] Copyright © 2007, American Chemical Society

1.5 Summary

Self-assembly is everywhere in nature. Molecular self-assembly represents a practical strategy for synthesis and fabrication of complex architectures. Challenges and opportunities still exist in the field where many natural self-assembly mechanisms are still not clear, and de novo design of bottom-up assemblies cannot afford structures as sophisticated as biomachines in living cells. Due to the well-studied collagen sequence features and a clear understanding of sequence-structure relationships, collagen-mimetic peptides comprising triple helical structural motifs are promising substrates for the construction of collagen-based biomaterials. In this introductive section, we summarized several representative strategies reported over the last decade, for fabrication of supramolecular assemblies. Disulfide bond formation, metal ion coordination, aromatic interaction, hydrophobic interaction, and electrostatic interaction have been employed to fabricate higher order structures. Versatile morphologies have been achieved in test tubes, such as vesicles, fibrils, discs, and hydrogels.

However, several challenges are currently limiting the expansion of this field. Many reported designs defined intermolecular interactions, from which the self-assembly pathway and outcome were unpredictable and uncontrollable. Moreover, most structures were assembled from single peptides, contrasting the multi-component assemblies found in cells. Those challenges are driving researchers to develop approaches that aim to construct complex and predictable peptide arrangements. The following chapters demonstrated the efforts we have made in manipulating recognition and interaction among collagen-mimetic peptides, which endowed us with structural and compositional control over two-dimensional peptide self-assembly.

1.6 Reference

(1) Whitesides, G. M.; Boncheva, M. *Proc. Natl. Acad. Sci. U. S. A.* **2002**, *99*, 4769-4774.

(2) Zhang, S.; Yokoi, H.; Zhao, X. In *Biomimetics: Biologically Inspired Technologies*; Bar-Cohen, Y., Ed.; CRC Press: Boca Raton, 2006, p 229-240.

(3) Whitesides, G. M.; Grzybowski, B. *Science* **2002**, *295*, 2418-2421.

(4) Thorkelsson, K.; Bai, P.; Xu, T. *Nano Today* **2015**, *10*, 48-66.

(5) Boekhoven, J.; Stupp, S. I. *Adv. Mater.* **2014**, *26*, 1642-1659.

(6) Chakrabarty, R.; Mukherjee, P. S.; Stang, P. J. *Chem. Rev.* **2011**, *111*, 6810-6918.

(7) Fegan, A.; White, B.; Carlson, J. C.; Wagner, C. R. *Chem. Rev.* **2010**, *110*, 3315-3336.

(8) Watson, J. D.; Crick, F. H. C. *Nature* **1953**, *171*, 737-738.

(9) Seeman, N. C. *Trends Biotechnol.* **1999**, *17*, 437-443.

(10) Linko, V.; Dietz, H. *Curr. Opin. Biotechnol.* **2013**, *24*, 555-561.

(11) Ke, Y. *Curr. Opin. Struct. Biol.* **2014**, *27*, 122-128.

(12) Rothemund, P. W. *Nature* **2006**, *440*, 297-302.

(13) Chen, J. H.; Seeman, N. C. *Nature* **1991**, *350*, 631-633.

(14) Wei, B.; Dai, M.; Yin, P. *Nature* **2012**, *485*, 623-626.

(15) Service, R. F. *Science* **2011**, *332*, 1140-1141, 1143.

(16) Gradisar, H.; Bozic, S.; Doles, T.; Vengust, D.; Hafner-Bratkovic, I.; Mertelj, A.; Webb, B.; Sali, A.; Klavzar, S.; Jerala, R. *Nat. Chem. Biol.* **2013**, *9*, 362-366.

(17) Boyle, A. L.; Woolfson, D. N. *Chem. Soc. Rev.* **2011**, *40*, 4295-4306.

(18) Brinckmann, J. *Collagen* **2005**, *247*, 1-6.

(19) Shoulders, M. D.; Raines, R. T. *Annu. Rev. Biochem.* **2009**, *78*, 929-958.

(20) Yu, S. M.; Li, Y.; Kim, D. *Soft Matter.* **2011**, *7*, 7927-7938.

(21) Bella, J.; Eaton, M.; Brodsky, B.; Berman, H. M. *Science* **1994**, *266*, 75-81.

(22) Ramshaw, J. A.; Shah, N. K.; Brodsky, B. *J. Struct. Biol.* **1998**, *122*, 86-91.

(23) Fraser, R. D.; MacRae, T. P.; Suzuki, E. *J. Mol. Biol.* **1979**, *129*, 463-481.

(24) Okuyama, K.; Miyama, K.; Mizuno, K.; Bachinger, H. P. *Biopolymers* **2012**, *97*, 607-616.

(25) Boudko, S. P.; Engel, J.; Okuyama, K.; Mizuno, K.; Bachinger, H. P.; Schumacher, M. A. *J. Biol. Chem.* **2008**, *283*, 32580-32589.

(26) Persikov, A. V.; Ramshaw, J. A.; Brodsky, B. *J. Biol. Chem.* **2005**, *280*, 19343-19349.

(27) Persikov, A. V.; Ramshaw, J. A.; Kirkpatrick, A.; Brodsky, B. *Biochemistry* **2005**, *44*, 1414-1422.

(28) Gustavson, K. H. *Nature* **1955**, *175*, 70-74.

(29) Bretscher, L. E.; Jenkins, C. L.; Taylor, K. M.; DeRider, M. L.; Raines, R. T. *J. Am. Chem. Soc.* **2001**, *123*, 777-778.

(30) Stenzel, K. H.; Miyata, T.; Rubin, A. L. *Annu. Rev. Biophys. Bio.* **1974**, *3*, 231-253.

(31) Koide, T. *Connect. Tissue Res.* **2005**, *46*, 131-141.

(32) Kar, K.; Amin, P.; Bryan, M. A.; Persikov, A. V.; Mohs, A.; Wang, Y. H.; Brodsky, B. *J. Biol. Chem.* **2006**, *281*, 33283-33290.

(33) Kar, K.; Wang, Y.-H.; Brodsky, B. *Protein Sci.* **2008**, *17*, 1086-1095.

(34) Kotch, F. W.; Raines, R. T. *Proc. Natl. Acad. Sci. U. S. A.* **2006**, *103*, 3028-3033.

(35) Koide, T.; Homma, D. L.; Asada, S.; Kitagawa, K. *Bioorg. Med. Chem. Lett.* **2005**, *15*, 5230-5233.

(36) Yamazaki, C. M.; Asada, S.; Kitagawa, K.; Koide, T. *Biopolymers* **2008**, *90*, 816-823.

(37) Yamazaki, C. M.; Nakase, I.; Endo, H.; Kishimoto, S.; Mashiyama, Y.; Masuda, R.; Futaki, S.; Koide, T. *Angew. Chem., Int. Ed.* **2013**.

(38) Przybyla, D. E.; Chmielewski, J. *J. Am. Chem. Soc.* **2008**, *130*, 12610-12611.

(39) Pires, M. M.; Chmielewski, J. *J. Am. Chem. Soc.* **2009**, *131*, 2706-2712.

(40) Pires, M. M.; Przybyla, D. E.; Chmielewski, J. *Angew. Chem., Int. Ed.* **2009**, *48*, 7813-7817.

(41) Przybyla, D. E.; Chmielewski, J. *J. Am. Chem. Soc.* **2010**, *132*, 7866-7867.

(42) Pires, M. M.; Przybyla, D. E.; Perez, C. M. R.; Chmielewski, J. *J. Am. Chem. Soc.* **2011**, *133*, 14469-14471.

(43) Pires, M. M.; Lee, J.; Ernenwein, D.; Chmielewski, J. *Langmuir* **2012**, *28*, 1993-1997.

(44) Przybyla, D. E.; Rubert Perez, C. M.; Gleaton, J.; Nandwana, V.; Chmielewski, J. *J. Am. Chem. Soc.* **2013**, *135*, 3418-3422.

(45) Hsu, W.; Chen, Y.-L.; Horng, J.-C. *Langmuir* **2012**, *28*, 3194-3199.

(46) Sontz, P. A.; Song, W. J.; Tezcan, F. A. *Curr. Opin. Chem. Biol.* **2014**, *19*, 42-49.

(47) Song, W. J.; Sontz, P. A.; Ambroggio, X. I.; Tezcan, F. A. *Annu. Rev. Biophys.* **2014**, *43*, 409-431.

(48) Cejas, M. A.; Kinney, W. A.; Chen, C.; Leo, G. C.; Tounge, B. A.; Vinter, J. G.; Joshi, P. P.; Maryanoff, B. E. *J. Am. Chem. Soc.* **2007**, *129*, 2202-2203.

(49) Cejas, M. A.; Kinnney, W. A.; Chen, C.; Vinter, J. G.; Almond, H. R.; Balss, K. M.; Maryanoff, C. A.; Schmidt, U.; Breslav, M.; Mahan, A.; Lacy, E.; Maryanoff, B. E. *Proc. Natl. Acad. Sci. U. S. A.* **2008**, *105*, 8513-8518.

(50) Chen, C. C.; Hsu, W.; Kao, T. C.; Horng, J. C. *Biochemistry* **2011**, *50*, 2381-2383.

(51) Kar, K.; Ibrar, S.; Nanda, V.; Getz, T. M.; Kunapuli, S. P.; Brodsky, B. *Biochemistry* **2009**, *48*, 7959-7968.

(52) McGuinness, K.; Khan, I. J.; Nanda, V. *ACS Nano* **2014**, *8*, 12514-12523.

(53) Nanda, V.; DeGrado, W. F. *J. Am. Chem. Soc.* **2006**, *128*, 809-816.

(54) Xu, F.; Khan, I. J.; McGuinness, K.; Parmar, A. S.; Silva, T.; Murthy, N. S.; Nanda, V. *J. Am. Chem. Soc.* **2013**, *135*, 18762-18765.

(55) Hulmes, D. J.; Miller, A.; Parry, D. A.; Piez, K. A.; Woodhead-Galloway, J. *J. Mol. Biol.* **1973**, *79*, 137-148.

(56) Fallas, J. A.; O'Leary, L. E. R.; Hartgerink, J. D. *Chem. Soc. Rev.* **2010**, *39*, 3510-3527.

(57) Xu, F.; Zhang, L.; Koder, R. L.; Nanda, V. *Biochemistry* **2010**, *49*, 2307-2316.

(58) Persikov, A. V.; Ramshaw, J. A. M.; Kirkpatrick, A.; Brodsky, B. *J. Mol. Biol.* **2002**, *316*, 385-394.

(59) Fallas, J. A.; Hartgerink, J. D. *Nat. Commun.* **2012**, *3*, 1087.

(60) Rele, S.; Song, Y. H.; Apkarian, R. P.; Qu, Z.; Conticello, V. P.; Chaikof, E. L. *J. Am. Chem. Soc.* **2007**, *129*, 14780-14787.

(61) O'Leary, L. E.; Fallas, J. A.; Bakota, E. L.; Kang, M. K.; Hartgerink, J. D. *Nat. Chem.* **2011**, *3*, 821-828.

2 Structurally defined nano-scale sheets from self-assembly of collagen-mimetic peptides

2.1 Introduction

Nanosheets, i.e., two-dimensional (2D) nanoscale assemblies, bridge an important intellectual and physical gap between low-dimensional assemblies (such as nanoparticles, nanofibers, nanotubes, and nanoribbons) and extended three-dimensional structures (such as crystalline solids). The controlled fabrication of two-dimensional assemblies on the nanoscale presents a significant challenge to current synthetic methods. Nonetheless, the development of effective strategies for the creation of 2D assemblies is essential to the success of the emergent field of 2D nanoarchitectonics,[1,2] in which chemical and physical principles are applied to engineer nanosheet structures for integration into functional devices.

The molecularly programmed self-assembly of sequence defined peptides offers significant promise for the fabrication of 2D nanoarchitectonics. Peptides have a high density of chemical functionality that can be arranged within a defined macromolecular architecture. This molecular level information can be utilized within a given structural context to direct highly specific intra- and inter-molecular interactions that promote self-assembly of thermodynamically stable and structurally defined 2D assemblies. Despite these advantages, the design of peptide-based two-dimensional assemblies has been limited

to structures derived from short linear[3,4] or cyclic peptide sequences[5] in which the intrinsic conformational properties of the polypeptide backbone have not been utilized as an explicit design principle. However, recent reports from Zuckermann, et al.,[6,7] on the controlled fabrication of nanosheets from self-assembly of a sequence-defined peptoid oligomers suggest that this approach has merit, particularly if a stable conformational state of the peptide sequence can geometrically promote specific intermolecular interactions within a two-dimensional assembly.

Collagen-mimetic peptides were selected as a substrate for the design of two-dimensional peptide-based assemblies. Whereas native collagen isoforms display a wide range of morphologies, the formation of 2D assemblies is an uncommon occurrence limited to in vitro conditions.[8-12] In order to bias self-assembly of collagen-mimetic peptides toward formation of layered collagen structures, methods must be developed to control registry between chains in a triple helix and between adjacent triple helices in supramolecular assemblies. However, despite recent progress, the sequence-structure correlations that determine the differences in structural hierarchy between native collagen isoforms are not well understood at the molecular level.

Previous researchers have demonstrated that introduction of structural modifications into collagen-mimetic peptides can recapitulate the complex modes of native collagen assembly. Metal ion coordination,[13-18] π-π interaction,[19,20] CH-π interaction,[21] cation-π interaction,[22] and disulfide bond formation[23-25] have been employed to direct higher order assembly of collagen-mimetic peptides into supramolecular structures including fibers, disks, networks, and spherical assemblies. However, the mode of assembly has been difficult to reliably predict from consideration of

the initial peptide sequence, such that the resultant assemblies usually do not exhibit the high degree of order implicit within the structural hierarchy of native collagen isoforms.

2.2 Collagen nanosheet sequences design

Previously, we employed sequence-encoded electrostatic interactions to enforce alignment of a designed collagen-mimetic peptide, **CPII**, into uniaxially oriented fibrils (Figure 2.1).[26] The design of peptide **CPII** comprised a symmetric sequence of three blocks of four triads, in which the triad sequence within each block encompassed different electrostatic properties. This block architecture was designed to promote a staggered alignment of peptides within a triple helical conformation in order to drive fibrillization through charge complementation (Figure 2.1C). The **CPII** peptide was observed to self-assemble into fibrils that mimicked the banded, D periodic ultrastructure of native collagen fibers.[27,28] However, the desired structural alignment was difficult to control under the extensive range of experimental conditions that were investigated for this peptide system. Hartgerink and coworkers, based on an extensive structural analysis of electrostatic interactions within collagen-mimetic peptides,[29-31] designed a derivative of **CPII** in which conservative substitutions of Asp for Glu and Lys for Arg were incorporated into the peptide sequence (Figure 2.1A).[32] This second generation peptide underwent multi-hierarchical self-assembly under a wide range of experimental conditions to afford collagen-based hydrogels composed of laterally associated peptide fibrils.

While fibrillar morphologies have been the predominant species observed thus far from self-assembly of **CPII**-like peptides, two-dimensional assemblies are not necessarily precluded based on the initial sequence design (Figure 2.1D). Indeed, the formation of

irregular sheet-like structures was occasionally observed from buffered aqueous solutions of **CPII** at near neutral pH. Two sequence variants of the **CPII** peptide, **NSI** and **NSII**, were designed in order to bias self-assembly toward formation of two-dimensional layered assemblies through incorporation of structural features to promote selective interaction between triple helices.

The sequences of peptides **NSI** and **NSII** were based on the original design of **CPII** in that the pattern of positively and negatively charged amino acid residues was maintained to ensure charge complementarity.[26] However, in order to direct the Coulombic interactions between triple helices, the positively charged arginine residues in the first four triads of **CPII** were replaced with the non-canonical imino acid, (2S, 4R)-4-aminoproline (Amp) (Figure 2.1B).[33,34] The stereoelectronic properties of Amp residue mirror those of the canonical (2S, 4R)-4-hydroxyproline (Hyp) residue, in that the pyrrolidine ring adopts a C^{γ} exo ring pucker conformation.[35-39] Crystallographic analyses of collagen structures have demonstrated that the C^{γ} exo ring pucker is the most common conformation for imino acid residues at Yaa positions within the triple helix.[40-42] The sequence of **NSI** is a direct structural analogue of the parent peptide **CPII**, while the sequence of **NSII** differs in that the central block of canonical (Pro-Hyp-Gly) triads was lengthened to seven repeats. Since peptide **NSII** no longer mimics the symmetric triblock architecture of **CPII**, it should not be competent for staggered assembly into one-dimensional fibrils (Figure 2.1C).

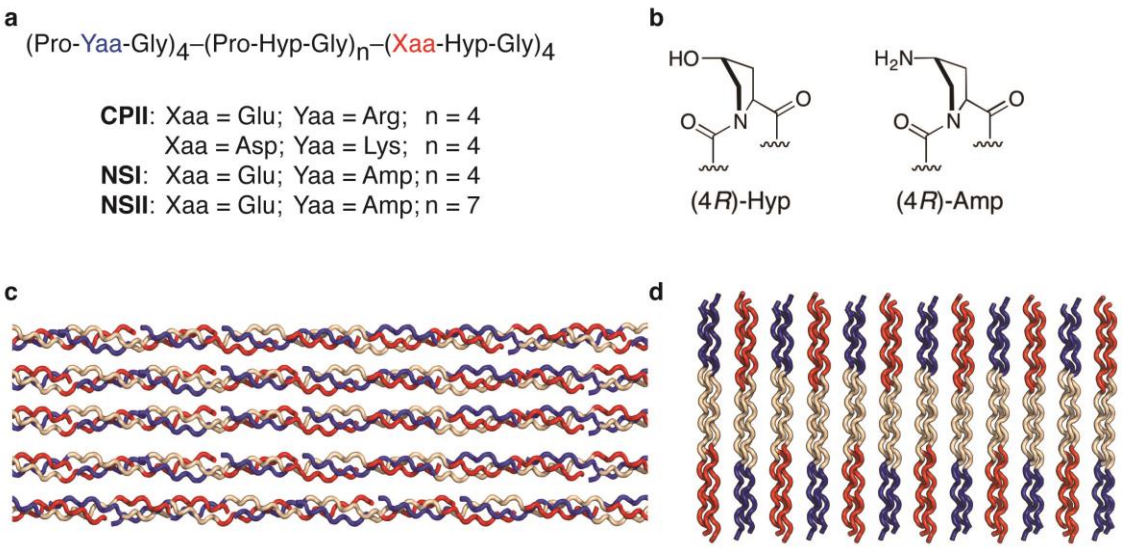

Figure 2.1 (A) Amino acid sequences of peptides (red: negatively charged amino acids or triads; blue: positively charged amino acids or triads). (B) Structures and preferred ring pucker conformers of imino acid derivatives. (C) Proposed staggered orientation of peptides indicating alignment within collagen-mimetic fibrils. (D) Proposed packing of collagen triple helices within two-dimensional layers through electrostatic interactions.

2.3 Results and discussion

2.3.1 Circular dichroism

Circular dichroism (CD) spectropolarimetry of solutions of **NSI** (2 mg/mL) and **NSII** (2.5 mg/mL) in MOPS buffer (20 mM, pH 7.0) displayed a characteristic collagen triple helical conformation, consisting of a positive maximum at 224 nm and a negative minimum at 198 nm (Figure 2.2). The RPN values, i.e., the ratio of intensities of the positive CD signal at 224 nm to the negative CD signal at 198 nm,[43] were 0.10 and 0.11 for the solutions of **NSI** and **NSII**, respectively. An RPN value of ≥ 0.10 is consistent with a stable triple helical structure. Thermal denaturation studies were performed on solutions

of the corresponding peptides, which afforded melting transitions (T_m) of 32 ℃ and 60 ℃ for **NSI** and **NSII**, respectively (Figure 2.3). T_m is estimated from the minimum in the first derivative curve. The presence of three additional triads of (Pro-Hyp-Gly) in the central block of **NSII** increased the thermal stability of the triple helical conformation vis-à-vis that of **NSI**. The T_m values observed for solutions of **NSI** and **NSII** were significantly below the values expected for collagen-mimetic peptides containing an identical number of canonical (Pro-Hyp-Gly) triads. These data suggest that the aminoproline and glutamic acid residues within the **NSI** and **NSII** peptides thermodynamically destabilize the triple helical conformation. In a previous study, Ganesh, et al,[33,34] have demonstrated that Amp could be substituted in place of hydroxyproline (Hyp) in a collagen peptide consisting of six triad repeats (Pro-Amp-Gly). The corresponding peptide adopted a triple helical structure that was stable at both acidic and basic pH to a greater degree than a peptide of identical length based on the canonical triad repeat sequence (Pro-Hyp-Gly). However, these comparisons were drawn from CD spectropolarimetry of the corresponding peptides that was performed in the presence of 100 mM NaCl, which effectively screened the charge repulsion between Amp residues.

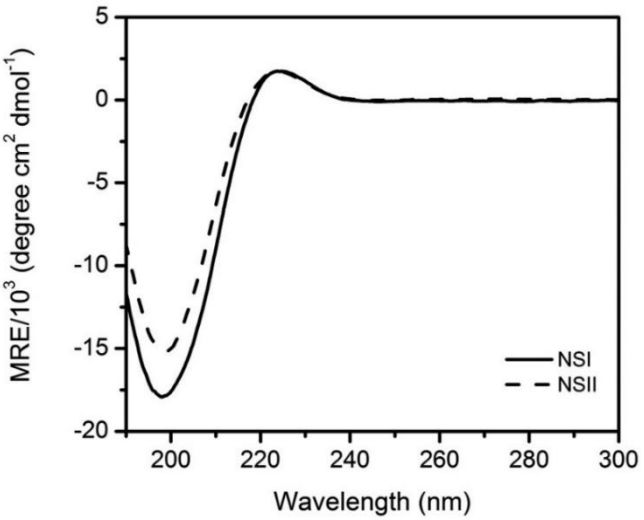

Figure 2.2 CD spectra of aqueous solutions of peptide **NSI** and **NSII**.

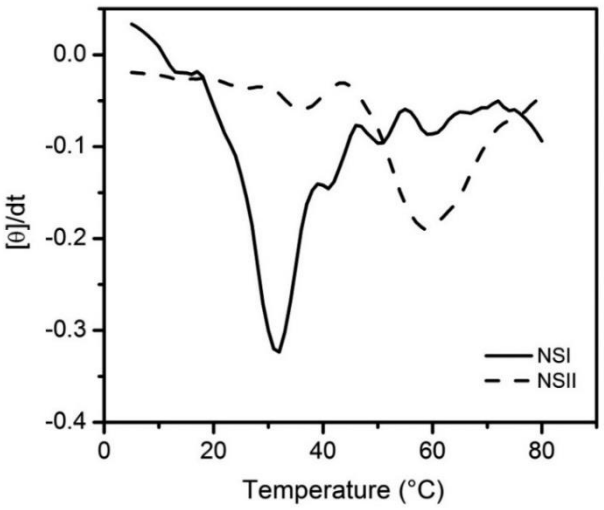

Figure 2.3 First derivative of the CD melting curve derived from monitoring the maximal signal as a function of temperature for aqueous solutions of **NSI** and **NSII**.

2.3.2 Flow linear dichroism

Flow linear dichroism[44,45] spectra were acquired under shear alignment for solutions of **NSI** as a function of incubation time to interrogate for the formation of assemblies (Figure 2.5). The sign and magnitude of the absorbance in flow linear dichroism can be correlated with the direction of polarization of the amide bond chromophores, which can be related to the orientation of self-assembled species in the flow field. Net orientation occurs for anisotropic self-assembled structures that persist under Couette flow. Solutions of freshly dissolved **NSI** (0.5 mg/mL in 20 mM MOPS buffer, pH 7.0) under a Couette flow of 2000 r.p.m displayed a weak positive absorbance at a position coincident with that expected for collagen fibrils.[46] However, incubation of the **NSI** solutions (0.5 mg/mL in 20 mM MOPS buffer, pH 7.0) for a period of weeks at 4 ℃ resulted in a significant change in the flow LD spectrum. The amide bond absorbance displayed a polarization that was opposite to that of the initially prepared **NSI** specimen as well as that of fibrillar Type I collagen. (0.4 mg/mL in 100 mM sodium phosphate buffer, pH 7.4) (Figure 2.4) The intensity of the signal for the mature **NSI** assemblies also increased significantly in comparison to the initial sample, approaching that of the fibrillar collagen preparation. The flow LD data support the formation of extended assemblies of **NSI**, in which the collagen triple helices are oriented in the flow field such that the long axis of the triple helix is perpendicular to the direction of flow. This arrangement would be consistent with assemblies consisting of layers of perpendicularly oriented collagen triple helices (Figure 2.1D). Surprisingly, a corresponding flow LD signal was not observed for assemblies derived from the more thermodynamically stable **NSII**. Subsequent studies indicated that the **NSII** assemblies were less robust toward shear alignment, which resulted in dis-

assembly of the supramolecular structures under Couette flow (vide infra). The flow LD data suggested that solutions of **NSI**, and, by association, **NSII**, could self-assemble into supramolecular structures in solution.

Figure 2.4 Negative stain TEM images of fibrils from type I collagen protein of rat tail.

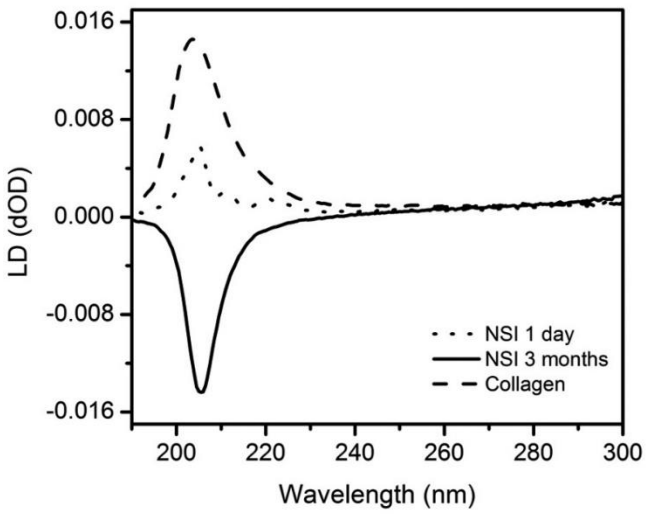

Figure 2.5 Flow LD spectra of nascent and assembled solutions of **NSI**. Flow LD spectrum of fibrillar type I collagen from rat-tail was employed under identical conditions as a standard of comparison.

2.3.3 Transmission Electron Microscopy

The formation of the assemblies was confirmed through correlative analysis with transmission electron microscopy (TEM). The self-assembly of **NSI** and **NSII** peptides in solution was monitored over time. The rate of formation of the assemblies was observed to depend on the concentration and molar mass of the peptide and ranged from weeks to hours. Dilute solutions of **NSI** (2 mg/mL in 20 mM MOPS, pH 7.0) assembled over a period of weeks, while more concentrated solutions (4 mg/mL) formed assemblies over a period of days. In contrast, solutions of **NSII** (2.5 mg/mL in 20 mM MOPS, pH 7.0) assembled over a period of hours. Analytical HPLC of **NSI** (2 mg/mL) and **NSII** (2.5 mg/mL) solutions in MOPS buffer indicated that approximately 46 % and 30 % of the respective peptides remained in solution after centrifugation (Figures 2.6 and 2.7). Therefore, in either case, the majority of the peptide was observed to sediment as self-assembled species.

TEM analysis of **NSI** and **NSII** assemblies was consistent with the presence of two-dimensional nano-scale sheets as the only observable self-assembled structures (Figure 2.8 and 2.9). Most commonly, the sheets occurred as fully formed tetragonal assemblies with cleanly defined edges in both lateral dimensions. On occasion, sheets were observed in stages of incomplete growth, in which well-defined terraces could be detected (Figure 2.10). Typically, the nanosheets displayed a wide dispersion in lateral dimensions; the polymorphism may be attributable to slow nucleation kinetics for sheet formation. This

effect was more pronounced for sheets derived from **NSI** in comparison to **NSII**. In the former case, polymorphism could be detected not only in the plane of the sheet, but also in the direction normal to the plane. In the TEM images of **NSI** sheets, this dispersion in height was manifested in terms of differences in the electron contrast among the assemblies (Figure 2.8). An equimolar mixture of the two peptides, **NSI** and **NSII**, did not appear to form mixed species, but rather a mixed population of nanosheets that were characteristic of the individual peptides (Figure 2.11).

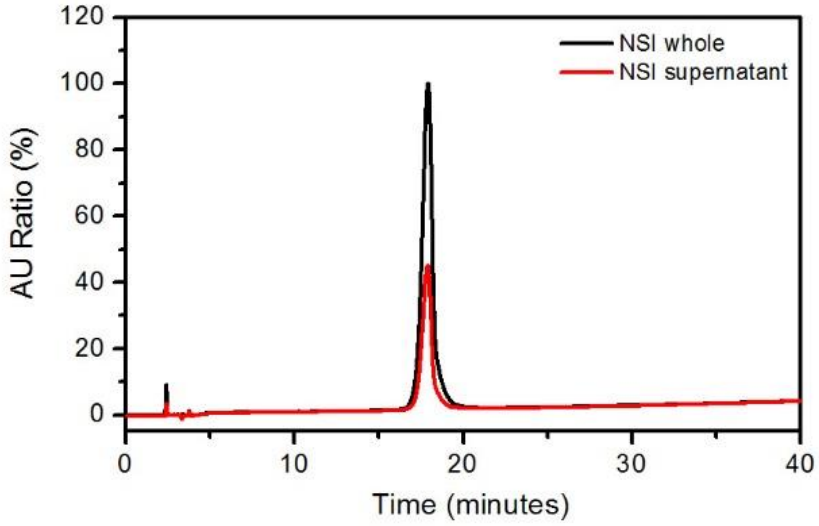

Figure 2.6 Analytical HPLC analysis of **NSI** in aqueous solutions for quantitation of the relative content of free peptide before (whole) and after (supernatant) centrifugation to sediment the nanosheets.

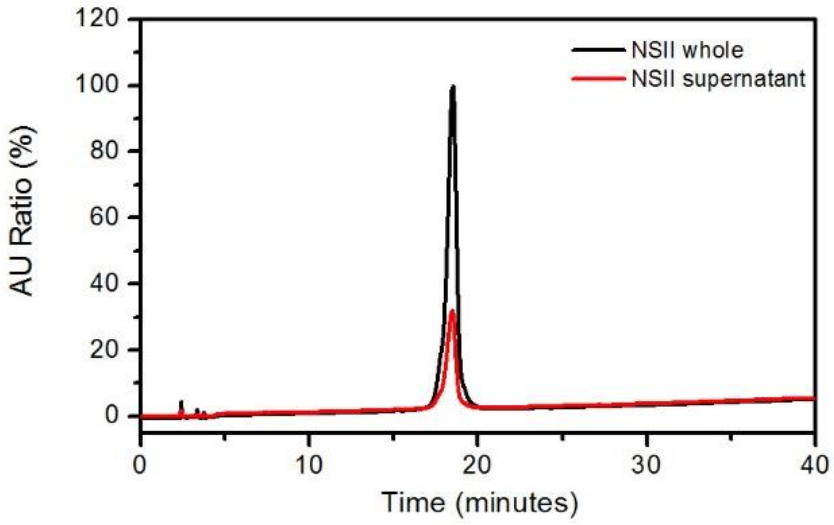

Figure 2.7 Analytical HPLC analysis of **NSII** in aqueous solutions for quantitation of the relative content of free peptide before (whole) and after (supernatant) centrifugation to sediment the nanosheets.

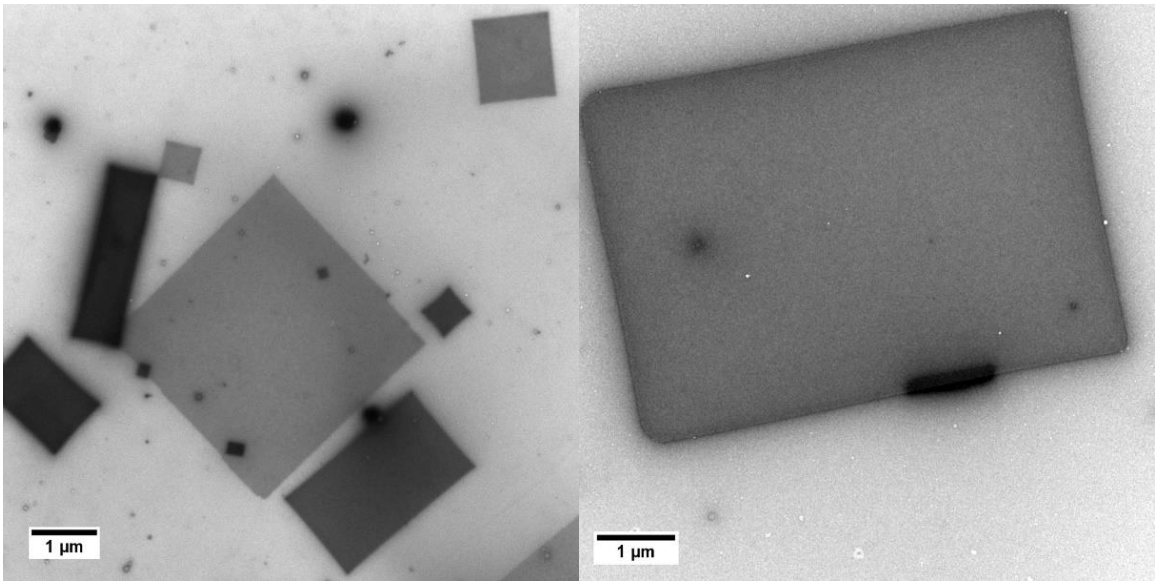

Figure 2.8 Negative stain TEM images of **NSI** nanosheets.

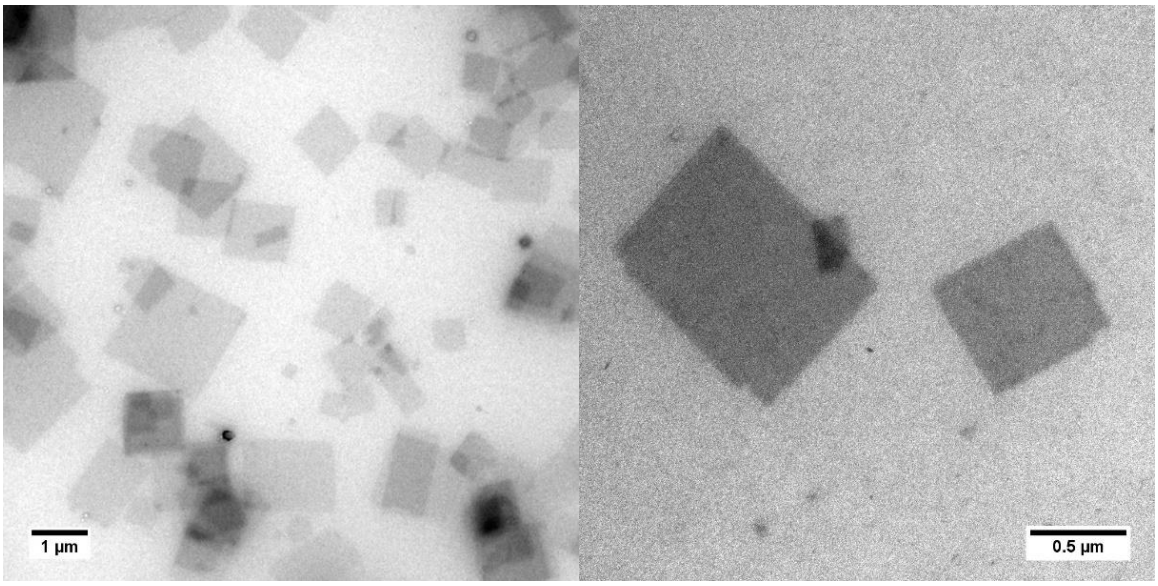

Figure 2.9 Negative stain TEM images of **NSII** nanosheets.

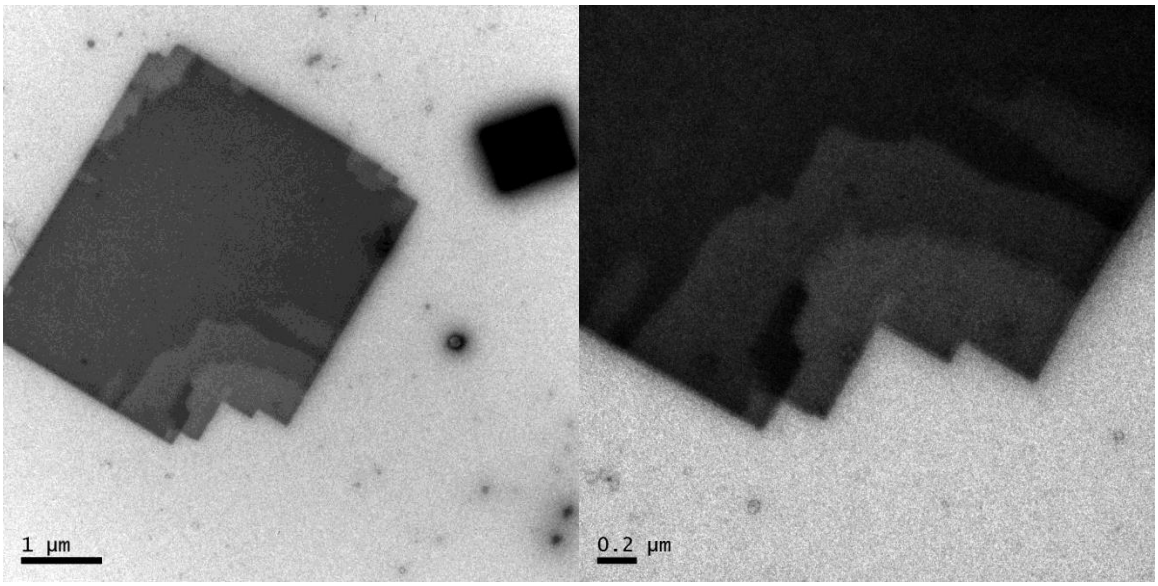

Figure 2.10 Negative stain TEM images of **NSI** nanosheets showing incomplete growth.

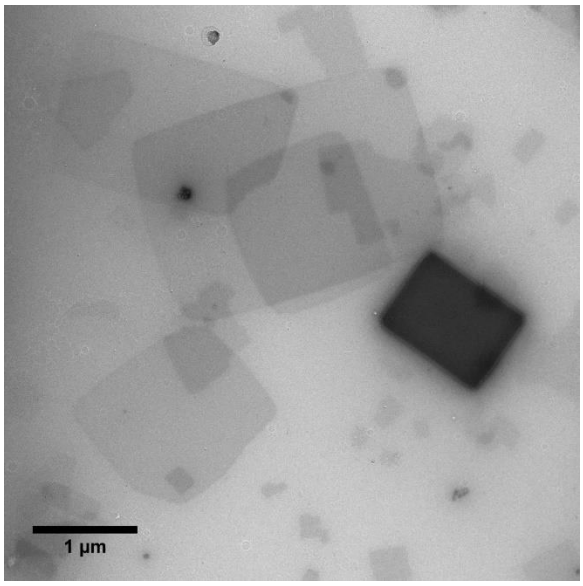

Figure 2.11 Negative stain TEM image of the nanosheets from an equimolar mixture of peptide **NSI** and **NSII**.

2.3.4 Atomic force microscopy

Atomic force microscopy (AFM) analysis was employed to interrogate the height of the assemblies, which was observed to depend on the concentration and molar mass of the peptides. Solutions of **NSI** incubated for long periods under dilute conditions (2 mg/mL) afforded much thicker nanosheets, with heights up to circa 250 nm. More concentrated solutions of **NSI** (4 mg/mL) and solutions of **NSII** (2.5 mg/mL) afforded thinner sheets. Nanosheets of **NSII** were typically only one or two layers in thickness (Figure 2.13). This observation may explain the absence of a flow LD signal for **NSII**, as the thinner sheets were not significantly robust to withstand the shear forces necessary for alignment. TEM analysis of shear aligned samples of **NSII** nanosheets indicated significant fragmentation subsequent to attempted alignment within a Couette cell. For the thicker sheets of **NSI**, AFM provided evidence for multiple stacked layers of collagen peptides, as

terraces could be observed on the surface of the sheets that corresponded to growth of new layers (Figure 2.12). AFM measurements provided values of 8.8 ± 0.8 nm and 12.3 ± 0.7 nm for the heights of single-layer sheets of **NSI** and **NSII**, respectively (Figure 2.14). The calculated thickness for a layer comprising vertically oriented triple helices of **NSI** and **NSII** should be 10.3 nm and 12.9 nm, respectively (# residues x 0.286 nm rise/residue).[47,48] These data suggest that the nanosheets are composed of stacked layers of collagen triple helices. The difference in layer height between nanosheets derived from **NSI** and **NSII** could be attributed to the respective differences in peptide length projected onto a collagen triple helix.

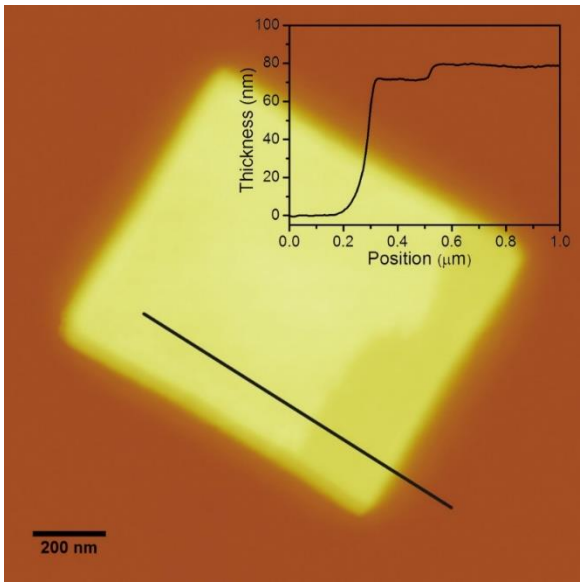

Figure 2.12 AFM image and height profile (inset) of a multilayer nanosheet from **NSI**.

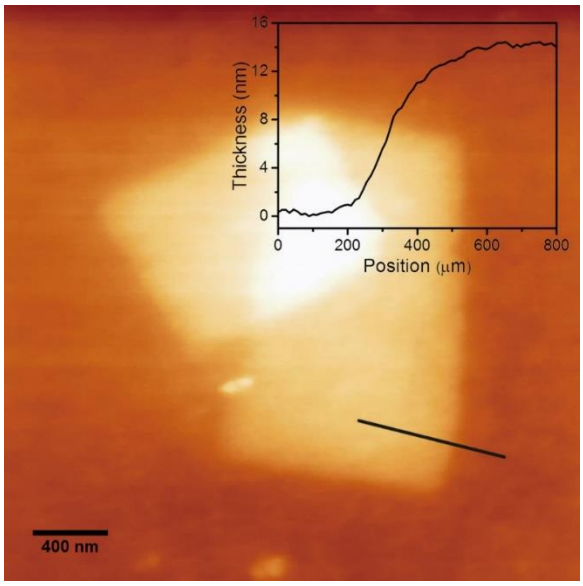

Figure 2.13 AFM image and height profile (inset) of the nanosheets from **NSII**.

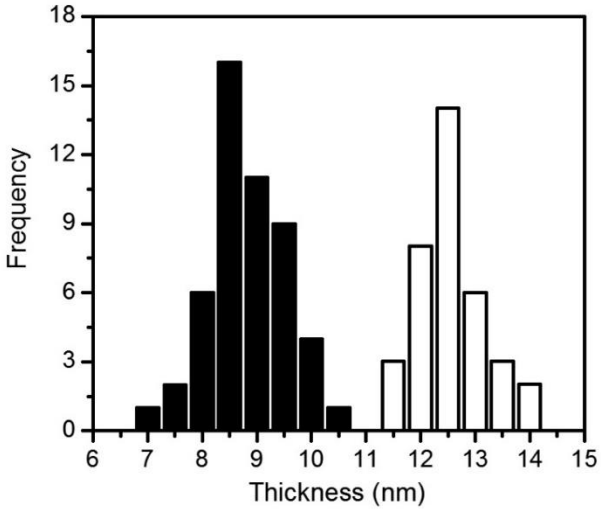

Figure 2.14 AFM height histogram for single-layer sheets from **NSI** (black) and **NSII** (white).

2.3.5 Solution X-ray scattering measurements

The well-defined morphology of the **NSI** and **NSII** nanosheets suggested an ordered internal structure. The thicker assemblies derived from peptide **NSI** proved more physically robust to structural analysis and were studied in further detail. Synchrotron SAXS/WAXS data were collected on aqueous solutions of **NSI** in MOPS buffer. The resultant plot of intensity versus momentum transfer (q) displayed a complex dependence in which form factor scattering was convoluted with sharp Bragg reflections (Figure 2.15). The scattering intensity in the Porod region followed a power law dependence of the momentum transfer (q^{-2}).[49] The mass fractal dimension confirmed the sheet-like structure in solution (Figure 2.16). However, the dispersion in sheet thickness prevented extraction of the single-layer sheet height using Guinier analysis. In the higher q region, four diffractions signals were observed; two peaks of relatively weak intensity at q values of 0.0600 $Å^{-1}$ and 0.120 $Å^{-1}$, and two strong, sharp peaks at q values of 0.405 $Å^{-1}$ and 0.573 $Å^{-1}$. The former signals correspond to d-spacings of 105 Å and 52.4 Å. The larger distance of 10.5 nm was consistent with the height of a single layer of laterally aligned collagen triple helices derived from **NSI** (vide supra). The smaller spacing of 52.4 Å was approximately half that of the 105 Å spacing, which suggested that the larger distance corresponds to that of a (001) lattice plane while the smaller one is consistent with the (002) plane. The observation of a diffraction peak associated with the (002) plane suggests that the triple helices within a layer may be packed with an anti-parallel orientation between nearest neighbors (vide infra). The weak intensity of these two reflections is indicative of the limited layer stacking in the z direction, i.e., perpendicular to the surface of the two-dimensional sheet.

The more intense signals at larger q values correspond to d-spacings of 15.5 Å, and 11.0 Å, which fall into the regime of reported inter-triple helical distances from crystal structures of collagen-mimetic model peptides.[40-42,50-56] Interestingly, these two d-spacings are related in that the 15.5 Å distance is equal to √2 times the 11.0 Å distance, which suggests that a two-dimensional tetragonal lattice may underlie the layered packing of collagen triple helices in nanosheets of **NSI**. The crystal structures of collagen-mimetic peptide sequences can be sorted into two symmetry classes based on pseudo-hexagonal and pseudo-tetragonal packing of triple helices, respectively. The packing of the 2D lattice of the **NSI** nanosheets more closely approximates the packing of the latter structures, although the dimensions of the lattice are contracted from the lattice parameters typically observed for pseudo-tetragonal packing within the crystal structures of collagen-mimetic peptides (e.g., PDB IDs: 1 ITT, 1X1K, 2 CUO, 2D3F, 2D3H, 3ADM, 3AH9, 3A1H, and 3AI6).[40-42,54,56]

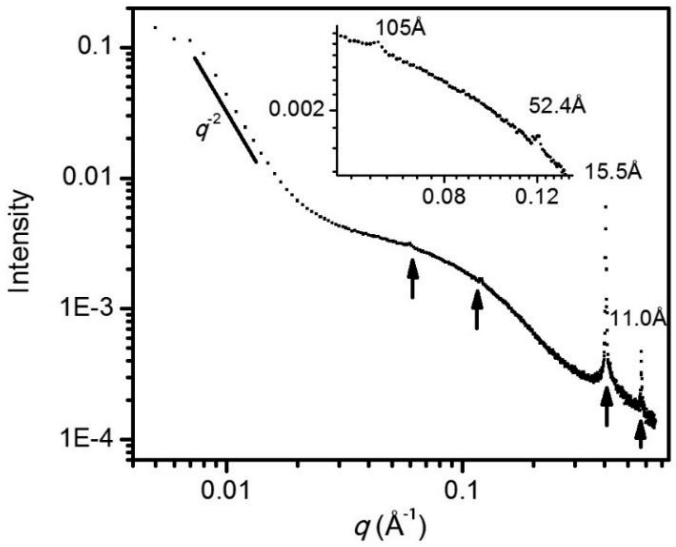

Figure 2.15 Synchrotron SAXS scattering profile for **NSI** sheets showing q^{-2} dependence in the Porod region and diffraction peaks.

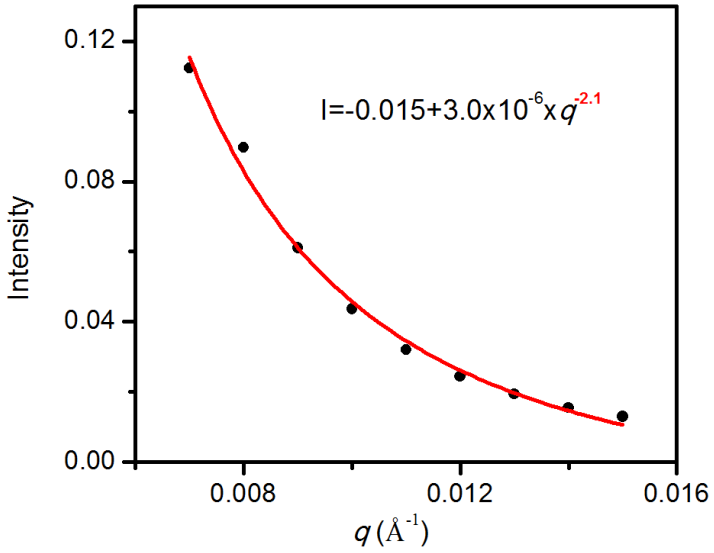

Figure 2.16 Fitting of the SAXS scattering data of **NSI** nanosheets within Porod region.

2.3.6 Electron diffraction measurements

Electron diffraction (ED) data (Figure 2.17) from nanosheets of **NSI** provide additional support for a 2D lattice of perpendicularly oriented collagen triple helices. Sharp diffraction spots are observed at d-spacings of 15.2 Å (lattice indicated by (1)) and 10.8 Å (lattice indicated by (2)), which are nearly identical to those observed in the solution SAXS measurements. Fourfold rotational symmetry was observed for the major and minor diffraction lattices, with a 45 ° angular offset between the two lattices. Lattice orientations for the larger d-spacing coincided with the directions of the sheet edges in the corresponding TEM image (Figure 2.18). The symmetry and lattice spacings of the **NSI** nanosheets were compared to the pseudo-tetragonal packing of triple helices in the ab-plane from the crystal structure of a representative collagen-mimetic model peptide (PDB

ID: 3AI6).(Figure 2.19) The comparative data suggest that the 2D lattice of the **NSI** nanosheets comprises a unit cell of 22 Å x 22 Å containing four triple helices. The 15.5 Å and 11.0 Å d-spacings correspond to reflections from the (110) and (200)/(020) lattice planes, respectively. Diffraction peaks of similar intensity can be calculated for the corresponding lattice planes in the crystal structure of the collagen-mimetic model peptide (Figure 2.19 and Table 2.1).

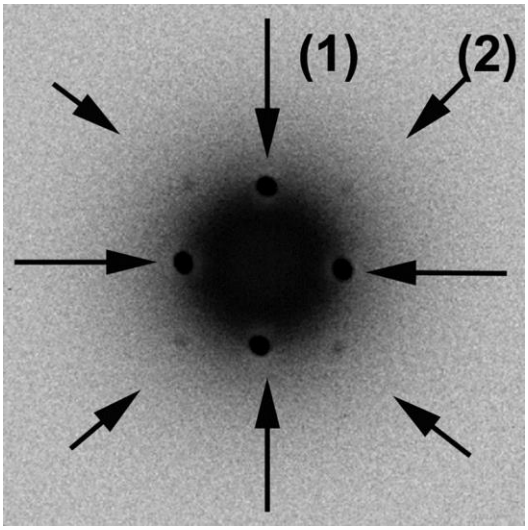

Figure 2.17 Electron diffraction pattern from an isolated **NSI** nanosheet.

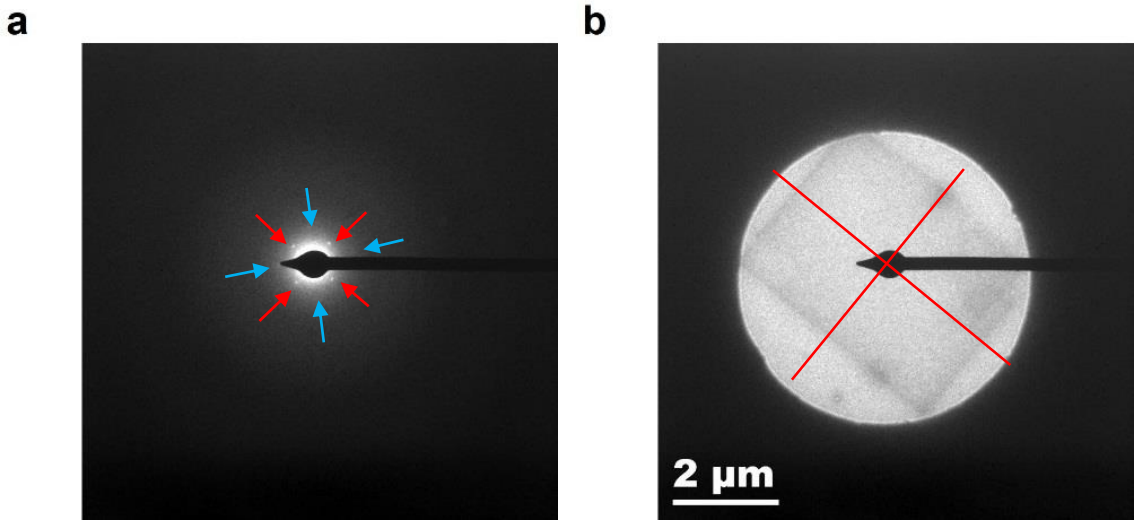

Figure 2.18 (A) Electron diffraction pattern from an isolated **NSI** nanosheet, comprising major diffraction lattice (red arrows) and weak lattice (blue arrows). (B) Corresponding negative stain TEM image of **NSI** nanosheet under investigation,

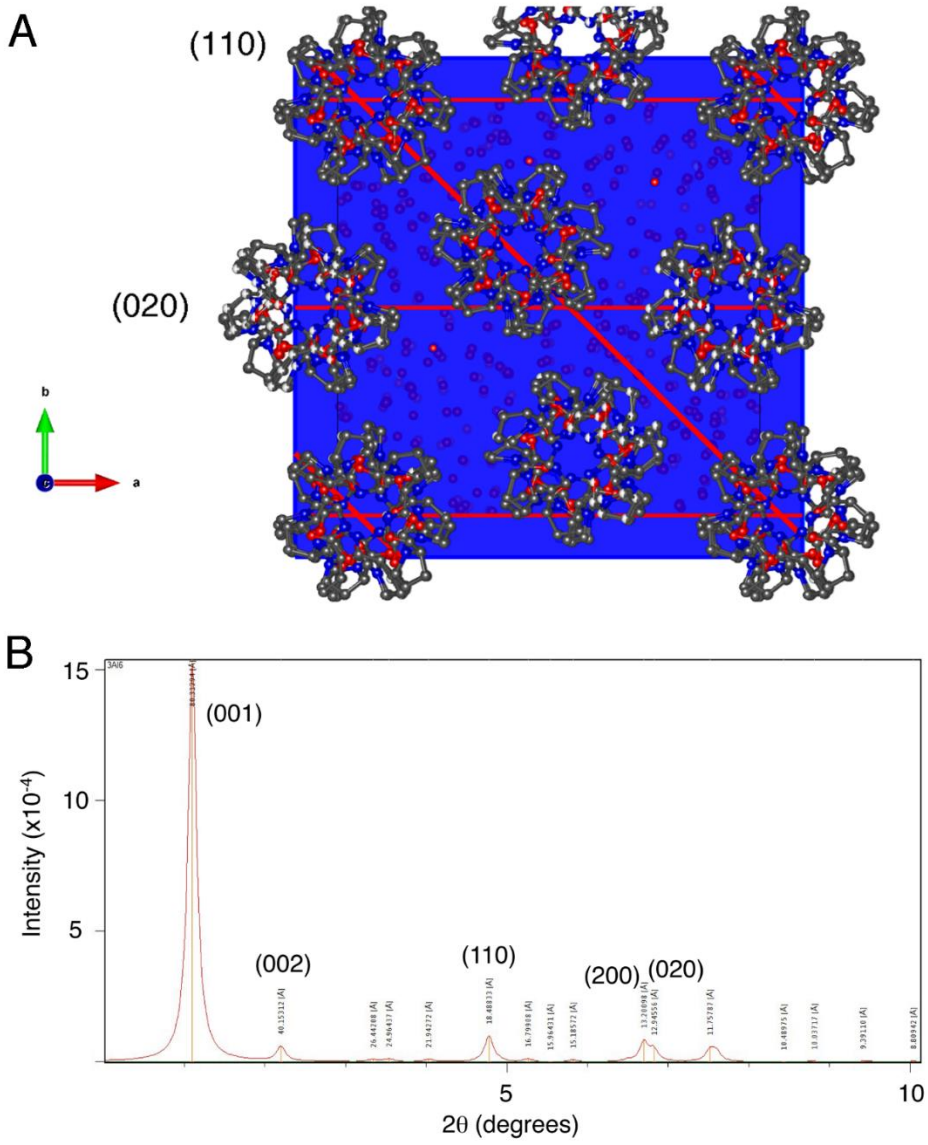

Figure 2.19 (A) The crystal structure of the (Pro-Pro-Gly)$_9$ triple helix (Protein data bank entry 3AI6). View along the c axis of the pseudo-tetragonal packing of triple helices in ab plane (B) Calculated powder pattern from the structure.

H	K	L	2θ	Intensity	d (Å)
0	0	1	1.10	10000000	80.162
0	0	2	2.20	364330	40.083
0	0	3	3.31	25590	26.724
1	0	0	3.35	37959	26.357
0	1	0	3.41	0	25.924
1	0	1	3.53	30785	25.043
-1	0	1	3.53	16289	25.043
0	1	1	3.58	15100	24.666
0	-1	1	3.58	15100	24.666
-1	0	2	4.01	3	22.034
1	0	2	4.01	45988	22.023
0	-1	2	4.06	10714	21.763
0	1	2	4.06	10709	21.763
-1	0	3	4.71	1626	18.769
1	0	3	4.71	14605	18.761
0	-1	3	4.75	2361	18.603
0	1	3	4.75	2362	18.603
1	1	0	4.78	319787	18.486
-1	1	0	4.78	319787	18.486
2	0	0	6.71	485232	13.180
0	2	0	6.82	290543	12.960

Table 2.1 Calculated intensities and d-spacings for selected lattice planes derived from the crystal structure of the $(Pro\text{-}Pro\text{-}Gly)_9$ triple helix (Protein data bank entry 3AI6).

2.3.7 Scanning transmission electron microscopy

Scanning transmission electron microscopy (STEM)[57-61] was employed to measure the mass-per-area (M/A)[3,62] of freeze-dried specimens of **NSI** nanosheets. Single-layer sheets of **NSI** were observed to have an average mass per area value of 75

Da/Å^2 (Figures 2.20). A theoretical mass-per-area of 83 Da/Å^2 was calculated for a 22 Å x 22 Å tetragonal unit cell containing four triples helices with individual masses of 10,044 Da derived from trimers of the **NSI** peptide (Figure 2.22). The calculated and experimentally determined M/A values compare well within the error limits of the STEM analysis. Moreover, multilayer sheets of **NSI** displayed a progression of M/A values between layers that differed by increments of approximately 80 Da/Å^2 (Figure 2.21, inset). This observation further substantiated a packing arrangement in which collagen layers were successively laminated to form the thick nanosheets derived from self-assembly of **NSI**.

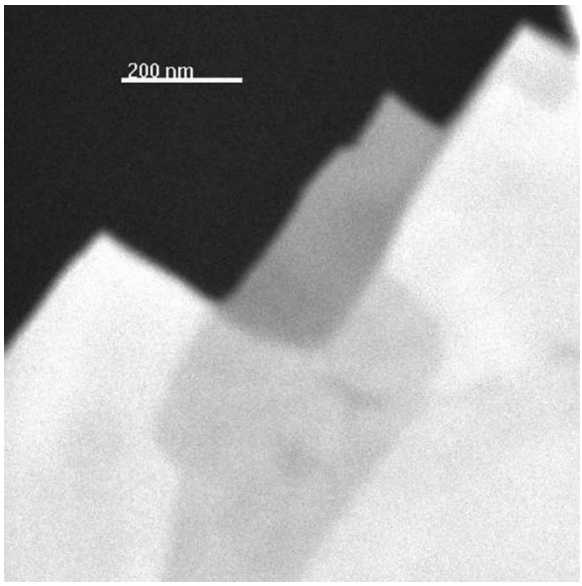

Figure 2.20 Dark field STEM of freeze dried, unstained specimens of a multilayer nanosheet of **NSI** in MOPS buffer.

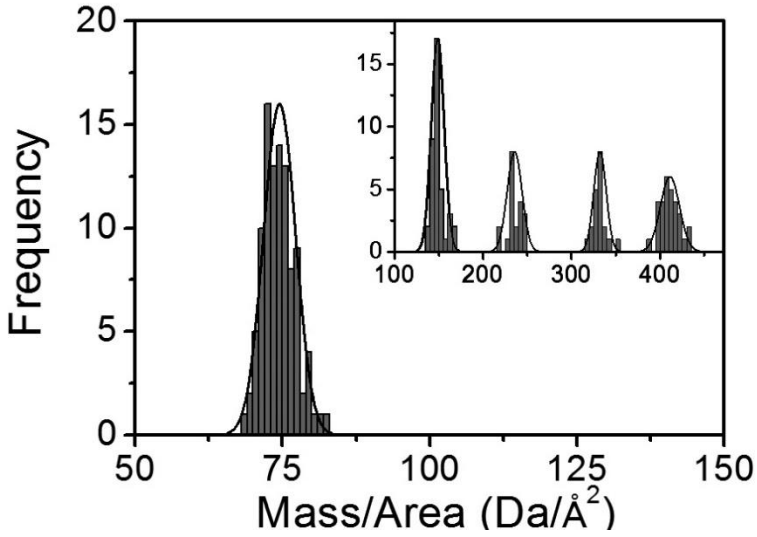

Figure 2.21 Mass-per-area measurements for **NSI** nanosheets in the single-layer and multilayer (inset) regions.

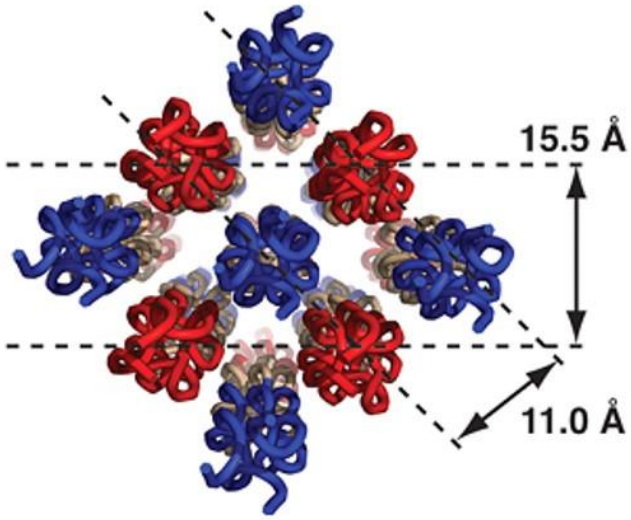

Figure 2.22 Proposed structural model of the 2D lattice in **NSI** sheets in a face centered tetragonal arrangement of anti-parallel triple helices.

2.3.8 Gold nanoparticle binding assay

The well-ordered peptide packing within the nanosheets suggests that the surfaces of the assemblies should be decorated with functional groups derived from the termini of the peptide (Figure 2.22). The functional groups at the sheet surface should be accessible for interaction with exogenous substrates. As a test of this hypothesis, nanosheets derived from **NSII** were probed with cationic gold nanoparticles (10 nm core diameter functionalized with (11-mercaptoundecyl)-N,N,N-trimethylammonium bromide). The positively charged ammonium ions immobilized on the gold nanopartilces should interact selectively with the negatively charged C terminal carboxylate groups of the peptides. TEM and AFM analysis provide evidence for relatively dense packing of the nanoparticles at the surface of **NSII** nanosheets (Figure 2.23 and 2.24). The diameter of the nanoparticles is much larger than the distance between adjacent triple helices in the structure (circa 11-15 Å). The nanoparticles tend to spread out evenly on the surface at lateral spacings that are larger than the nanoparticle diameter. Fourier transforms of the TEM images do not provide evidence for an ordered arrangement of nanoparticles on the surface, which may indicate either that the system has not achieved equilibrium under the experimental conditions or that the surface functional groups may adopt a more disordered arrangement than the internal structure of the assembly.

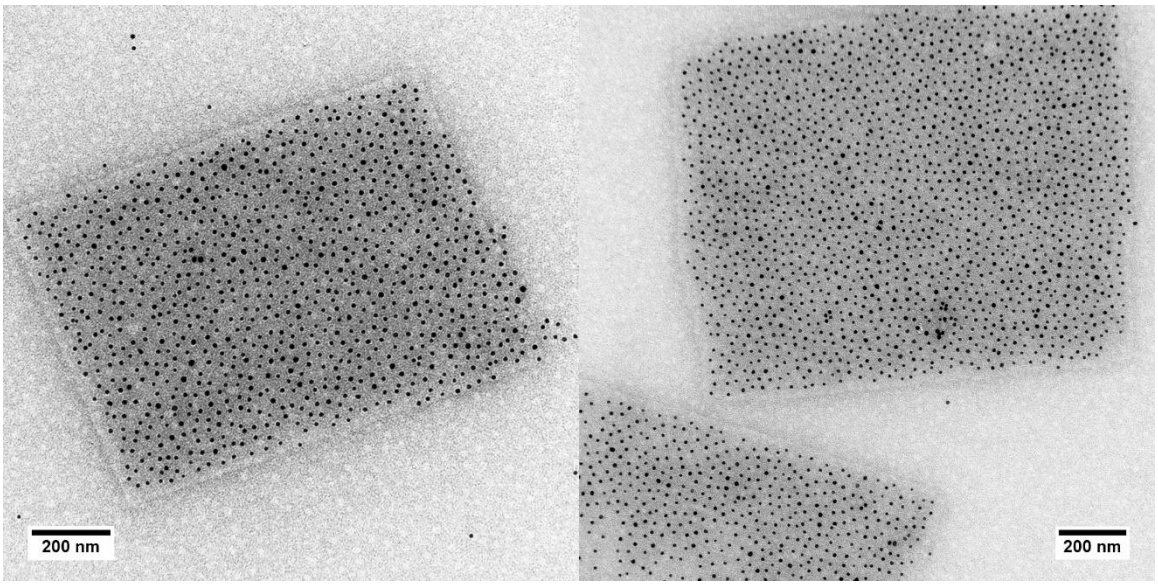

Figure 2.23 Negative stain TEM images of **NSII** nanosheet probed with cationic gold nanoparticles.

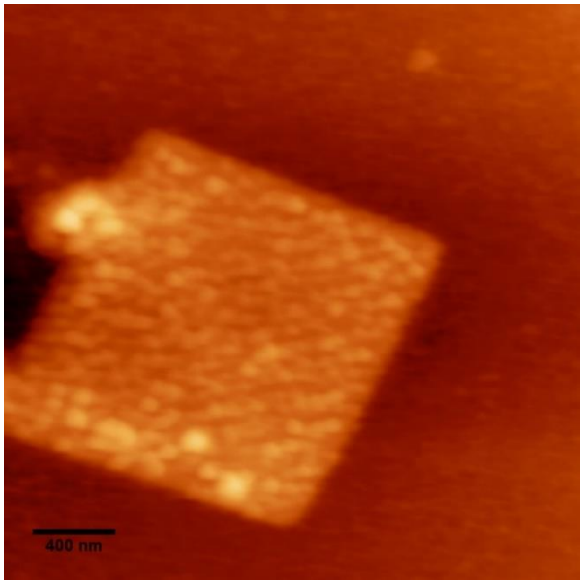

Figure 2.24 AFM image of **NSII** nanosheet probed with cationic gold nanoparticles.

2.3.9 Chemical modification of sheet surface

In order to promote a more specific interaction between the gold nanoparticles and nanosheets, a variant of peptide **NSII**, **NSII***, was synthesized in which the N-terminus was capped with the D-biotin-15-amido-4,7,10,13-tetraoxapentadecyl group (biotin-dPEG$_4$). CD spectropolarimetry of peptide **NSII*** (2.8 mg/mL) in MOPS buffer (20 mM, pH 7.0) indicates the presence of the triple helical conformation of collagen, although the RPN value of 0.083 and T_m value of 54 ℃ suggest that the structure is less stable than that of **NSII** (Figures 2.25 and 2.26). **NSII*** (10 mg/mL in 20 mM MOPS buffer, pH 7.0 3 weeks) self-assembles into nanosheets of similar morphology to **NSII** assemblies under identical conditions (Figure 2.27). Nanosheets derived from **NSII*** bind selectively to streptavidin-tagged gold nanoparticles (10 nm core diameter) with high affinity (Figure 2.28A). In contrast, nanosheets of **NSII** show no tendency to bind streptavidin-tagged gold nanoparticles (Figure 2.28B). The nanoparticle binding appears denser and less uniform than the corresponding interaction of the **NSII** nanosheets with cationic gold nanoparticles (Figure 2.23 and 2.24). The strength of the biotin-streptavidin interaction dictates that the binding of the nanoparticles is kinetically irreversible in the former case, which explains the differences in particle distribution at the sheet surface.

The biotin-streptavidin interaction could also be employed to selectively immobilize nanosheets of **NSII*** on functionalized surfaces (Figures 2.29). Biotin-derivatized glass surfaces were treated with excess streptavidin, followed by incubation with pre-assembled nanosheets of **NSII***. The immobilized nanosheets were visualized using fluorescence microscopy after treatment with a solution of streptavidin-tagged Alexa488 dye. Reflection interference contrast microscopic (RICM) indicated that the

fluorescent signal co-localized with the nanosheet (Figure 2.29). In general, the biotin-capped nanosheets of **NSII*** could be immobilized on the surface with retention of the 2D shape. However, structural remodeling was also noted for some nanosheets upon immobilization, perhaps due to the strength of the biotin-streptavidin interaction. Although the **NSII*** nanosheets attached with random orientations to the functionalized surface, these data demonstrate the potential for construction of hybrid nanostructures through programmable noncovalent interactions, which is an essential condition for articulation of the nanosheets into functionally complex 2D nanoarchitectonic platforms.

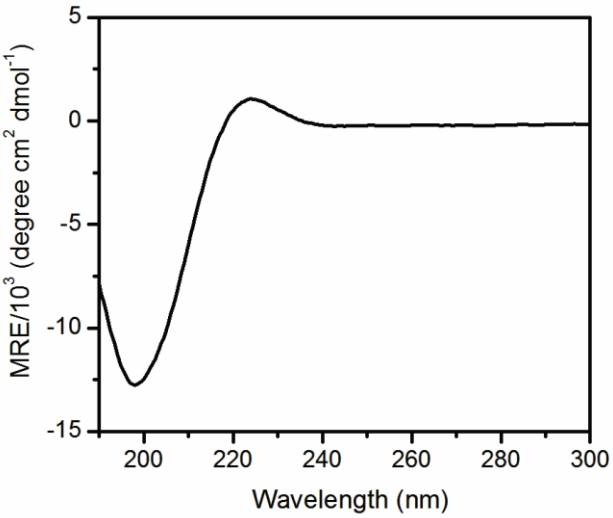

Figure 2.25 CD spectrum of an aqueous solution of peptide **NSII***.

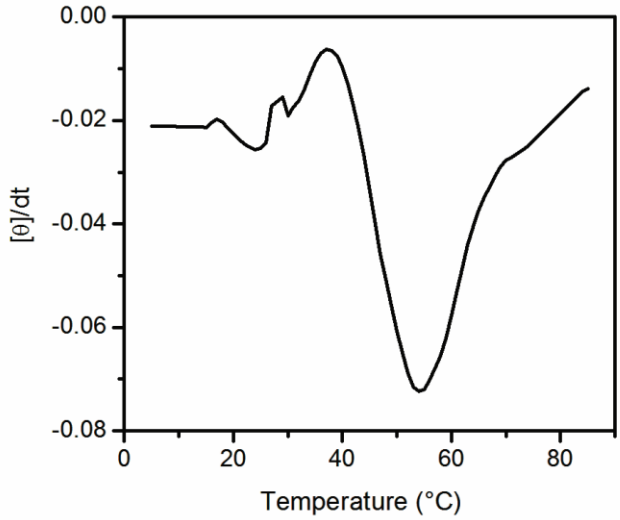

Figure 2.26 First derivative of the CD melting curve derived from monitoring the maximal signal as a function of temperature for an aqueous solution of **NSII***.

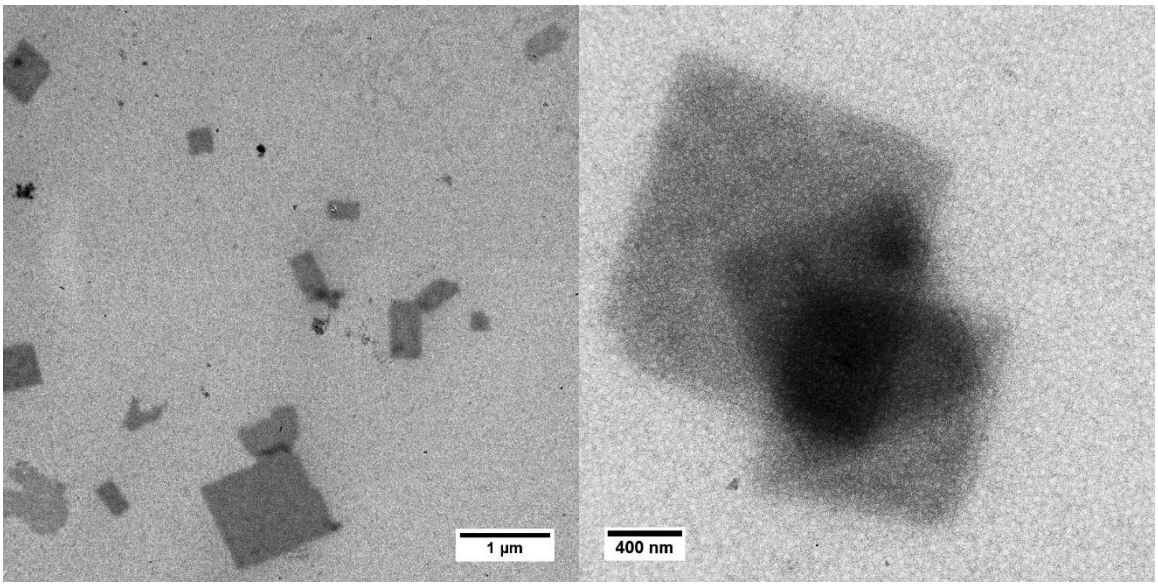

Figure 2.27 Representative TEM images of **NSII*** nanosheets.

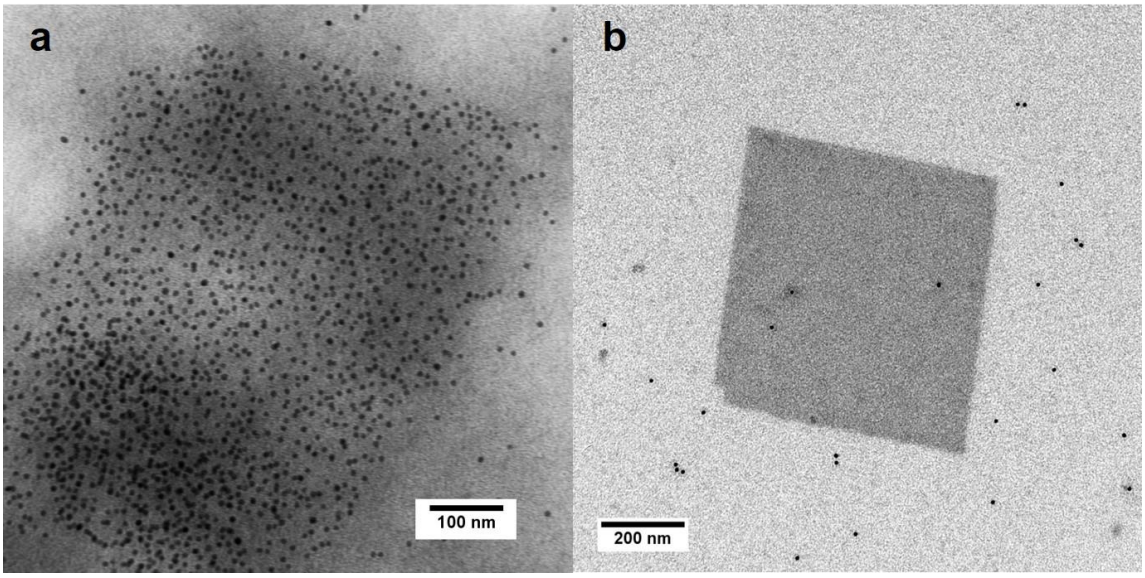

Figure 2.28 TEM images of (A) **NSII*** and (B) **NSII** nanosheets probed with streptavidin-tagged gold nanoparticles

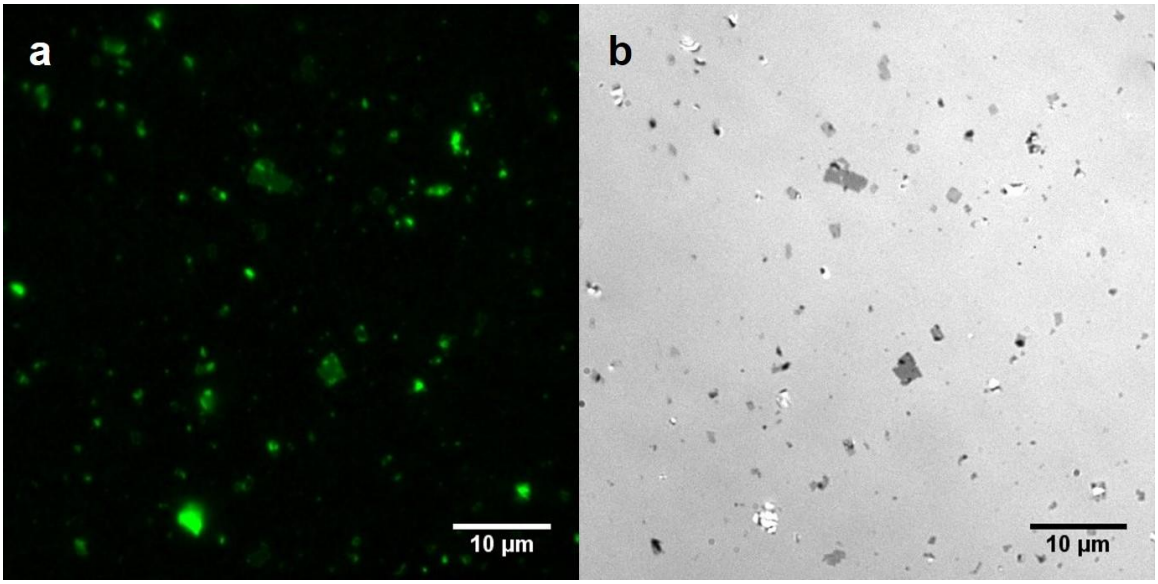

Figure 2.29 (A) Fluorescence microscopic and (B) Reflection interference contrast microscopic (RICM) images of **NSII*** sheets immobilized on a biotinylated glass surface and stained with streptavidin-Alexa488.

2.4 Summary

Significant research effort over the past two decades has been directed toward creation of structurally complex materials through solution-based self-assembly. However, most studies have focused on the design and fabrication of one-dimensional assemblies, e.g., nanofibrils, nanoribbons, and nanotubes, while far fewer examples of structurally defined two-dimensional assemblies have been reported. Sequence specific macromolecules, i.e., peptides and nucleic acids, represent attractive scaffolds for the creation of these assemblies, in that supramolecular structure can be encoded at the molecular level through the progression of structural hierarchy. DNA nanotechnology has enabled the creation of a diverse range of structurally defined 1D-, 2D-, and 3D-assemblies from simplified molecular building blocks.[63-67] DNA has an advantage in that the Watson-Crick base pairing rules provide a simple scoring function that can be employed to distinguish among alternative structural alignments between protomers in multiple dimensions. In contrast, the rules that govern protein-protein interactions are more complex and difficult to reliably predict. However, the sequence specificity and chemical diversity of peptide-based materials affords the opportunity to introduce functional complexity across length-scales, if the intermolecular structural interactions between subunits could be predicted and controlled.[68] In addition, peptides have the advantage of greater chemical stability and physical robustness in comparison to nucleic acids, as well as being more amenable to preparative-scale synthesis.

Two-dimensional protein-based assemblies have been observed in native biological systems, most notably, the crystalline S-layers associated with bacterial surfaces.[69] Significant research effort has been directed toward modification of the S-layer systems

for use in non-native applications as stable two-dimensional platforms for nanotechnology.[70] However, rather than reverse engineering native protein-based 2D assemblies, such as S-layers, we have explored an alternative approach in which synthetic peptide sequences were forward engineered to self-assemble into structurally defined two-dimensional assemblies. This approach has scientific precedent in that peptide[3,62] and peptoid[6] oligomers have been synthesized that self-assemble into 2D nanomaterials. The fibrillogenic peptide **CPII** was re-designed to introduce charge complementarity between triple helices in order to promote lateral assembly into layered structures. Biophysical measurements were conducted in solution and the solid-state on assemblies derived from the resultant peptides, **NSI** and **NSII**, over multiple length-scales of structural hierarchy. The accumulated data suggest that the underlying structure of these nanosheets can be understood in terms of the layered packing of collagen triple helices. Moreover, the chemical functionality displayed at the surface of the nanosheet enabled further elaboration of these structures through surface-localized chemical interactions.

Recently, several collagen-mimetic peptides have been reported that self-assemble into supramolecular structures based on 2D lattices.[17,71] The cohesive interactions between protomers were derived from either metal promoted cross-linking or hetero-chiral peptide recognition. However, the **NSI** and **NSII** nanosheets display a very high degree of internal order over large 2D length scales without recourse to introduction of nonnative structural interactions. Moreover, the nanosheet thickness can be controlled through the peptide length and terminal functionality. The presence of functionalized capping groups provides the opportunity to control the surface chemistry to promote specific interaction with exogenous substrates that have been complementarily functionalized. Previous

investigators have demonstrated that charge complementation is a powerful experimental strategy to control supramolecular structure within peptide-based materials,[6,26,32,71-79] especially when applied in the context of a defined backbone conformation. Our experimental results demonstrate that the collagen triple helix represents a flexible experimental platform for creation of extended self-assembled 2D structures through structurally informed encoding of electrostatic interactions.

2.5 Materials and methods

Materials. Chemical reagents were purchased from Sigma-Aldrich Chemical Co. (St. Louis, MO) or Anaspec, Inc. (Fremont, CA), unless otherwise noted. (2S, 4R)-Boc-4-amino-1-Fmoc-pyrrolidine-2-carboxylic acid (Amp) was purchased from RSP Amino Acids LLC (Shirley, MA). Biotin-dPEG4 acid was purchased from Quanta BioDesign, Ltd. (Powell, OH). Fmoc-Gly-PEG-PS resin for solid-phase synthesis was purchased from Applied Biosystems, Inc. (Foster City, CA). Alexa 488 NHS ester was purchased from Life Technologies, Co. (Carlsbad, CA). Streptavidin was purchased from Rockland Immunochemicals, Inc. (Gilbertsville, PA). Cationic gold nanoparticles (10 nm diameter, functionalized with 11-mercaptoundecyl-N,N,N-trimethylammonium bromide were purchased from Cytodiagnostics Inc. (Burlington, ON, Canada). Mica surfaces modified with (3-aminopropyl)-triethoxysilane (APTES) were obtained from Novascan Technologies, Inc. (Ames, IA).

Peptide Synthesis. Peptides **NSI** and **NSII** were prepared as the uncapped derivatives using microwave-assisted synthesis on a CEM Liberty solid-phase peptide synthesis instrument using an Fmoc-Gly-PEG-PS resin. Standard Fmoc protection chemistry was employed with coupling cycles based on HBTU/DIEA-mediated activation protocols and base-induced deprotection (20% piperidine in DMF with 0.1 M HOBt) of the Fmoc group. Peptides were purified via RP-HPLC on a C18 column with a gradient of water-acetonitrile with 0.1% trifluoroacetic acid. The target fractions were collected and lyophilized. The mass and purity were analyzed by matrix assisted laser desorption/ionization (MALDI) mass spectrometry and analytical HPLC (Figure 2.30-2.33). Peptides were dialyzed against deionized water thoroughly to remove residual

trifluoroacetate (MWCO = 2,000 Da). The resulting peptides were re-lyophilized, and stored at -20 ℃ before use. Peptide **NSII*** was synthesized and purified using an identical procedure, with the exception that the N-terminus was capped with biotin-dPEG$_4$, using in situ activation of the corresponding free acid. The presence of biotin-dPEG$_4$ capping group was confirmed using mass spectrometric analysis (Figure 2.34 and 2.35). Peptides were dissolved in MOPS buffer (20 mM, pH 7.0) at the desired concentration. Solution concentrations were determined from the measured mass of the respective peptides. Samples were thermally annealed at 75 ℃ for 45 min, and gradually cooled to ambient temperature. For analysis of the relative concentration of free peptide, samples of assembled and unassembled peptides were centrifuged at 16,000g for 10 min. The supernatant of the solutions was analyzed using reverse phase analytical HPLC after addition of trifluoroacetic acid to 0.1%.

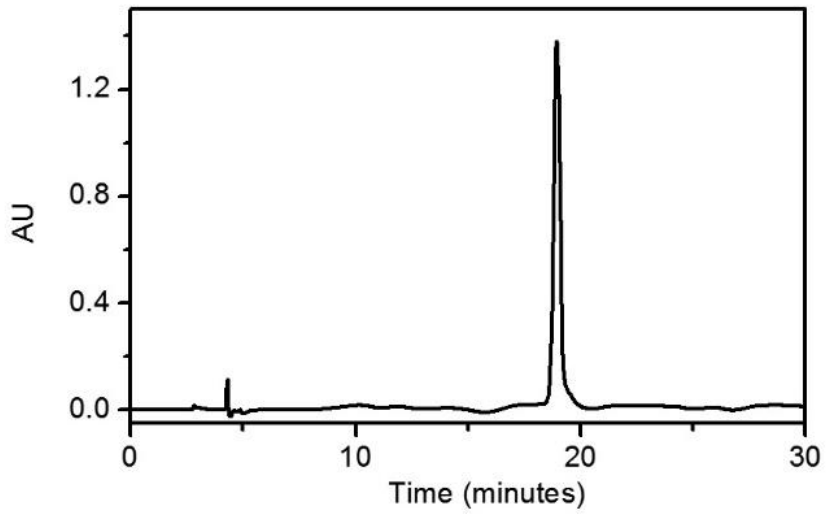

Figure 2.30 Analytical HPLC trace of a purified peptide **NSI**.

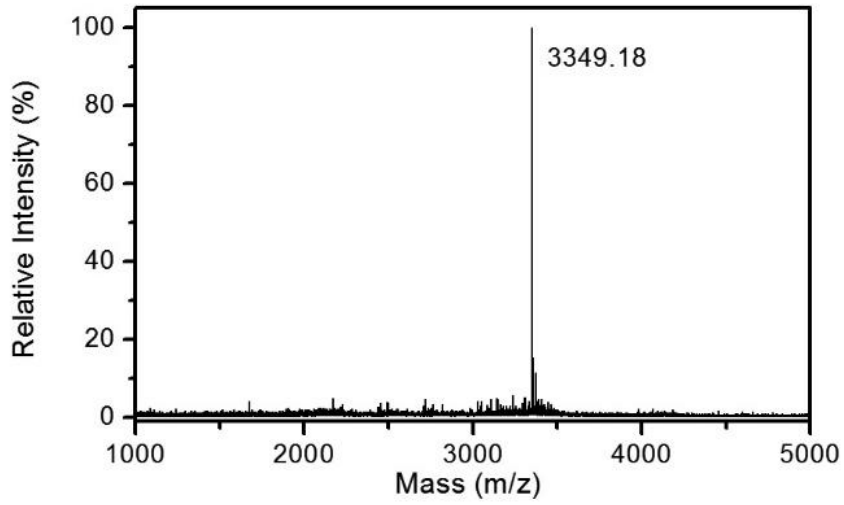

Figure 2.31 MALDI-TOF mass spectrum of a purified peptide **NSI**.

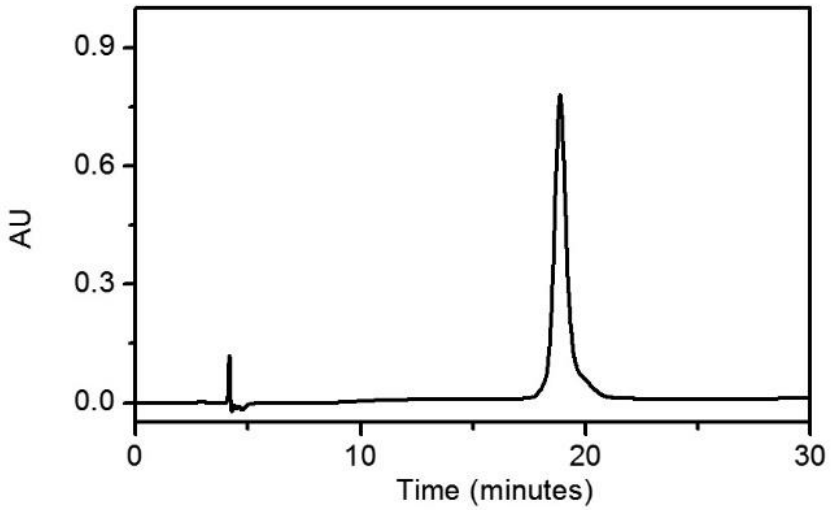

Figure 2.32 Analytical HPLC trace of a purified peptide **NSII**.

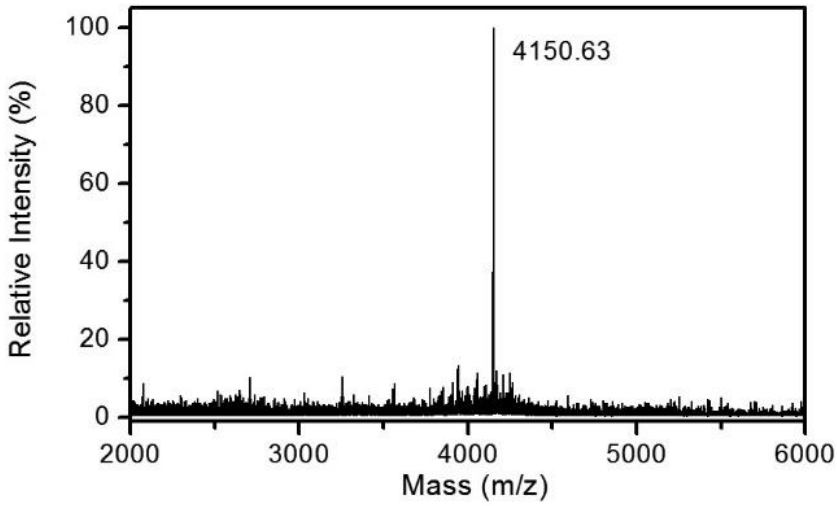

Figure 2.33 MALDI-TOF mass spectrum of a purified peptide **NSII**.

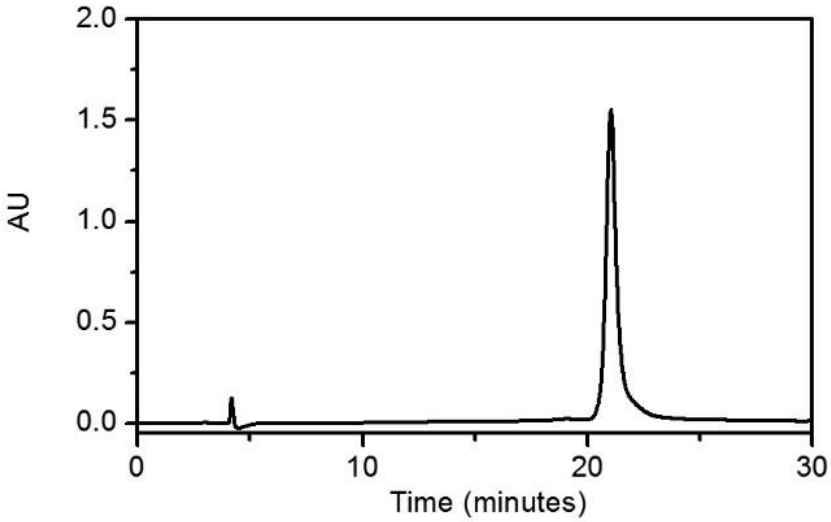

Figure 2.34 Analytical HPLC trace of a purified peptide **NSII***.

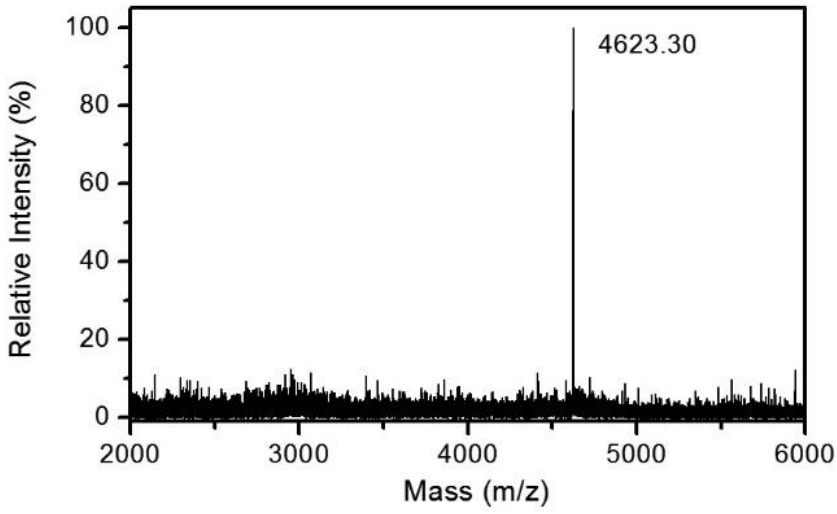

Figure 2.35 MALDI-TOF mass spectrum of a purified peptide **NSII***.

Circular Dichroism Spectropolarimetry. CD spectra were recorded on a Jasco J-810 CD spectropolarimeter in 0.10 mm quartz cells in MOPS buffer (20 mM, pH 7.0). Spectra were recorded from 300 to 190 nm at a scanning rate of 100 nm/min and a resolution of 0.5 nm. CD melting experiments were performed in the temperature range from 5 ℃ to 80 ℃ at a heating rate of 1 ℃/min. The intensity of the CD signal at 224 nm was monitored as a function of temperature. Melting temperatures were obtained from the first derivative of the melting curves.

Flow Linear Dichroism Spectroscopy. Flow linear dichroism spectra were recorded on a JASCO J-810 circular dichroism spectropolarimeter using a microvolume cuvette with a path length of 50 μm and a rotation speed of 2000 rpm to establish Couette flow.[80] The background scattering for each sample was obtained from the LD spectra of samples at 0 rpm. The LD spectra were measured after 5 min of rotation. Solutions of **NSI** were sampled in MOPS buffer (20 mM, pH 7.0) at the indicated concentrations. Type I

collagen from rat tail (Sigma-Aldrich Chemical Co.) was prepared in phosphate buffer (100 mM, pH 7.4) at a concentration of (0.4 mg/mL).

Transmission Electron Microscopy. TEM specimens were prepared from aqueous solutions of **NSI** (2 mg/mL), **NSII** (2.5 mg/mL), or **NSII*** (10 mg/mL) in MOPS buffer (20 mM, pH 7.0). The samples were deposited onto 200 mesh carbon coated copper grids from Electron Microscopy Sciences (Hatfield, PA). After a 2 min incubation period, excess liquid was wicked away and the specimens were stained with an aqueous solution of uranyl acetate (1%). Excess stain was wicked away after incubation on the grid for 30 s. The sample grids were dried under vacuum and stored in a desiccator. TEM measurements were acquired on a Hitachi H-7500 transmission electron microscope at an accelerating voltage of 75 kV.

For cationic gold nanoparticle staining experiments, both the solution of nanoparticles and **NSII** sheets were diluted 20 times with distilled, deionized H_2O. An aliquot (4 μL) of the diluted cationic gold solution was added to a solution (4 μL) of the diluted **NSII** sheets in situ, The mixture was incubated at ambient temperature for 20 min. Excess liquid was wicked away, and the specimens were then stained with uranyl acetate (1%) for 30 s. Excess stain solution was wicked away. Sample grids were dried in vacuum desiccator before TEM investigation. TEM images were recorded as described above.

Streptavidin-tagged gold nanoparticles were diluted 10-20 times with MOPS buffer (20 mM, pH 7.0). An aliquot (4-20 μL) of the diluted streptavidin-gold solution was added to 4 μL of **NSII*** sheets (10 mg/mL) in situ, and was incubated at ambient temperature for 20 min. Excess liquid was wicked away and the sample was washed three times for 5 min

to remove the non-specifically bound streptavidin-gold solution. The specimens were then stained with uranyl acetate (1%) for 30 seconds. Excess stain solution was wicked away. Sample grids were dried in vacuum desiccator before TEM investigation. TEM images were recorded as described above.

Electron Diffraction. Electron diffraction patterns were acquired on either a Hitachi H-7500 transmission electron microscope (Emory University) or an FEI Tecnai G2 12 transmission electron microscope (University of Delaware). Data were acquired from individual **NSI** nanosheets prepared as described above for TEM diffraction pattern acquisition. Adequate camera lengths (1 m for H-7500 and 2.1 m for Tecnai G2 12) were used to expose the small reciprocal lattice, and d-spacings were calculated using the equation: $d = \lambda L/R$, where R is the distance of the diffraction spots, λ denotes the electron wavelength, and L is the camera length. An aluminum polycrystalline standard from Ted Pella, Inc. (Redding, CA) was used to calibrate the camera length.

Atomic Force Microscopy. AFM measurements were performed using either a JEOL JSPM-4200 or MFP-3D-BIO AFM instruments. Aqueous solutions of **NSI** (2 mg/mL) or **NSII** (2.5 mg/mL) in MOPS buffer (20 mM, pH 7.0) were deposited on either a freshly cleaved mica substrate or a pre-cleaned glass coverslip. Silicon AFM tips (MikronMasch) with a force constant (5.4-16 N/m) were used to image the specimens in tapping mode at a scan rate of 1 Hz. A TGZ-20 SiO2 grating was employed for z axis calibration (Ted Pella). For gold nanoparticle binding experiments, a solution of **NSII** nanosheets was deposited on an APTES modified mica substrate was treated with a diluted solution of cationic gold nanoparticles.

Scanning Transmission Electron Microscopy. The STEM data were acquired at Brookhaven National Laboratory (BNL). The STEM instrument operates at 40 keV with a scanning probe of < 0.3 nm diameter produced from a cold field-emission source. Every electron emerging from the specimen is detected by one of the scintillator-photomultiplier detectors collecting 0-15 mRadian (bright field), 15-40 mRadian (small angle dark field) and 40-200 mRadian (large-angle dark field). The large angle signal is proportional to the mass of atoms in the path of the beam. Specimen quality and mass calibration are checked by detailed comparison of the image to the known structure of tobacco mosaic virus (TMV). For mass per area (M/A) measurements, TMV rafts at a theoretical M/A value of 81.9 Da/Å^2 were employed for calibration.

Specimens are deposited on thin carbon (circa 2 nm thick) supported on a thicker holey carbon film mounted on a titanium grid using the wet film, hanging-drop method http://www.bnl.gov/biology/stem/SpecPrepDetails.asp. TMV is added to the grid first as an internal control, followed by injection buffer, then specimen solution (in 20 mM MOPS buffer, pH 7.0) for 1 min, then 10 washes of 20 mM ammonium acetate pH 7.0. Excess solution is wicked from the edge with filter paper between each injection. After the last wash the grid is wicked to a thin layer (circa 1 μm), fast frozen by plunging into liquid nitrogen shush and stored under liquid nitrogen. Grids are freeze-dried overnight in an ion pumped chamber with an efficient cold trap and transferred under vacuum to the STEM cold stage (-160 ℃). Imaging typically uses a dose of 20 el/Å^2 (causing < 5% mass loss, corrected by comparison to TMV).

Mass measurements were performed off line with customized software (PCMass, available at ftp.stem.bnl.gov). The program masks out objects significantly above

background and computes the value for the thin carbon in the remaining areas, which is subtracted, and pixels within the contour of filaments are summed and divided by area to give mass-per-unit area. Accuracy is determined by cleanliness of the background between objects and by counting statistics of the scattered electrons. For TMV the program provides automatic searching and measurement, but manual selection was employed for the thin sheets. PCMass also provides statistics in a database for individual images or groups of images.

Small- and Wide-angle X-ray Scattering Measurements. Synchrotron SAXS/WAXS measurements were performed at the 12-ID-B beamline of Advanced Photon Source at Argonne National Laboratory. A simultaneous SAXS/WAXS setup was utilized and the sample-to-detector distances were set such that the overall scattering momentum transfer, q, range was achieved from 0.005 to 2.4 $Å^{-1}$, where $q = 4\pi\sin\theta/\lambda$, 2θ denoting the scattering angle and λ the x-ray wavelength. The wavelength was set at 1.033 Å during the measurements. Scattered X ray intensities were measured using a Pilatus 2M (DECTRIS Ltd) detector for SAXS and Pilatus 300K for WAXS. SAXS/WAXS measurements were performed on aqueous solutions of peptide **NSI** at a concentration of 4 mg/mL in MOPS buffer (20 mM, pH 7.0) at 25 ℃. A quartz capillary flow cell (1.5 mm diameter) was employed to prevent radiation damage. Twenty images were collected for each sample and buffer. The 2D scattering images were converted to 1D SAXS curves through azimuthally averaging after solid angle correction and then normalizing with the intensity of the transmitted X ray beam, using the software package at beamline 12ID-B. The 1D curves of the samples were averaged and subtracted with the background measured from the corresponding buffers.

Fluorescence Microscopy. An aliquot (100 μL) of a 1.5 mM solution of Alexa 488 dye was reacted with streptavidin (0.5 mg/mL) in 0.1 M sodium bicarbonate for 1 h. The unreacted Alexa 488 dye was removed with phosphate buffered saline (PBS, pH 7.4) in a P-6 gel spin column (Bio-rad) that was pre-equilibrated with PBS buffer. Silicon glass was etched by piranha solution (v/v = 3:7 hydrogen peroxide:sulfuric acid) for 15 min to remove residual organic materials and then functionalized with 2% (3-aminopropyl) trimethoxysilane in acetone for 4 h. An aliquot (200 μL) of biotin-NHS ester (2 mg/mL) in dimethylsulfoxide was added to the amine-modified surface and was incubated for 3 h. After thoroughly rinsing the surface with de-ionized water and acetone, an aliquot (500 μL) of streptavidin (50 μg/mL) in PBS solution was incubated with the biotinylated surface for 1 h. The surface was treated with PBS and MOPS buffers (20 mM, pH 7.0) to remove the unbound streptavidin, and incubated subsequently with a solution (0.5 mg/mL) of the **NSII*** nanosheets in MOPS buffer (20 mM, pH 7.0) for 1 h. A solution (0.5 mL) of Alexa 488 labeled streptavidin (250 nM) was added to the nanosheet bound surface for 1 h, and subsequently rinsed three times with MOPS buffer (20 mM, pH 7.0).

Conventional fluorescence microscopy was performed using a Nikon Eclipse Ti inverted fluorescence microscope equipped with a Nikon 100X oil-immersion objective (numerical aperture (NA) of 1.49) and an electron multiplying charge-coupled device (Photometrics Evolve or Andor iXon). To image the Alexa 488-streptavidin nanosheets, a Nikon mercury lamp was used as excitation source and a FITC cube (λ_{ex}= 480/40 nm; λ_{em}=535/50 nm) was employed for wavelength selection. In addition, reflection interference contrast microscopy (RICM) was performed on the same instrument to

visualize the contact areas of nanosheets on glass surface. The images were acquired with the Evolve EMCCD feature (106.7 nm/pixel) and Andor iXon feature (60 nm/pixel).

2.6 Reference

(1) Govindaraju, T.; Avinash, M. B. *Nanoscale* **2012**, *4*, 6102-6117.

(2) Ariga, K.; Ji, Q.; Hill, J. P.; Bando, Y.; Aono, M. *NPG Asia Mater.* **2012**, *4*, e17.

(3) Hamley, I. W.; Dehsorkhi, A.; Castelletto, V. *Chem. Commun.* **2013**, *49*, 1850-1852.

(4) Hughes, M.; Xu, H.; Frederix, P. W. J. M.; Smith, A. M.; Hunt, N. T.; Tuttle, T.; Kinloch, I. A.; Ulijn, R. V. *Soft Matter.* **2011**, 10032-10038.

(5) Govindaraju, T.; Pandeeswar, M.; Jayaramulu, K.; Jaipuria, G.; Atreya, H. S. *Supramol. Chem.* **2011**, *23*, 487-492.

(6) Nam, K. T.; Shelby, S. A.; Choi, P. H.; Marciel, A. B.; Chen, R.; Tan, L.; Chu, T. K.; Mesch, R. A.; Lee, B. C.; Connolly, M. D.; Kisielowski, C.; Zuckermann, R. N. *Nat. Mater.* **2010**, *9*, 454-460.

(7) Kudirka, R.; Tran, H.; Sanii, B.; Nam, K. T.; Choi, P. H.; Venkateswaran, N.; Chen, R.; Whitelam, S.; Zuckermann, R. N. *Biopolymers* **2011**, *96*, 586-595.

(8) Paige, M. F.; Goh, M. C. *Micron* **2001**, *32*, 355-361.

(9) Fujita, Y.; Kobayashi, K.; Hoshino, T. *J. Electron Microsc.* **1997**, *46*, 321-326.

(10) Kobayashi, K.; Hashimoto, Y.; Hayakawa, T.; Hoshino, T. *J. Ultrastruct. Mol. Struct. Res.* **1988**, *100*, 255-262.

(11) Olsen, B. R. *J. Ultrastruct. Res.* **1967**, *19*, 446-473.

(12) Olsen, B. R. *J. Ultrastruct. Res.* **1967**, *19*, 432-445.

(13) Przybyla, D. E.; Chmielewski, J. *J. Am. Chem. Soc.* **2008**, *130*, 12610-12611.

(14) Pires, M. M.; Przybyla, D. E.; Perez, C. M. R.; Chmielewski, J. *J. Am. Chem. Soc.* **2011**, *133*, 14469-14471.

(15) Pires, M. M.; Chmielewski, J. *J. Am. Chem. Soc.* **2009**, *131*, 2706-2712.

(16) Pires, M. M.; Lee, J.; Ernenwein, D.; Chmielewski, J. *Langmuir* **2012**, *28*, 1993-1997.

(17) Przybyla, D. E.; Rubert Perez, C. M.; Gleaton, J.; Nandwana, V.; Chmielewski, J. *J. Am. Chem. Soc.* **2013**, *135*, 3418-3422.

(18) Hsu, W.; Chen, Y.-L.; Horng, J.-C. *Langmuir* **2012**, *28*, 3194-3199.

(19) Cejas, M. A.; Kinney, W. A.; Chen, C.; Leo, G. C.; Tounge, B. A.; Vinter, J. G.; Joshi, P. P.; Maryanoff, B. E. *J. Am. Chem. Soc.* **2007**, *129*, 2202-2203.

(20) Cejas, M. A.; Kinnney, W. A.; Chen, C.; Vinter, J. G.; Almond, H. R.; Balss, K. M.; Maryanoff, C. A.; Schmidt, U.; Breslav, M.; Mahan, A.; Lacy, E.; Maryanoff, B. E. *Proc. Natl. Acad. Sci. U. S. A.* **2008**, *105*, 8513-8518.

(21) Kar, K.; Ibrar, S.; Nanda, V.; Getz, T. M.; Kunapuli, S. P.; Brodsky, B. *Biochemistry* **2009**, *48*, 7959-7968.

(22) Chen, C. C.; Hsu, W.; Kao, T. C.; Horng, J. C. *Biochemistry* **2011**, *50*, 2381-2383.

(23) Yamazaki, C. M.; Asada, S.; Kitagawa, K.; Koide, T. *Biopolymers* **2008**, *90*, 816-823.

(24) Koide, T.; Homma, D. L.; Asada, S.; Kitagawa, K. *Bioorg. Med. Chem. Lett.* **2005**, *15*, 5230-5233.

(25) Kotch, F. W.; Raines, R. T. *Proc. Natl. Acad. Sci. U. S. A.* **2006**, *103*, 3028-3033.

(26) Rele, S.; Song, Y. H.; Apkarian, R. P.; Qu, Z.; Conticello, V. P.; Chaikof, E. L. *J. Am. Chem. Soc.* **2007**, *129*, 14780-14787.

(27) Chapman, J. A.; Tzaphlidou, M.; Meek, K. M.; Kadler, K. E. *Electron Microsc. Rev.* **1990**, *3*, 143-182.

(28) Kadler, K. E.; Holmes, D. F.; Trotter, J. A.; Chapman, J. A. *Biochem. J.* **1996**, *316* 1-11.

(29) Gauba, V.; Hartgerink, J. D. *J. Am. Chem. Soc.* **2007**, *129*, 15034-15041.

(30) Gauba, V.; Hartgerink, J. D. *J. Am. Chem. Soc.* **2007**, *129*, 2683-2690.

(31) Gauba, V.; Hartgerink, J. D. *J. Am. Chem. Soc.* **2008**, *130*, 7509-7515.

(32) O'Leary, L. E.; Fallas, J. A.; Bakota, E. L.; Kang, M. K.; Hartgerink, J. D. *Nat. Chem.* **2011**, *3*, 821-828.

(33) Umashankara, M.; Babu, I. R.; Ganesh, K. N. *Chem. Commun.* **2003**, 2606-2607.

(34) Babu, I. R.; Ganesh, K. N. *J. Am. Chem. Soc.* **2001**, *123*, 2079-2080.

(35) Hodges, J. A.; Raines, R. T. *J. Am. Chem. Soc.* **2003**, *125*, 9262-9263.

(36) DeRider, M. L.; Wilkens, S. J.; Waddell, M. J.; Bretscher, L. E.; Weinhold, F.; Raines, R. T.; Markley, J. L. *J. Am. Chem. Soc.* **2002**, *124*, 2497-2505.

(37) Bretscher, L. E.; Jenkins, C. L.; Taylor, K. M.; DeRider, M. L.; Raines, R. T. *J. Am. Chem. Soc.* **2001**, *123*, 777-778.

(38) Holmgren, S. K.; Bretscher, L. E.; Taylor, K. M.; Raines, R. T. *Chem. Biol.* **1999**, *6*, 63-70.

(39) Holmgren, S. K.; Taylor, K. M.; Bretscher, L. E.; Raines, R. T. *Nature* **1998**, *392*, 666-667.

(40) Okuyama, K.; Hongo, C.; Fukushima, R.; Wu, G. G.; Narita, H.; Noguchi, K.; Tanaka, Y.; Nishino, N. *Biopolymers* **2004**, *76*, 367-377.

(41) Jiravanichanun, N.; Hongo, C.; Wu, G.; Noguchi, K.; Okuyama, K.; Nishino, N.; Silva, T. *ChemBioChem* **2005**, *6*, 1184-1187.

(42) Hongo, C.; Noguchi, K.; Okuyama, K.; Tanaka, Y.; Nishino, N. *J. Biochem.* **2005**, *138*, 135-144.

(43) Feng, Y. B.; Melacini, G.; Taulane, J. P.; Goodman, M. *J. Am. Chem. Soc.* **1996**, *118*, 10351-10358.

(44) Marrington, R.; Seymour, M.; Rodger, A. *Chirality* **2006**, *18*, 680-690.

(45) Rodger, A.; Marrington, R.; Geeves, M. A.; Hicks, M.; de Alwis, L.; Halsall, D. J.; Dafforn, T. R. *Phys. Chem. Chem. Phys.* **2006**, *8*, 3161-3171.

(46) Bulheller, B. M.; Rodger, A.; Hicks, M. R.; Dafforn, T. R.; Serpell, L. C.; Marshall, K. E.; Bromley, E. H.; King, P. J.; Channon, K. J.; Woolfson, D. N.; Hirst, J. D. *J. Am. Chem. Soc.* **2009**, *131*, 13305-13314.

(47) Okuyama, K. *Connect. Tissue Res.* **2008**, *49*, 299-310.

(48) Okuyama, K.; Xu, X.; Iguchi, M.; Noguchi, K. *Biopolymers* **2006**, *84*, 181-191.

(49) Beaucage, G. *J. Appl. Cryst.* **1996**, *29*, 134-146.

(50) Okuyama, K.; Miyama, K.; Mizuno, K.; Bachinger, H. P. *Biopolymers* **2012**, *97*, 607-616.

(51) Kramer, R. Z.; Venugopal, M. G.; Bella, J.; Mayville, P.; Brodsky, B.; Berman, H. M. *J. Mol. Biol.* **2000**, *301*, 1191-1205.

(52) Bella, J.; Eaton, M.; Brodsky, B.; Berman, H. M. *Science* **1994**, *266*, 75-81.

(53) Chanzy, H.; Franc, J. M.; Herbage, D. *Biochem. J.* **1976**, *153*, 139-140.

(54) Okuyama, K.; Hongo, C.; Wu, G.; Mizuno, K.; Noguchi, K.; Ebisuzaki, S.; Tanaka, Y.; Nishino, N.; Bachinger, H. P. *Biopolymers* **2009**, *91*, 361-372.

(55) Okuyama, K.; Miyama, K.; Morimoto, T.; Masakiyo, K.; Mizuno, K.; Bachinger, H. P. *Biopolymers* **2011**, *95*, 628-640.

(56) Okuyama, K.; Miyama, K.; Morimoto, T.; Masakiyo, K.; Mizuno, K.; Bachinger, H. P. *Biopolymers* **2011**, *95*, 628-640.

(57) Baxa, U.; Keller, P. W.; Cheng, N.; Wall, J. S.; Steven, A. C. *Mol. Microbiol.* **2011**, *79*, 523-532.

(58) Goldsbury, C.; Baxa, U.; Simon, M. N.; Steven, A. C.; Engel, A.; Wall, J. S.; Aebi, U.; Muller, S. A. *J. Struct. Biol.* **2011**, *173*, 1-13.

(59) Hodgkinson, J. L.; Horsley, A.; Stabat, D.; Simon, M.; Johnson, S.; da Fonseca, P. C.; Morris, E. P.; Wall, J. S.; Lea, S. M.; Blocker, A. J. *Nat. Struct. Mol. Biol.* **2009**, *16*, 477-485.

(60) Sen, A.; Baxa, U.; Simon, M. N.; Wall, J. S.; Sabate, R.; Saupe, S. J.; Steven, A. C. *J. Biol. Chem.* **2007**, *282*, 5545-5550.

(61) Baxa, U.; Taylor, K. L.; Wall, J. S.; Simon, M. N.; Cheng, N.; Wickner, R. B.; Steven, A. C. *J. Biol. Chem.* **2003**, *278*, 43717-43727.

(62) Castelletto, V.; Hamley, I. W.; Stain, C.; Connon, C. *Langmuir* **2012**, *28*, 12575-12580.

(63) Yin, P.; Hariadi, R. F.; Sahu, S.; Choi, H. M.; Park, S. H.; Labean, T. H.; Reif, J. H. *Science* **2008**, *321*, 824-826.

(64) Rothemund, P. W. *Nature* **2006**, *440*, 297-302.

(65) Wei, B.; Dai, M.; Yin, P. *Nature* **2012**, *485*, 623-626.

(66) Lin, C.; Liu, Y.; Rinker, S.; Yan, H. *ChemPhysChem* **2006**, *7*, 1641-1647.

(67) Ke, Y.; Ong, L. L.; Shih, W. M.; Yin, P. *Science* **2012**, *338*, 1177-1183.

(68) Gradisar, H.; Bozic, S.; Doles, T.; Vengust, D.; Hafner-Bratkovic, I.; Mertelj, A.; Webb, B.; Sali, A.; Klavzar, S.; Jerala, R. *Nat. Chem. Biol.* **2013**, *9*, 362-366.

(69) Sleytr, U. B.; Sara, M.; Messner, P.; Pum, D. *J. Cell. Biochem.* **1994**, *56*, 171-176.

(70) Schuster, B.; Sleytr, U. B. *Methods Mol. Biol.* **2013**, *996*, 153-175.

(71) Xu, F.; Khan, I. J.; McGuinness, K.; Parmar, A. S.; Silva, T.; Murthy, N. S.; Nanda, V. *J. Am. Chem. Soc.* **2013**, *135*, 18762-18765.

(72) Pandya, M. J.; Spooner, G. M.; Sunde, M.; Thorpe, J. R.; Rodger, A.; Woolfson, D. N. *Biochemistry* **2000**, *39*, 8728-8734.

(73) Ryadnov, M. G.; Woolfson, D. N. *Angew. Chem., Int. Ed.* **2003**, *42*, 3021-3023.

(74) Ryadnov, M. G.; Woolfson, D. N. *Nat. Mater.* **2003**, *2*, 329-332.

(75) Papapostolou, D.; Smith, A. M.; Atkins, E. D.; Oliver, S. J.; Ryadnov, M. G.; Serpell, L. C.; Woolfson, D. N. *Proc. Natl. Acad. Sci. U. S. A.* **2007**, *104*, 10853-10858.

(76) Sharp, T. H.; Bruning, M.; Mantell, J.; Sessions, R. B.; Thomson, A. R.; Zaccai, N. R.; Brady, R. L.; Verkade, P.; Woolfson, D. N. *Proc. Natl. Acad. Sci. U. S. A.* **2012**, *109*, 13266-13271.

(77) Zhang, S.; Holmes, T.; Lockshin, C.; Rich, A. *Proc. Natl. Acad. Sci. U. S. A.* **1993**, *90*, 3334-3338.

(78) Marini, D. M.; Hwang, W.; Lauffenburger, D. A.; Zhang, S. G.; Kamm, R. D. *Nano Lett.* **2002**, *2*, 295-299.

(79) Swanekamp, R. J.; DiMaio, J. T. M.; Bowerman, C. J.; Nilsson, B. L. *J. Am. Chem. Soc.* **2012**, *134*, 5556-5559.

(80) Marrington, R.; Dafforn, T. R.; Halsall, D. J.; MacDonald, J. I.; Hicks, M.; Rodger, A. *The Analyst* **2005**, *130*, 1608-1616.

3 Structurally homogeneous nanosheets from self-assembly of a collagen-mimetic peptide

3.1 Introduction

In the last section, we described the design of a collagen-mimetic peptide, **NSI** that self-assembled into structurally defined nano-scale sheets.[1] The sequence of peptide **NSI** encompassed three sequential blocks of identical length with complementary electrostatic properties comprising positively charged, neutral, and negatively charged (Xaa-Yaa-Gly) triads (Figure 3.1).[1-3] The positively charged, non-canonical imino acid, (2*S*, 4*R*)-4-aminoproline (Amp),[4-6] was placed at the Yaa positions of the first block, in order to direct Coulombic interactions between oppositely charged residues located on structurally adjacent triple helices. The underlying structure of the **NSI** nanosheets was based on layered packing of perpendicularly oriented collagen triple helices into a two-dimensional tetragonal lattice. However, the resultant nanosheets were highly polymorphic in both the lateral (x/y) dimension and the stacking (z) dimension. The wide dispersion in nanosheet sizes presents a challenge to the development of applications for these materials as two-dimensional (2D) nanoarchitectonic structural platforms.[7,8] We describe herein a modification of the **NSI** sequence to create a peptide, **NSIII**, which self-assembles into nanosheets that display homogeneity in both lateral sheet dimension and thickness.

3.2 Nanosheet sequence design

The sequence of peptide **NSIII** differs from the corresponding sequence of **NSI** in that the epimeric non-canonical imino acid (2S, 4S)-4-aminoproline (amp) was employed in place of (2S, 4R)-4-aminoproline (Amp) as the positively charged residue (Figure 3.1). These two imino acids display preferences for opposite ring puckers, C^{γ}-endo and C^{γ}-exo, respectively, of the pyrrolidine side chain.[4-6] Crystallographic analyses of collagen model peptides have indicated that the most common conformation for imino acid residues at the Xaa and Yaa positions are the C^{γ}-endo ring pucker and the C^{γ}-exo ring pucker, respectively.[9-14] Therefore, the amp residue in the sequence of **NSIII** was encoded within the Xaa positions of the respective triad sequences. To compensate, the glutamic acid (Glu) residues were moved to Yaa positions of **NSIII**. The triblock architecture of peptide **NSI** sequence was strictly maintained in **NSIII** such that direct structural comparisons could be made between these two peptide systems.

a) **NSI:** $(Pro\text{-}Amp\text{-}Gly)_4$–$(Pro\text{-}Hyp\text{-}Gly)_4$–$(Glu\text{-}Hyp\text{-}Gly)_4$
NSIII: $(amp\text{-}Hyp\text{-}Gly)_4$–$(Pro\text{-}Hyp\text{-}Gly)_4$–$(Pro\text{-}Glu\text{-}Gly)_4$

b)

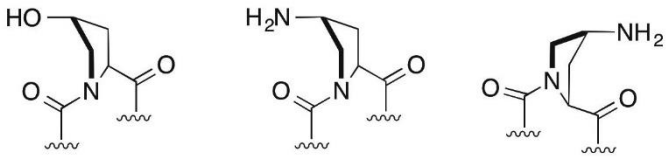

(4*R*)-Hyp (4*R*)-Amp (Amp) (4*S*)-Amp (amp)

Figure 3.1 (A) Sequences of peptides **NSI** and **NSIII**. (B) Structures and preferred ring pucker conformers of imino acid derivatives.

3.3 Results and discussion

3.3.1 Circular dichroism

Circular dichroism (CD) spectropolarimetry was employed to assess the conformation and thermodynamic stability of peptide **NSIII** in solution under conditions identical to those that promoted self-assembly of peptide **NSI.** (Figure 3.2) Peptide **NSIII** (4 mg/mL) in MOPS buffer (20 mM, pH 7.0) displayed the classic spectroscopic signature of the collagen triple helix with a minimum at 198 nm and a maximum at 224 nm. Surprisingly, the melting temperature (T_m) of **NSIII** was only slightly lower (28 ℃) than that of **NSI** (32 ℃) under identical conditions, which differs from the previously observed influence of similar substitutions on the thermal stability of collagen-mimetic model peptides.[4,5,15-23] The triple helical secondary structure of **NSIII** developed over a period of several days in aqueous solution, as judged by the increase in intensity of the CD signal at 224 nm. (Figure 3.4 and 3.5) However, the position of the cooperative melting transition remained constant, which suggested that triple helix formation coincided with a higher order self-assembly process, as observed previously for peptide **NSI**.

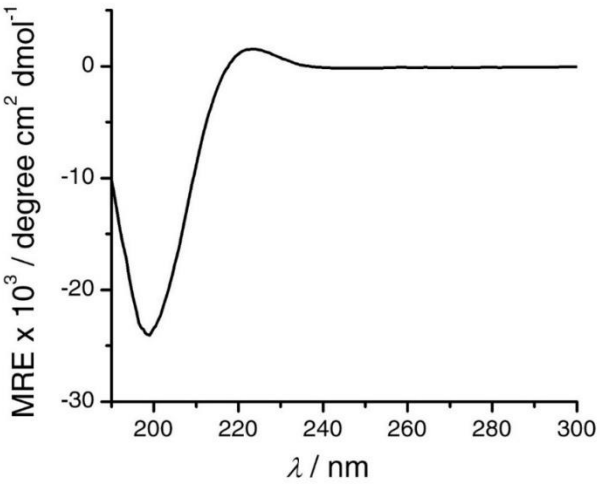

Figure 3.2 CD spectra of an aqueous solution of peptide **NSIII**.

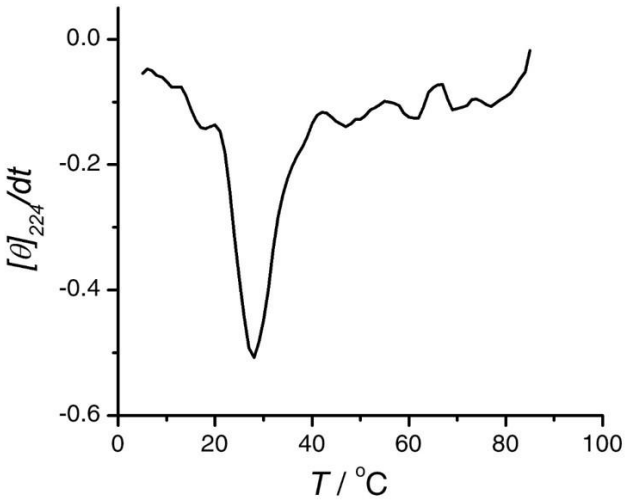

Figure 3.3 First derivative of the CD melting curve derived from monitoring the maximal signal as a function of temperature for an aqueous solution of **NSIII**.

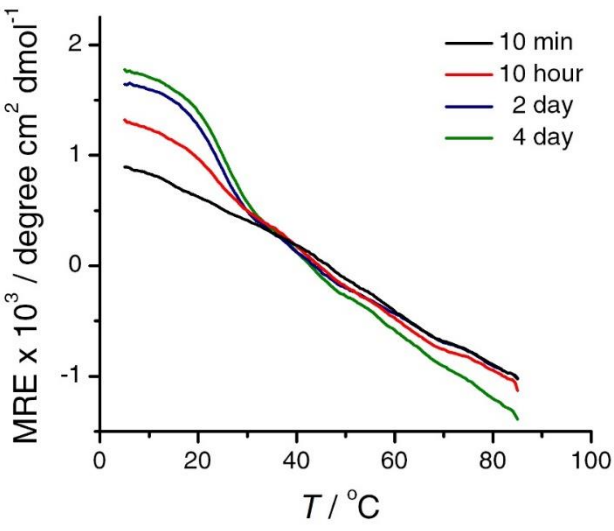

Figure 3.4 CD melting curves of aqueous solutions of **NSIII** buffer as a function of time after dissolution.

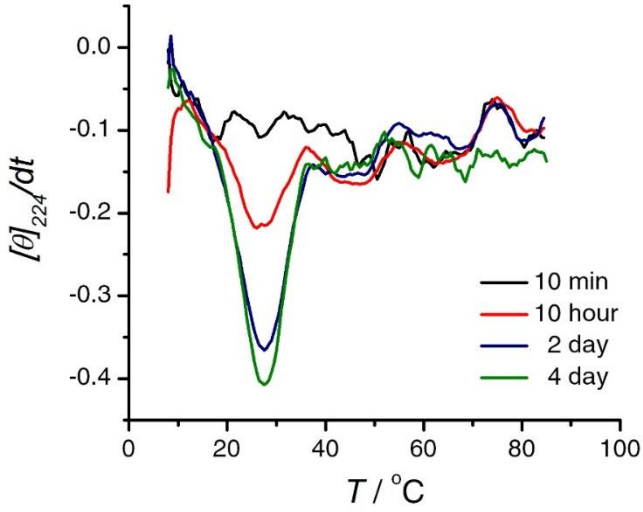

Figure 3.5 First derivative of the corresponding melting curves as a function of time after dissolution.

3.3.2 Transmission Electron Microscopy

TEM image analysis (Figure 3.6 scar bar = 1 μm) demonstrated that peptide **NSIII** (4 mg/mL) self-assembles into nanosheets at 4 °C from MOPS buffer (20 mM, pH 7.0); conditions that are similar to those employed for self-assembly of nanosheets from peptide **NSI**[1]. However, in contrast to the assemblies observed previously for **NSI**, a homogeneous population nanosheets was observed for **NSIII**. Measurement of the diagonal length across the nanosheet surface indicated a narrow range of values for the **NSIII** assemblies (mean distance = 679 ± 57 nm), which was interpreted as an indication of the homogeneity of the assemblies. (Figure 3.7 and 3.8) In comparison, a very broad distribution of sheet diagonal values (1-15 μm) was measured for the corresponding **NSI** nanosheets.

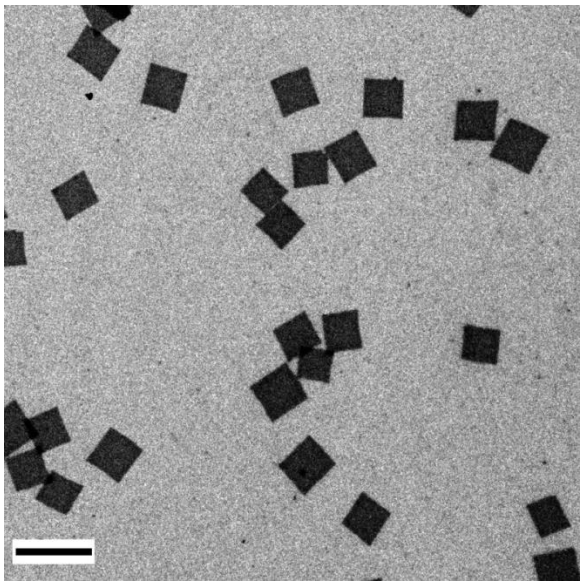

Figure 3.6 TEM image of **NSIII** nanosheets.

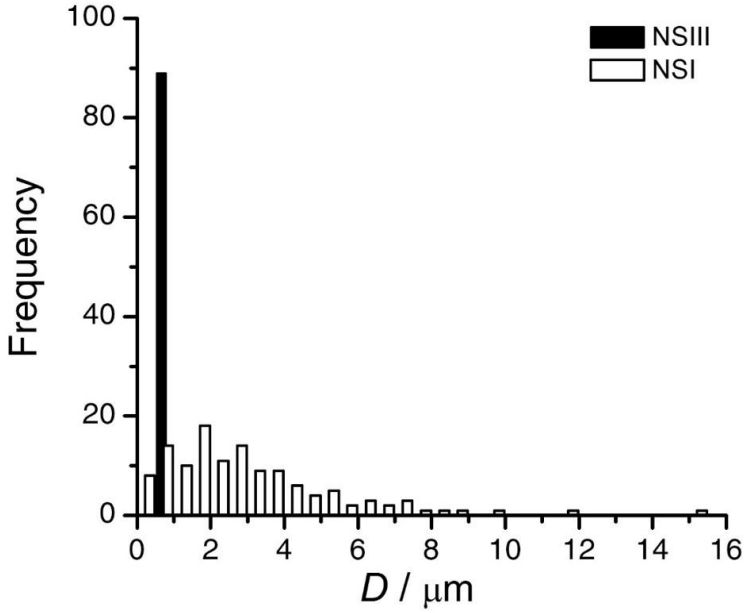

Figure 3.7 Histogram of diagonal length values for representative populations of **NSIII** and **NSI** nanosheets from measurements in the corresponding TEM images.

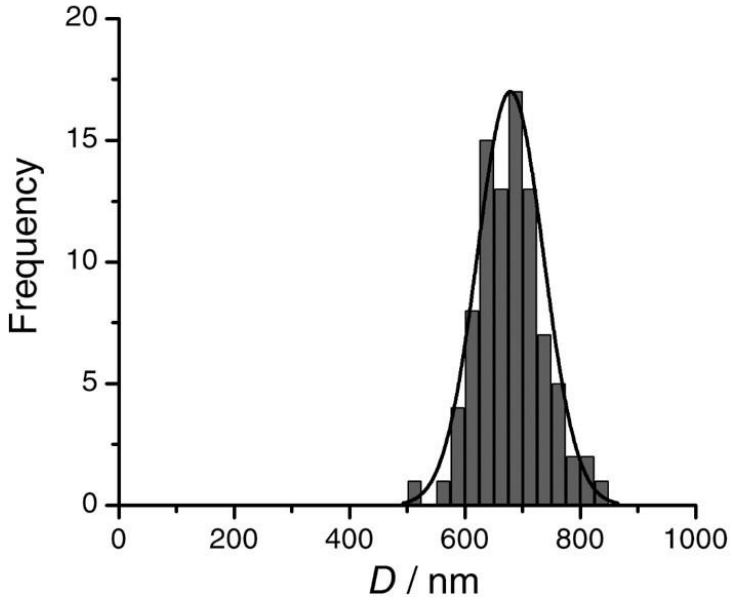

Figure 3.8 Histogram of diagonal lengths of **NSIII** nanosheets from measurements in the corresponding TEM images.

3.3.3 Atomic force microscopy

AFM analysis was employed to estimate the height of nanosheets of **NSIII**. A thickness of 9.6 ± 0.4 nm was observed for the **NSIII** nanosheets, (Figure 3.9 scale bar = 300 nm) which compared well to the value of 8.8 ± 0.8 nm measured for single-layer nanosheets of **NSI**. A theoretical sheet thickness of 10.3 nm (36 residues x 0.286 nm rise/residue for collagen triple helices)[24,25] was calculated for single-layer nanosheets of **NSI** and **NSIII**, which correlates well with the height values measured from tapping mode AFM imaging under dry conditions. The AFM data support a structure for the **NSIII** nanosheets in which collagen triple helices pack into a single layer without stacking in the z direction. In contrast, single-layer nanosheets of **NSI** are relatively rare. A wide

dispersion of height values (10-250 nm) is observed from AFM measurements on the **NSI** nanosheets.[1] These results suggested that multilayer nanosheets are the norm for **NSI**, while all of the observed **NSIII** nanosheets corresponded to single layers of collagen triple helices.

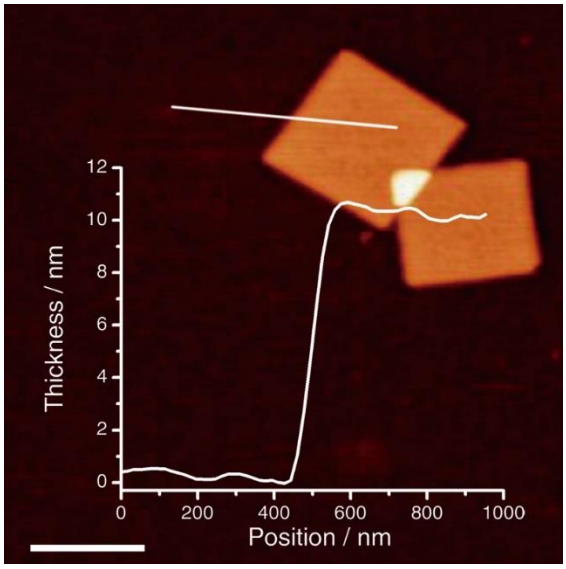

Figure 3.9 AFM image and height profile of single-layer nanosheets of **NSIII**.

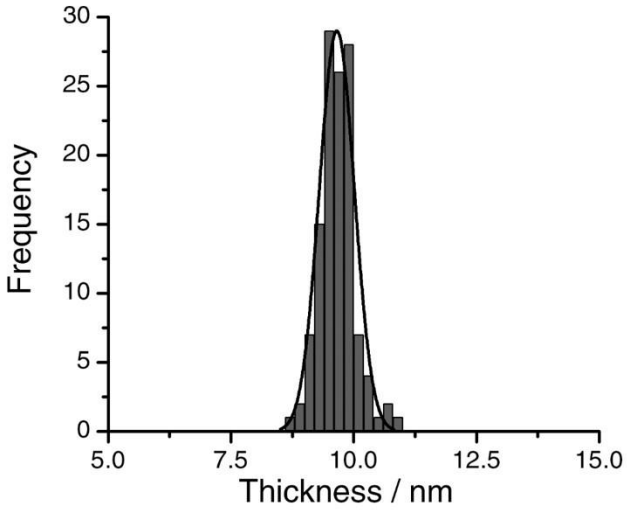

Figure 3.10 AFM height histogram for single-layer nanosheets of **NSIII**.

TEM and AFM image analysis indicated that the nanosheets formed over a concentration rage from 2-10 mg/mL in MOPS buffer. Moreover, the lateral size of the nanosheets did not vary significantly within this concentration rage. The population of nanosheets appeared to increase with time in a manner commensurate with the increase in the intensity of the CD signal. Lower initial concentrations of **NSIII** (less than 0.5 mg/mL) did not support nanosheet formation. Dilution of nanosheets (4 mg/mL) to non-permissive concentrations (0.25 mg/mL) resulted in their dis-assembly with concomitant diminution of the CD signal.(Figure 3.11)

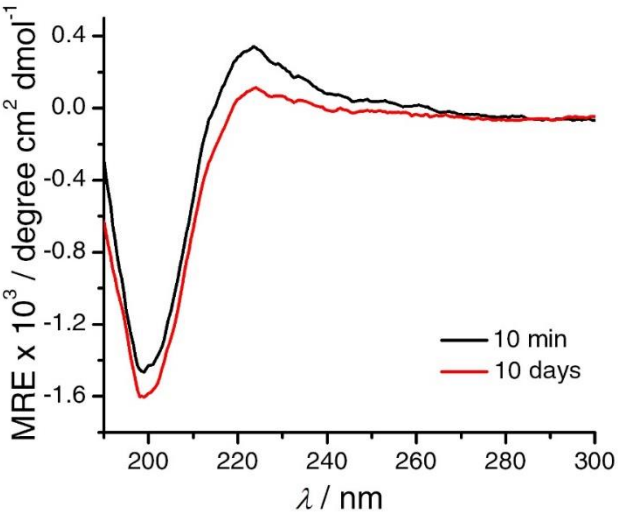

Figure 3.11 CD spectra of mature **NSIII** nanosheets as a function of time after dilution.

3.3.4 Dynamic light scattering measurements

Dynamic light scattering (DLS) measurements of the **NSIII** nanosheets confirmed this observation, in that a narrow distribution of nanosheets was observed in solution under

the self-assembly conditions (Figure 3.12). While the Stokes-Einstein relationship does not obtain for two-dimensional objects, the population of nanosheets could be fit to a single curve that was consistent with a uniform size distribution of self-assembled species. The temperature profile of the dynamic light scattering response indicated that both the intensity of scattered light and the apparent hydrodynamic radius (R) underwent a sharp transition as the temperature increased through the T_m of the collagen triple helix. (Figure 3.13) The observed transition was consistent with dis-assembly of the nanosheets into individual non-associated **NSIII** peptides due to melting of the triple helices.

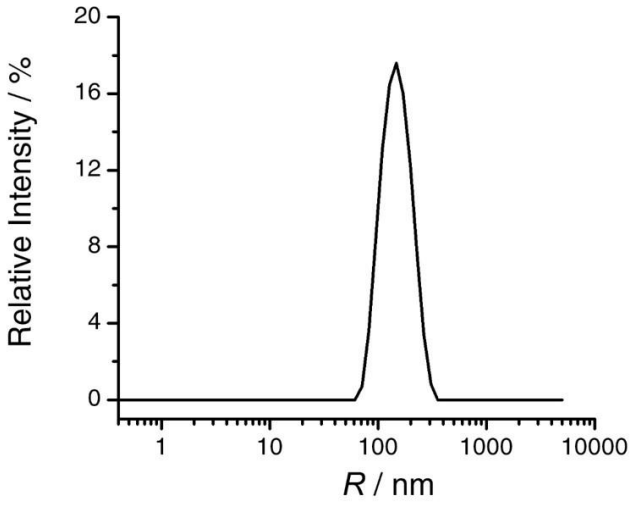

Figure 3.12 DLS measurement of an aqueous solution of **NSIII** nanosheets.

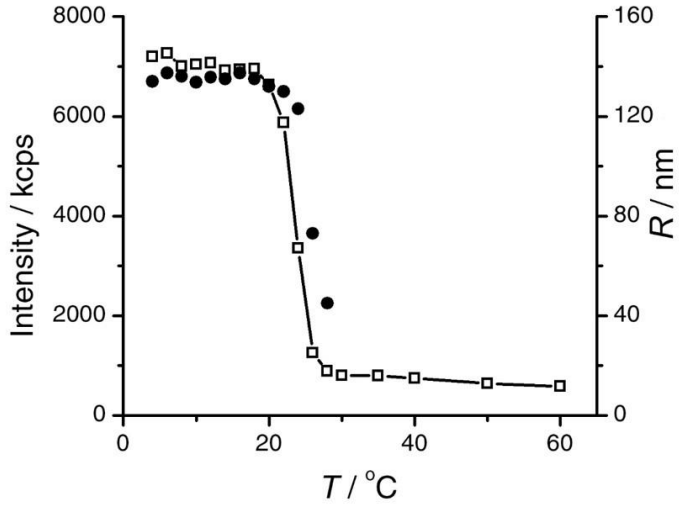

Figure 3.13 Temperature dependence of the intensity of scattered light and calculated hydrodynamic radius for a solution of **NSIII** nanosheets.

3.3.5 Solution X-ray scattering and electron diffraction measurements

Synchrotron SAXS/WAXS analysis (Figure 3.15) of a dilute solution of **NSIII** (4 mg/mL) displayed a scattering intensity profile that was similar to that observed for nanosheets of **NSI**. Form factor scattering was convoluted with sharp peaks that could be attributed to Bragg diffraction in the high q, that is, small d-spacing, region of the scattering curve. The data in the Guinier region ($q_{max}*R_c \leq 1.0$) could be fit to a model for sheet-like forms. (Figure 3.14)[26] A value of 107 ± 4 Å for the sheet thickness can be calculated from the Guinier plot (Figure 3.14), which compares well to the height from AFM measurements as well as the length of the **NSIII** peptide projected onto a collagen triple helix (see above). In contrast, the polydispersity of the **NSI** nanosheets precluded determination of the sheet thickness from Guinier analysis of the SAXS data. The oscillating features in the q range of 0.02-0.3 $Å^{-1}$ arise from the thickness dimension of the

nanosheet and provide information on sheet thickness and its distribution. The position of the first oscillation minima is circa 0.058-0.060 $Å^{-1}$, corresponding to a thickness of 105-108 Å. The attenuation of the scattering oscillation indicates a dispersion on the thickness, which is estimated no more than ± 13 Å, the standard deviation of a normal Gaussian distribution (Figure 3.15).

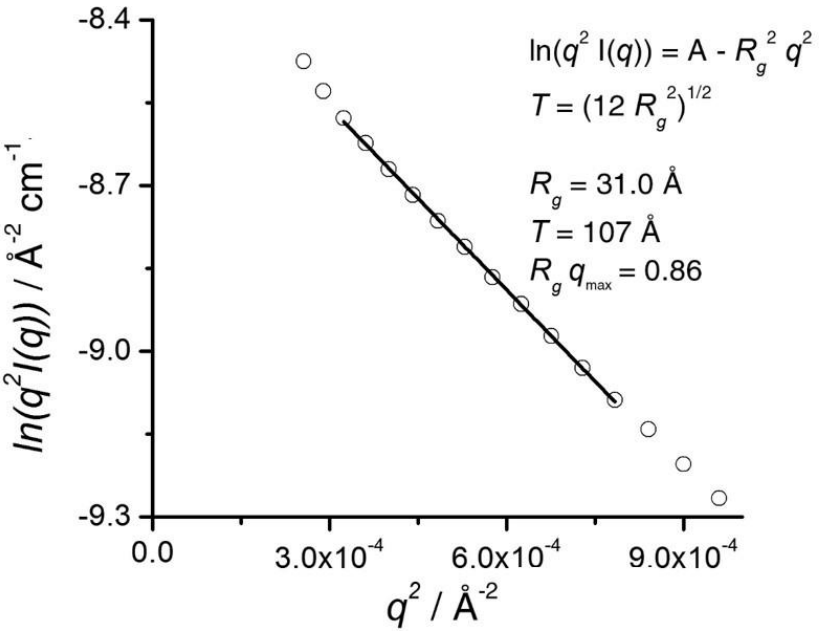

Figure 3.14 Guinier plot (sphere) of **NSIII** nanosheets in aqueous solutions and the calculated Guinier fit (line) for a sheet-like form.

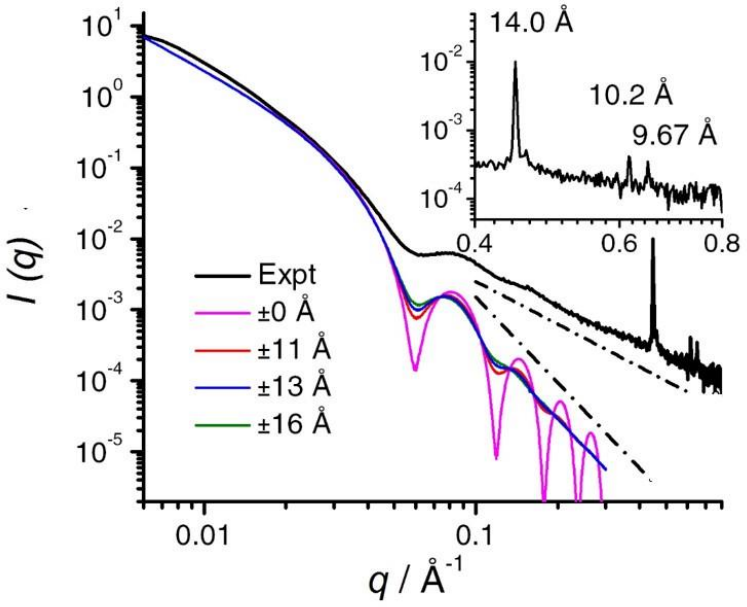

Figure 3.15 Thickness variation analysis for **NSIII** nanosheets in aequous solutions. The black curve is the experimental data, and the others are the simulated SAXS curves using a homogenous disc model with various thickness standard deviation.

The Bragg diffraction peaks observed in the high q region of the intensity plot support a high degree of internal order for the nanosheets, albeit with a different internal structure than observed for **NSI** sheets. For the **NSI** nanosheets, diffraction peaks were observed in the scattering curve at q value of 0.405 $Å^{-1}$ and 0.573 $Å^{-1}$, which correspond to azimuthally averaged d-spacings of 15.5 Å and 11.0 Å.[1] These d-spacings were interpreted in terms of a tetragonal 2D lattice, which was confirmed with electron diffraction. In comparison, three diffractions peaks were observed in the SAXS scattering profile of the **NSIII** nanosheets at q values of 0.448 $Å^{-1}$ (d = 14.0 Å), 0.617 $Å^{-1}$ (d = 10.2 Å), and 0.650 $Å^{-1}$ (d = 9.67 Å). The inequivalent values of the latter two spacings and the

geometrical relationship between the three d-spacings suggested that **NSIII** does not pack into the same tetragonal lattice as **NSI**. Electron diffraction confirmed the lattice spacing (14 Å) of the major diffraction lattice (Figure 3.16), although the diffraction patterns from isolated sheets could not be observed due to sheet overlap and sensitivity to radiation damage. A structural model for the **NSIII** nanosheets was constructed from this data. (Figure 3.17) This model compares well to that for the **NSI** nanosheets with the exception that the 2D-lattice of the **NSIII** nanosheets is slightly distorted from tetragonal and the unit lattice undergoes contraction with respect to the **NSI** nanosheets.

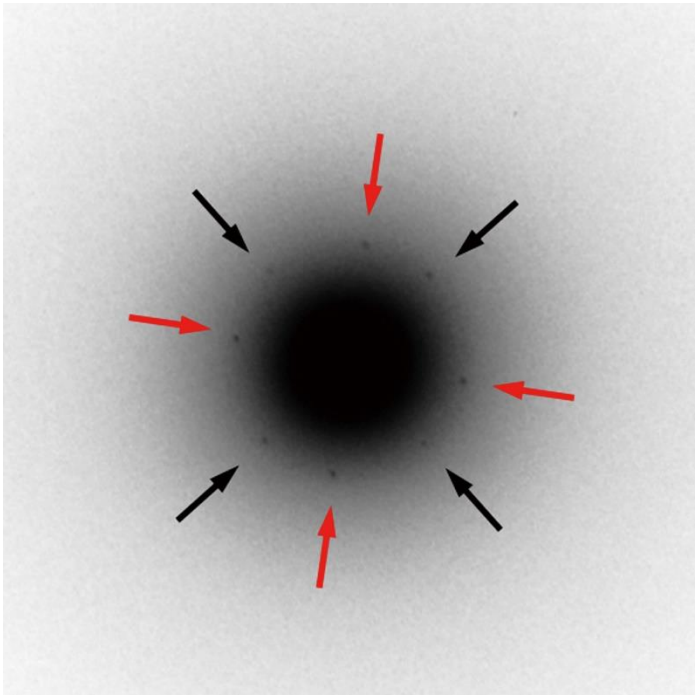

Figure 3.16 Electron diffraction pattern for two overlapping **NSIII** nanosheets. Diffraction spots were observed for each of the two major lattices (red and black arrows).

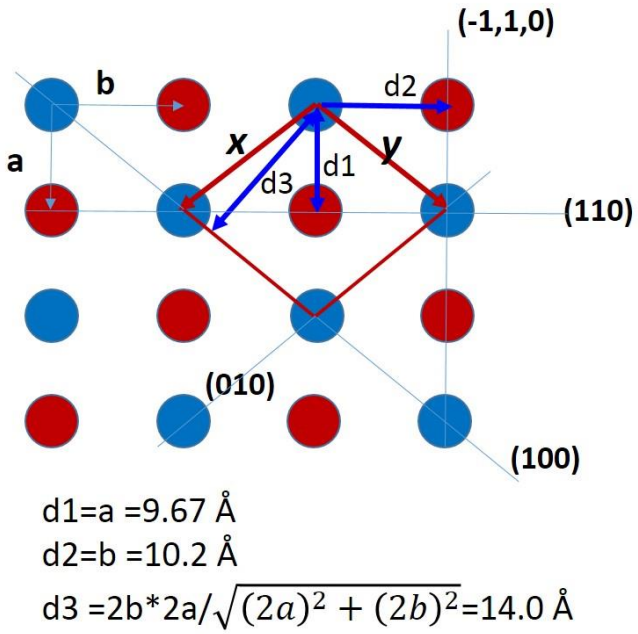

Figure 3.17 Proposed structural model of the 2D lattice for **NSIII** nanosheets in a distorted tetragonal arrangement of anti-parallel triple helices.

3.3.6 Energy frustration mechanism

The structural homogeneity of the **NSIII** nanosheets is striking in comparison to the polydispersity of the corresponding **NSI** nanosheets. The difference in nanosheet morphology between **NSI** and **NSIII** must be attributable to the relatively minor differences in amino acid sequence between the respective peptides. The imino acids (2S, 4S)-4-aminoproline (amp) and (2S, 4R)-4-aminoproline (Amp) posit different ring puckers, C^{γ}-endo and C^{γ}-exo, respectively, within small molecule model compounds.[4-6] These ring puckers are compatible with the preferred conformations of the pyrrolidine rings of the imino acid residues at the Xaa ($\chi_1 \approx 25^{o}$) and Yaa ($\chi_1 \approx -25^{o}$) positions, respectively, within the collagen triple helical structures.[12-14] Although high resolution structural

information is not available for collagen-mimetic peptides containing either Amp or amp residues, the structure of a collagen-mimietic peptide [(Pro-Hyp-Gly)$_4$(hyp-Pro-Gly)$_2$(Pro-Hyp-Gly)$_4$], **1**, has been determined crystallographically in which the isosteric (2S, 4S)-4-hydroxyproline (hyp) and (2S, 4R)-4-hydroxyproline (Hyp) residues occupy Xaa and Yaa positions, respectively, within a triple helix.[27]

The Hyp residues in peptide **1** display a nearly ideal C$^\gamma$-exo ring pucker ($\chi_1 \approx -25^o$), as observed previously in a number of reported structures of collagen-mimetic peptides.[9-14] In contrast, the hyp residues display considerable conformational heterogeneity. A significant percentage of hyp residues (circa 30%) within the structural model for **1** adopt the stereoelectronically unfavorable C$^\gamma$-exo ring pucker at the Xaa position. The remaining hyp residues adopt a structurally distorted C$^\gamma$-endo ring pucker pucker ($\chi_1 \approx 16^o$), presumably to alleviate a sterically unfavorable interaction between the γ-hydroxyl group and the pyrrolidine ring of a Hyp residue on a structurally adjacent peptide within the triple helix.

In analogy to the Hyp residues at the Yaa positions in the sequence of peptide **1**, the stereoelectronically similar Amp residues within **NSI** should adopt a C$^\gamma$-endo ring pucker that favors a typical triple helical collagen conformation. Conversely, the amp residues in the Xaa positions of **NSIII** should recapitulate the conformational properties of the hyp residues of peptide **1**, which would result in stereoelectronically or sterically unfavorable confinement of the substituted pyrrolidine rings with concomitant structural distortion of the triple helix. The conformational differences between the respective triple helices should manifest themselves in terms of differences in electrostatic interactions

between charged residues on adjacent protomers within the 2D lattices of **NSIII** relative to **NSI**.

We propose that the difference in morphology between the **NSI** and **NSIII** nanosheets can be understood in terms of the geometric requirements for packing of the chiral rod-like protomers within the respective 2D lattices. Self-assembly in each case coincides with the formation of the triple helical structure. The extent of self-association depends on a balance between the Coulombic energy of attraction between oppositely charged residues and the energy penalty associated with distortion of the local triple helical conformation to promote packing into the 2D lattice.

In the case of the **NSIII** nanosheets, local conformational distortion of the triple helix occurs due to the presence of the amp residues. The dimensions of the 2D lattice of the **NSIII** nanosheets suggest that closer contact between triple helical protomers may be required to promote the optimal electrostatic interactions. Of note in this regard, the 2D lattice of **NSIII** is contracted in comparison not only to the **NSI** nanosheets but also to pseudotetragonal crystal structures of collagen model peptides.[12-14,28,29] The resultant crystalline order cannot be sustained over large dimensions and frustrates lateral growth as well as sheet stacking. Energetic arguments based on geometrical packing requirements have been invoked account for restrictions in the dimensions of para-crystalline peptide-based assemblies, including the homogeneity of lateral diameter in type I collagen fibers[30] and synthetic α-helical coiled-coil assemblies[31,32] as well as the finite degree of lamination of β-sheet fibrils[33]. In contrast, the local triple helical conformation of **NSI** should be subject to less significant structural distortion owing to the presence of the stereoelectronically preferred Amp residue. As a consequence, the triple helical protomers

of **NSI** undergo minimal distortion owing to the geometrical packing requirements of the 2D lattice, which should promote lateral growth and subsequent sheet stacking.

3.4 Summary

In summary, the disparity in morphology between **NSI** and **NSIII** nanosheets suggests that the geometrical requirements associated with packing of chiral protomers can exert a significant influence on the structure of the resultant assemblies.[34] Manipulation of these quaternary interactions may represent an effective mechanism to control the structure and function of synthetic self-assembled materials. Sequence defined and structurally regular peptide-based materials manifest complex, owing to the complexity of interactions that are manifested, offer a rich test-bed to explore the implications of this hypothesis.

3.5 Materials and methods

Materials. Chemical reagents were purchased from Sigma-Aldrich Chemical Co. (St. Louis, MO) or Anaspec, Inc. (Fremont, CA), unless otherwise noted. (2S, 4S)-Boc-4-amino-1-Fmoc-pyrrolidine-2-carboxylic acid (amp) was purchased from Ambinter (Orléans, France). Fmoc-Gly-PEG-PS resin for solid-phase synthesis was purchased from Applied Biosystems, Inc. (Foster City, NY).

Peptide Synthesis. Peptides **NSIII** was prepared as the uncapped derivative using microwave-assisted synthesis on a CEM Liberty solid-phase peptide synthesis instrument using an Fmoc-Gly-PEG-PS resin. Standard Fmoc protection chemistry was employed with coupling cycles based on HBTU/DIEA-mediated activation protocols and base-induced deprotection (20 % piperidine in DMF with 0.1 M HOBt) of the Fmoc group. Peptide was purified via RP-HPLC on a C18 column with a gradient of water-acetonitrile with 0.1% trifluoroacetic acid. The target fractions were collected and lyophilized. The mass and purity were analyzed by matrix assisted laser desorption/ionization (MALDI) mass spectrometry and analytical high performance liquid chromatography (HPLC), respectively. (Figure 3.18 and 3.19) Peptide **NSIII** was dialyzed against deionized water thoroughly to remove residual trifluoroacetate (MWCO = 2,000 Da). The resulting peptide was lyophilized, and stored at -20 ℃. Peptide **NSIII** was dissolved in MOPS buffer (20 mM, pH 7.0). Solution concentrations were determined from the measured mass of peptide. Samples were thermally annealed at 75 ^{o}C for 45 min, and gradually cooled to ambient temperature and then incubate at 4 ℃.

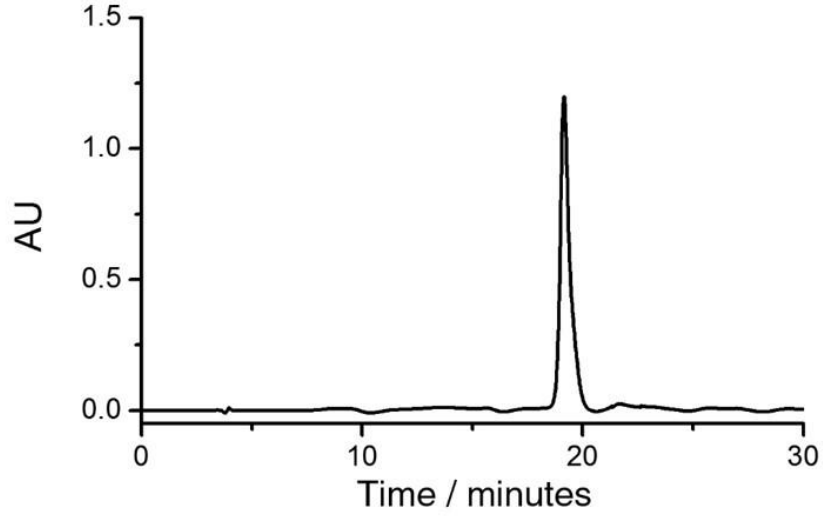

Figure 3.18 Analytical HPLC trace of a purified peptide **NSIII**.

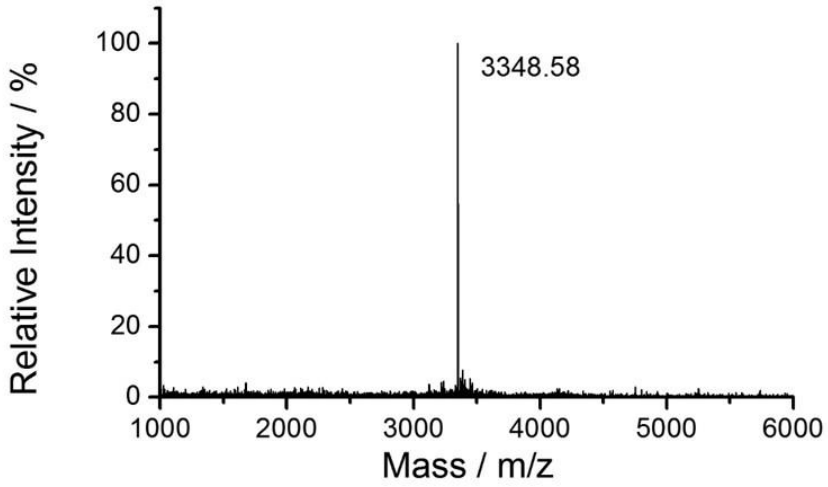

Figure 3.19 MALDI-TOF mass spectrum of a purified peptide **NSIII**.

Circular Dichroism Spectropolarimetry. CD spectra were recorded on a Jasco J-810 CD spectropolarimeter in 0.10 mm quartz cells in MOPS buffer (20 mM, pH 7.0). Spectra were recorded from 300 to 190 nm at a scanning rate of 100 nm/min and a

resolution of 0.5 nm. CD melting experiments were performed in the temperature range from 5 ℃ to 85 ℃ at a heating rate of 1 ℃/min. The intensity of the CD signal at 224 nm was monitored as a function of temperature. Melting temperatures were obtained from the first derivative of the melting curves.

Transmission Electron Microscopy. TEM specimens were prepared from aqueous solutions of **NSIII** (4 mg/mL) in MOPS buffer (20 mM, pH 7.0). The samples were deposited onto 200 mesh carbon coated copper grids from Electron Microscopy Sciences (Hatfield, PA). After a 2 min incubation period, excess liquid was wicked away and the specimens were stained with an aqueous solution of uranyl acetate (1%). Excess stain was wicked away after incubation on the grid for 30 s. The sample grids were dried under vacuum and stored in a desiccator. TEM measurements were acquired on a Hitachi H-7500 transmission electron microscope at an accelerating voltage of 75 kV.

Electron Diffraction. Electron diffraction patterns were acquired on Hitachi H-7500 transmission electron microscope. Data were acquired from **NSIII** nanosheets prepared as described above for TEM diffraction pattern acquisition. Adequate camera length were used to expose the small reciprocal lattice, and d-spacings were calculated using the equation: $d = \lambda L/R$, where R is the distance of the diffraction spots, λ denotes the electron wavelength, and L is the camera length. An aluminum polycrystalline standard from Ted Pella, Inc. (Redding, CA) was used to calibrate the camera length.

Atomic Force Microscopy. AFM measurements were performed using JEOL JSPM-4200 AFM instrument. Solutions of **NSIII** (4 mg/mL) in MOPS buffer (20 mM, pH 7.0) were diluted at 4 ℃ to a final concentration of 0.5 mg/mL and deposited on a freshly

cleaved mica substrate, then dried with nitrogen. Silicon AFM tips with a force constant (5.4-16 N/m) were used to image the specimens in tapping mode at a scan rate of 1 Hz. A TGZ-20 SiO_2 grating was employed for z-axis calibration (Ted Pella).

Small- and Wide-Angle X-ray Scattering Measurements. Synchrotron SAXS/WAXS measurements were performed at the 12-ID-B beamline of Advanced Photon Source at Argonne National Laboratory. A simultaneous SAXS/WAXS setup was utilized and the sample-to-detector distances were set such that the overall scattering momentum transfer, q, range was achieved from 0.005 to 2.4 $Å^{-1}$, where $q = 4\pi\sin\theta/\lambda$, 2θ denoting the scattering angle and λ the x-ray wavelength. The wavelength was set at 1.033 Å during the measurements. Scattered X ray intensities were measured using a Pilatus 2M (DECTRIS Ltd) detector for SAXS and Pilatus 300K for WAXS. SAXS/WAXS measurements were performed on aqueous solutions of peptide **NSIII** at a concentration of 4 mg/mL in MOPS buffer (20 mM, pH 7.0) at 4 ℃. A quartz capillary flow cell (1.5 mm diameter) was employed to prevent radiation damage. Twenty images were collected for each sample and buffer. The 2D scattering images were converted to 1D SAXS curves through azimuthally averaging after solid angle correction and then normalizing with the intensity of the transmitted x-ray beam, using the software package at beamline 12ID-B. The 1D curves of the samples were averaged and subtracted with the background measured from the corresponding buffers.

Detailed analysis of scattering data of SAXS/WAXS in terms of a 2D disc model (illustrated in figure 3.15): simulated SAXS profiles was calculated using a disc model with homogenous density. To simplify the simulations, the radius of disc was set to 3000 Å, comparable to the sheet surface dimensions measured by TEM. The disc height was set

to follow a normal Gaussian distribution centered at 107 Å with different standard deviations (σ). The curve with a value for σ equal to 13 Å has similar level of attenuation on the oscillations as the experimental data. Inset: expansion of the three diffraction peaks in the high q region.

Dynamic Light Scattering. Dynamic light scattering (DLS) measurements were performed at an angle of 90° from the incident beam on Malvern Zetasizer Nano instrument, equipped with a 4 mW, He-Ne laser with an emission wavelength at 633 nm. The Zetasizer software uses algorithms to extract the decay rates from the autocorrelation function of each sample to produce the size distribution of intensity. Solutions of **NSIII** (4 mg/mL) in MOPS buffer (20 mM, pH 7.0) were diluted at 4 ℃ to a final concentration of 2 mg/mL in the same buffer, and equilibrated at the appropriate temperature for 15 min prior to data acquisition. Melting experiments were performed in the temperature range from 4 ℃ to 60 ℃.

3.6 Reference

(1) Jiang, T.; Xu, C.; Liu, Y.; Liu, Z.; Wall, J. S.; Zuo, X.; Lian, T.; Salaita, K.; Ni, C.; Pochan, D.; Conticello, V. P. *J. Am. Chem. Soc.* **2014**, *136*, 4300-4308.

(2) Rele, S.; Song, Y. H.; Apkarian, R. P.; Qu, Z.; Conticello, V. P.; Chaikof, E. L. *J. Am. Chem. Soc.* **2007**, *129*, 14780-14787.

(3) O'Leary, L. E.; Fallas, J. A.; Bakota, E. L.; Kang, M. K.; Hartgerink, J. D. *Nat. Chem.* **2011**, *3*, 821-828.

(4) Umashankara, M.; Babu, I. R.; Ganesh, K. N. *Chem. Commun.* **2003**, 2606-2607.

(5) Babu, I. R.; Ganesh, K. N. *J. Am. Chem. Soc.* **2001**, *123*, 2079-2080.

(6) Erdmann, R. S.; Wennemers, H. *Angew. Chem., Int. Ed.* **2011**, *50*, 6835-6838.

(7) Govindaraju, T.; Avinash, M. B. *Nanoscale* **2012**, *4*, 6102-6117.

(8) Ariga, K.; Ji, Q.; Hill, J. P.; Bando, Y.; Aono, M. *NPG Asia Mater.* **2012**, *4*, e17.

(9) Bella, J.; Eaton, M.; Brodsky, B.; Berman, H. M. *Science* **1994**, *266*, 75-81.

(10) Berisio, R.; Vitagliano, L.; Mazzarella, L.; Zagari, A. *Protein Sci.* **2002**, *11*, 262-270.

(11) Vitagliano, L.; Berisio, R.; Mastrangelo, A.; Mazzarella, L.; Zagari, A. *Protein Sci.* **2001**, *10*, 2627-2632.

(12) Okuyama, K.; Hongo, C.; Fukushima, R.; Wu, G. G.; Narita, H.; Noguchi, K.; Tanaka, Y.; Nishino, N. *Biopolymers* **2004**, *76*, 367-377.

(13) Jiravanichanun, N.; Hongo, C.; Wu, G.; Noguchi, K.; Okuyama, K.; Nishino, N.; Silva, T. *ChemBioChem* **2005**, *6*, 1184-1187.

(14) Hongo, C.; Noguchi, K.; Okuyama, K.; Tanaka, Y.; Nishino, N. *J. Biochem.* **2005**, *138*, 135-144.

(15) Holmgren, S. K.; Taylor, K. M.; Bretscher, L. E.; Raines, R. T. *Nature* **1998**, *392*, 666-667.

(16) Holmgren, S. K.; Bretscher, L. E.; Taylor, K. M.; Raines, R. T. *Chem. Biol.* **1999**, *6*, 63-70.

(17) Bretscher, L. E.; Jenkins, C. L.; Taylor, K. M.; DeRider, M. L.; Raines, R. T. *J. Am. Chem. Soc.* **2001**, *123*, 777-778.

(18) Hodges, J. A.; Raines, R. T. *J. Am. Chem. Soc.* **2003**, *125*, 9262-9263.

(19) Shoulders, M. D.; Kotch, F. W.; Choudhary, A.; Guzei, I. A.; Raines, R. T. *J. Am. Chem. Soc.* **2010**, *132*, 10857-10865.

(20) Inouye, K.; Sakakibara, S.; Prockop, D. J. *Biochim. Biophys. Acta* **1976**, *420*, 133-141.

(21) Inouye, K.; Kobayashi, Y.; Kyogoku, Y.; Kishida, Y.; Sakakibara, S.; Prockop, D. J. *Arch. Biochem. Biophys.* **1982**, *219*, 198-203.

(22) Nishi, Y.; Uchiyama, S.; Doi, M.; Nishiuchi, Y.; Nakazawa, T.; Ohkubo, T.; Kobayashi, Y. *Biochemistry* **2005**, *44*, 6034-6042.

(23) Doi, M.; Nishi, Y.; Uchiyama, S.; Nishiuchi, Y.; Nishio, H.; Nakazawa, T.; Ohkubo, T.; Kobayashi, Y. *J. Pept. Sci.* **2005**, *11*, 609-616.

(24) Okuyama, K. *Connect. Tissue Res.* **2008**, *49*, 299-310.

(25) Okuyama, K.; Xu, X.; Iguchi, M.; Noguchi, K. *Biopolymers* **2006**, *84*, 181-191.

(26) Porod, G. *Small angle X-ray Scattering*; Academic Press: New York, 1982.

(27) Motooka, D.; Kawahara, K.; Nakamura, S.; Doi, M.; Nishi, Y.; Nishiuchi, Y.; Kang, Y. K.; Nakazawa, T.; Uchiyama, S.; Yoshida, T.; Ohkubo, T.; Kobayashi, Y. *Biopolymers* **2012**, *98*, 111-121.

(28) Okuyama, K.; Hongo, C.; Wu, G.; Mizuno, K.; Noguchi, K.; Ebisuzaki, S.; Tanaka, Y.; Nishino, N.; Bachinger, H. P. *Biopolymers* **2009**, *91*, 361-372.

(29) Okuyama, K.; Miyama, K.; Morimoto, T.; Masakiyo, K.; Mizuno, K.; Bachinger, H. P. *Biopolymers* **2011**, *95*, 628-640.

(30) Prockop, D. J.; Fertala, A. *J. Struct. Biol.* **1998**, *122*, 111-118.

(31) Papapostolou, D.; Smith, A. M.; Atkins, E. D.; Oliver, S. J.; Ryadnov, M. G.; Serpell, L. C.; Woolfson, D. N. *Proc. Natl. Acad. Sci. U. S. A.* **2007**, *104*, 10853-10858.

(32) Sharp, T. H.; Bruning, M.; Mantell, J.; Sessions, R. B.; Thomson, A. R.; Zaccai, N. R.; Brady, R. L.; Verkade, P.; Woolfson, D. N. *Proc. Natl. Acad. Sci. U. S. A.* **2012**, *109*, 13266-13271.

(33) Aggeli, A.; Nyrkova, I. A.; Bell, M.; Harding, R.; Carrick, L.; McLeish, T. C.; Semenov, A. N.; Boden, N. *Proc. Natl. Acad. Sci. U. S. A.* **2001**, *98*, 11857-11862.

(34) Gibaud, T.; Barry, E.; Zakhary, M. J.; Henglin, M.; Ward, A.; Yang, Y.; Berciu, C.; Oldenbourg, R.; Hagan, M. F.; Nicastro, D.; Meyer, R. B.; Dogic, Z. *Nature* **2012**, *481*, 348-351.

4 Rational design of multilayer collagen nanosheets with compositional and structural control

4.1 Introduction

The self-assembly of peptides,[1-10] proteins,[11,12] and architecturally related foldamers[13-16] has recently emerged as a method to create structurally defined and physically robust two-dimensional (2D) nano-scale assemblies (i.e., nanosheets). In several of these cases,[1,11,17], structural information derived from biophysical analysis of the nanosheets was employed to guide the design of functionalized assemblies in which the surfaces were modified selectively with exogenous substrates. This nanoarchitectonic approach [18,19] holds significant promise for the fabrication of functional nanosheet assemblies for technological applications. In order to develop these nanosheets as platforms for integration into more complex structures, uniform populations of structurally and dimensionally defined sheets would be the optimal starting point. Thus far, however, the composition of these nanosheets has been limited to homogeneous populations of protomers with little control over growth in the lateral (x/y) or vertical (z) directions. We report herein the design of protomers derived from collagen-mimetic peptides (CMPs) in which self-assembly can be directed selectively toward the formation of multilayer structures of defined composition and surface chemistry.

Recently we reported the fabrication of nanosheets from self-assembly of a series of collagen-mimetic peptides; **NSI**, **NSII**, and **NSIII**.[1,2] The sequences of these peptides comprised three consecutive blocks of positively charged, neutral, and negatively charged (Xaa-Yaa-Gly) triads arranged in order from the N-terminus to the C-terminus of the respective peptides. Structural analysis of the nanosheets was consistent with a model based on a tetragonal 2D lattice, in which structurally adjacent triple helices were packed in an anti-parallel arrangement. The long axes of the triple helices displayed a perpendicular orientation with respect to the sheet surface such that the length of the triple helix defined the thickness of a layer within the nanosheet. Coulombic interactions between the positively charged amino acids in the first block and the negatively charged residues of the third block ostensibly provided the thermodynamic driving force for nanosheet self-assembly. However, striking differences in self-assembly behavior were observed between the structurally related peptides within this series. The **NSI** and **NSII** nanosheets were highly polymorphic in the lateral (x/y) directions, with **NSI** nanosheets also displaying polymorphism in the vertical (z) direction. In contrast, the **NSIII** nanosheets were very uniform in lateral dimension and exclusively displayed single layer thickness.

The mechanism responsible for the differences in nanosheet morphology was difficult to deconvolute due to the absence of structural information on the assemblies at atomic level resolution. Moreover, the positively charged amino acids within this peptide series corresponded to either (4R)- or (4S)-4-aminoproline. The conformational behavior of these noncanonical imino acid derivatives within the structural context of the collagen triple helix has been shown to be a complex function of pH and sequence position.[20-22] In addition, the influence of these aminoproline derivatives on protein structure is only

beginning to be understood at the molecular level.[23-25] At this point in time, these considerations limit the utility of the peptides within the **NS** series as substrates for the development of a broadly applicable nano-scale structural platform.

4.2 Asymmetric peptides design

Previously, we reported the design of a collagen-mimetic peptide **CPII** (Figure 4.2), which self-assembled from aqueous solution into banded fibrils.[26] However, under appropriate conditions, **CPII** was also observed to form nanosheet structures similar to those derived from peptides within the **NS** series[1].(Figure 4.1) In contrast to the **NS** peptides, the sequence of **CPII** encompassed charged amino acid residues that occur frequently in native collagen isoforms.[27] In addition, the nature of electrostatic interactions between oppositely charged canonical amino acids within the collagen triple helix[28] are reasonably well understood from structural analyses of model peptide systems,[8,29-47] including those that self-assemble into structurally ordered materials.[26,48-51] On this basis, **CPII** peptide derivatives represent more attractive substrates for the controlled fabrication of nanosheet assemblies and may serve as a valuable test bed for examination of the influence of different architectural features on the self-assembly of the corresponding nanosheets.

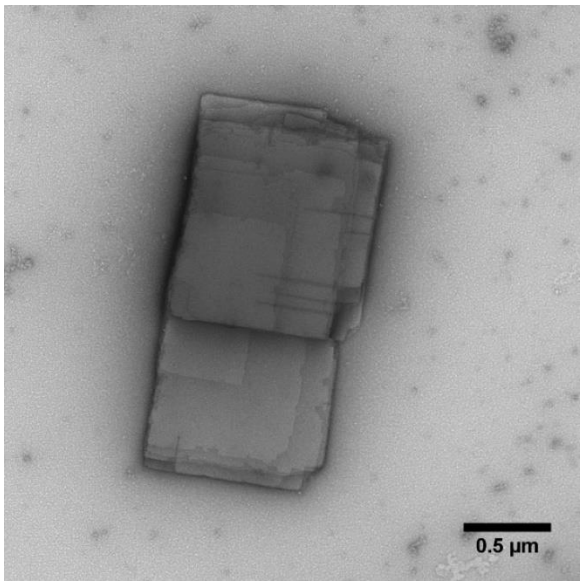

Figure 4.1 Negative stain TEM image of nanosheets observed from self-assembly of **CPII**.

The self-assembly of nanosheets based on collagen-mimetic peptides has been described in terms of a structural model in which the triple helix defines the layer thickness.[1,2] Structural analyses of the nanosheets have demonstrated that the peptide termini are displayed at the surface of the assembly.[1] In order to promote controlled growth in the z direction, we rationalized that collagen-mimetic peptides that encompassed an asymmetric distribution of charged blocks might localize the uncompensated charge on the surface of the nanosheet after self-assembly (Figure 4.2). Peptide-based nanosheets with surface charges could be employed as a strategy to manipulate the z-directional sheet stacking preferences in order to promote the formation of multilayer structures. This process is conceptually analogous to "layer-by-layer adsorption",[52] which employs electrostatic attraction as the primary driving force to build multi-component systems that comprise alternating layers of positively charged and negatively charged substrates.

However, simple charge complementation may not be sufficient to guarantee the formation of multilayer nanosheet assemblies that display a high degree of internal structural order. In order to address this concern, the charged residues were incorporated within the structural context of collagen triad repeats. The charged triple helical extensions should localize at the surface of the resultant nanosheets and present a preorganized template for assembly of nanosheets derived from peptides having complementary sequences of charged triads (Figure 4.2B). The surfaces of the nanosheets could be considered to resemble Lego plate assemblies at the supramolecular level, in that spatially defined patterns of studs and tubes occur at the interface between nanosheets due to the periodic arrangement of charged triple helical cohesive ends. The nascent layers should adopt the underlying 2D lattice structure of the nucleating nanosheet due to a template effect (Figure 4.2C).

In order to test this hypothesis, we designed and synthesized two peptides, **CP**$^{+}$ and **CP**$^{-}$, having asymmetric distributions of charged triad sequences (Figure 4.2A). The core sequence of each peptide is derived from **CPII** [26], but extensions corresponding to three positively charged triads or negatively charged triads were added to the N-terminus of **CP**$^{+}$ or C-terminus of **CP**$^{-}$, respectively. These three extra triads should protrude from the surface of the nanosheet after self-assembly of the respective peptides. The identity of the positively charged triads (Pro-Arg-Gly) and negatively charged triads (Glu-Hyp-Gly) reflect positional preferences that were previously determined from host-guest studies of collagen-mimetic peptides.[53-55]

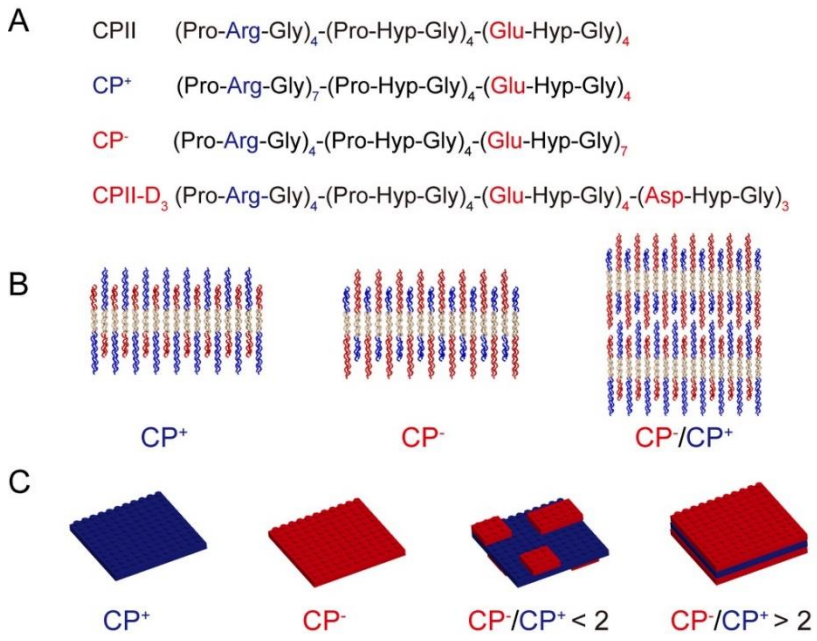

Figure 4.2 (A) Sequences of asymmetric peptides. (B) Side view of the antiparallel packing of triple helices within individual layers and a stacked bilayer. Individual lines represent triple helices with different charged blocks. (C) Three-dimensional representations of charged nanosheet assemblies from **CP**$^{+}$ and **CP**$^{-}$ peptides, and multilayer structures at different **CP**$^{-}$/**CP**$^{+}$ mixing ratios. Color code for amino acid residues, helices, and surfaces: red, negatively charged; neutral, uncharged; blue: positively charged.

4.3 Results and discussion

4.3.1 Circular dichroism

Circular dichroism (CD) spectropolarimetry was employed to assess the conformational properties of the **CP**$^{+}$ and **CP**$^{-}$ peptides in buffered aqueous solution, as well as the thermal stabilities of the resultant triple helices (Figure 4.3 and 4.4). **CP**$^{+}$ and **CP**$^{-}$ peptides (1 mg/mL) in MES buffer (20 mM, pH 6.0) displayed the classic CD signature of a collagen-like triple helix, with a maximum absorption from 222 to 224 nm

and a minimum absorption from 195 to 199 nm. The melting transition (T_m) of peptide **CP**$^+$ (76 ℃) was observed to be significantly higher than the corresponding transition for **CP**$^-$ (56 ℃). Notably, the T_m values for triple helices derived from either the **CP**$^+$ peptide or the **CP**$^-$ peptide were greater than the corresponding T_m value of 44 ℃ for the parent **CPII** system [26] under identical conditions (Figure 4.5).

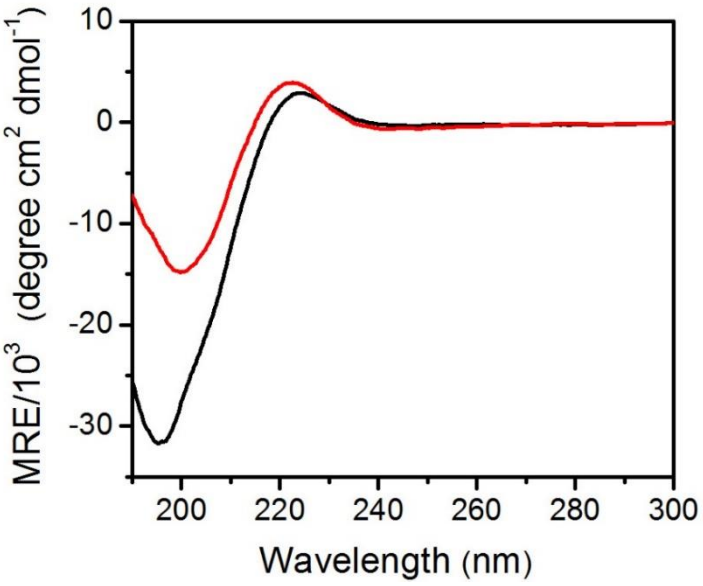

Figure 4.3 CD spectra of aqueous solutions of the peptide **CP**$^+$ (red), and **CP**$^-$ (black).

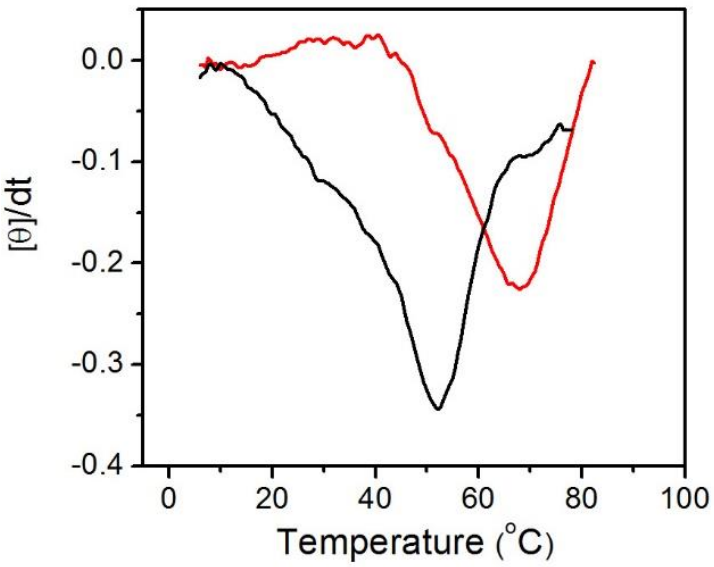

Figure 4.4 First derivative of the CD melting curve derived from monitoring the maximal signal as a function of temperature for aqueous solutions of **CP**$^{+}$ (red), and **CP**$^{-}$ (black).

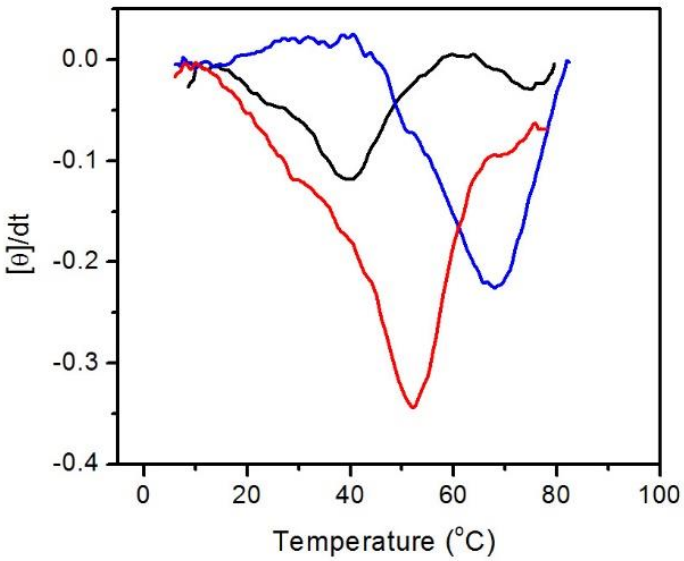

Figure 4.5 First derivative of the CD melting curve derived from monitoring the maximal signal as a function of temperature for aqueous solutions of **CP**$^{+}$ (blue), **CP**$^{-}$ (red), and **CPII** (black).

The trend in CD data can be understood in terms of the relative influence of the respective triads on the thermodynamic stability of triple helices derived from collagen-mimetic peptides.[53-55] The (Pro-Arg-Gly) triad was observed to be similar in stability to the canonical (Pro-Hyp-Gly) triad in host-guest model peptide systems.[56] The stabilizing effect of arginine at the Yaa position has been attributed to its potential for the formation of intramolecular or intermolecular hydrogen bonding interactions in the structural context of a collagen triple helix.[57] In contrast, the (Glu-Hyp-Gly) triad, despite having the greatest stability among (Xaa-Hyp-Gly) guest triads, was nonetheless destabilizing vis-à-vis the canonical (Pro-Hyp-Gly) triad sequence. These observed T_m values for triple helices of **CP**$^+$ versus **CP**$^-$ can be attributed to the presence of a greater number of stabilizing (Pro-Arg-Gly) triads in the former peptide in comparison to the presence of destabilizing (Glu-Hyp-Gly) triads in the latter case.

4.3.2 Transmission Electron Microscopy

Transmission electron microscopy (TEM) was employed to investigate the morphology of species derived from self-assembly of the **CP**$^+$ and **CP**$^-$ peptides (Figure 4.6 and 4.7). Peptide **CP**$^+$ underwent self-assembly into nanosheets structures in MES buffer (20 mM, pH 6.0) over a period of hours, even at concentrations as low as 0.2 mg/mL. (Figure 4.6) In contrast, peptide **CP**$^-$ formed detectable nanosheets only over a period of months at a concentration of $\geq$ 5 mg/mL in MES buffer (20 mM, pH 6.0). The addition of calcium(II) ion (4 mM) was observed to accelerate the self-assembly of the **CP**$^-$ nanosheets (5 mg/mL), effectively lowering the association time from months to hours. (Figure 4.7) Calcium(II) ion can coordinate to glutamate residues within proteins,[58] often displaying K_d values in the μM to mM range within calcium binding proteins.[59] Coordination of

calcium ion may stabilize the **CP**$^{-}$ assemblies through partial neutralization of the excess negative charge of the glutamate side chains within the $(Glu\text{-}Hyp\text{-}Gly)_3$ extensions. However, a comparison of the CD melting curves for **CP**$^{-}$ in the presence or absence of calcium(II) ion indicated an insignificant difference in T_m between the two samples (Figure 4.8). These results suggest that the calcium ions probably promote self-assembly through coordination of glutamate residues on proximal triple helices within a nanosheet rather than stabilization of the triple helical conformation.

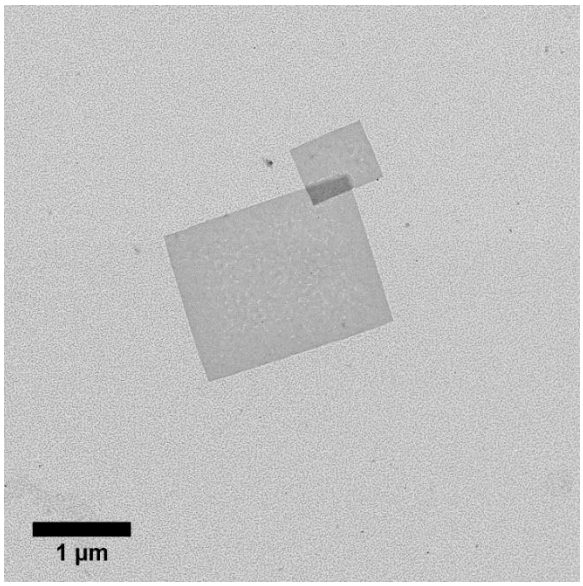

Figure 4.6 Negative stain TEM image of nanosheets observed from self-assembly of the peptide **CP**$^{+}$.

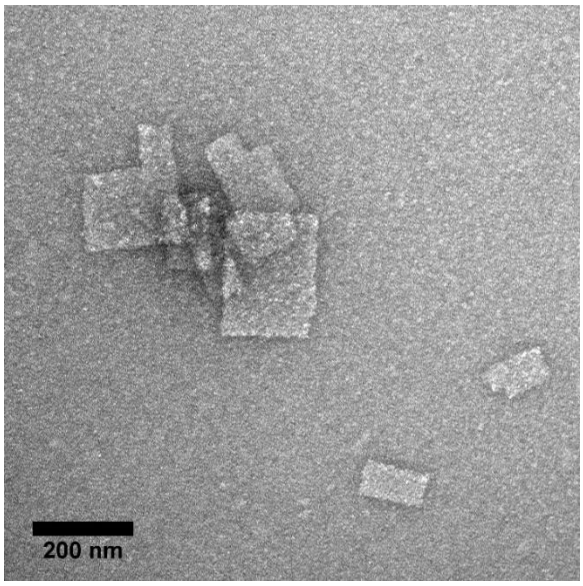

Figure 4.7 Negative stain TEM image of nanosheets observed from self-assembly of the peptide **CP**$^{-}$ with Ca^{2+}.

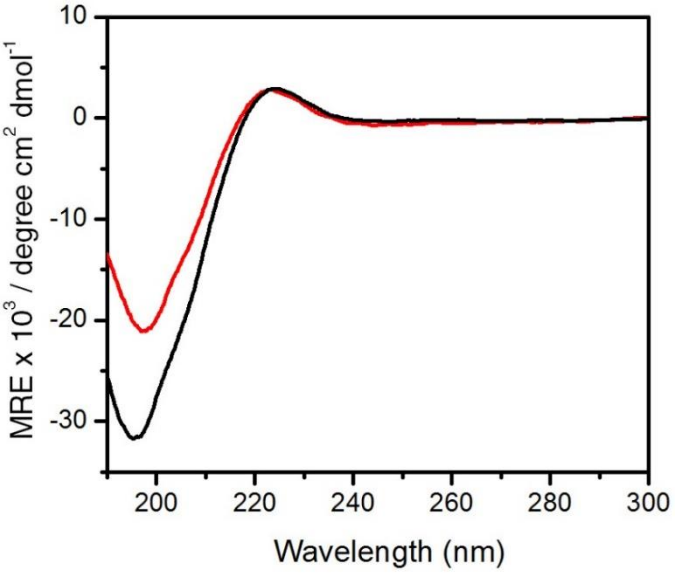

Figure 4.8 CD spectra of aqueous solutions of the peptide **CP**$^{-}$ in the presence (red) and absence (black) of Ca^{2+}.

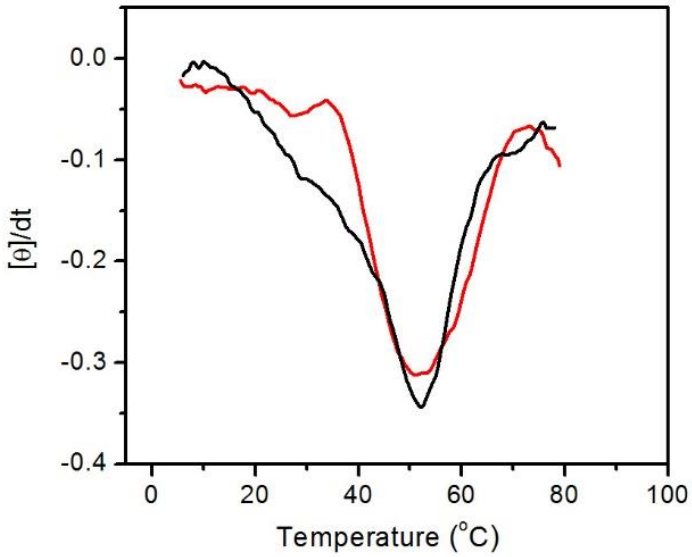

Figure 4.9 First derivative of the CD melting curve derived from monitoring the maximal signal as a function of temperature for aqueous solutions of peptide **CP**$^{-}$ in the presence (red) and absence (black) of Ca^{2+}.

However, the slow self-assembly of the **CP**$^{-}$ nanosheets in the absence of calcium(II) ion cannot be solely attributed to the negative charge associated with the three extra (Glu-Hyp-Gly) triads. A variant peptide, **CP**$^{-}$**D**$_3$, in which the three C-terminal triads were replaced with (Asp-Hyp-Gly), could self-assemble into nanosheets within hours in the absence of calcium ion (Figure 4.10). Notably, CD spectropolarimetry of the **CP**$^{-}$**D**$_3$ assemblies indicated a melting transition of circa 60 ℃, which is significantly greater than that of the parent peptide **CP**$^{-}$ (Figures 4.11 and 4.12). Thus, the (Asp-Hyp-Gly)$_3$ extensions can stabilize the triple helix, and promote nanosheet assembly, despite a weaker propensity for triple helix formation from model studies on host-guest peptides.[53-55] The difference in thermodynamic stability and kinetics of self-association between **CP**$^{-}$ and

CP$^-$D$_3$ cannot be fully attributed to the small difference in pK_a between the Asp and Glu side chains ($\Delta pK_a \approx 0.2$) of the free amino acids. However, Asp residues have been observed to form hydrogen-bonded interactions with each other in the crystal structure of a collagen triple helix derived from a model peptide, which may provide a rationale for the observed differences in nanosheet formation between **CP$^-$** and **CP$^-$D$_3$**.[60]

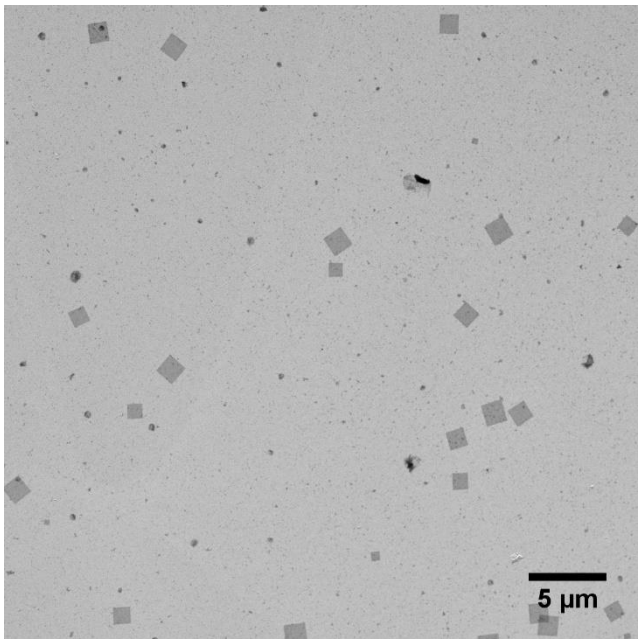

Figure 4.10 Negative stain TEM image of nanosheets observed from self-assembly of the peptide **CP$^-$D$_3$**.

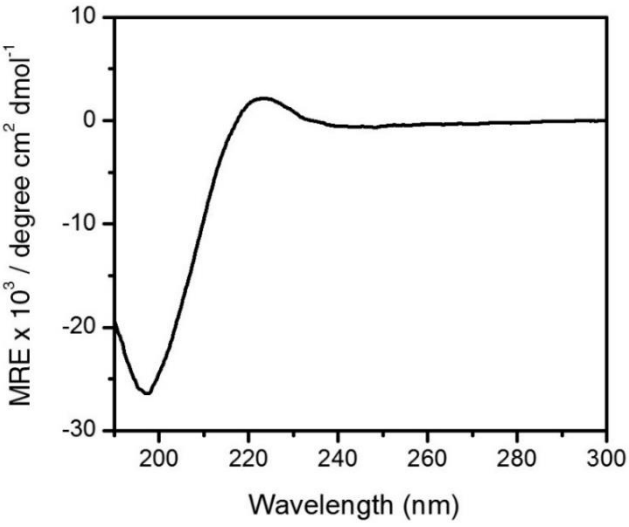

Figure 4.11 CD spectra of an aqueous solution of the peptide **CP$^-$D$_3$**.

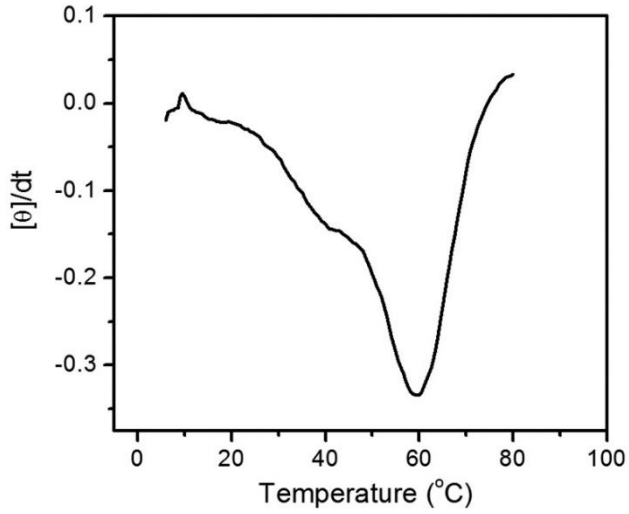

Figure 4.12 First derivative of the CD melting curve derived from monitoring the maximal signal as a function of temperature for an aqueous solution of the peptide **CP$^-$D$_3$**.

4.3.3 Atomic force microscopy

A tapping mode atomic force microscope (AFM) was employed to estimate the thickness of nanosheets derived from self-assembly of the **CP**$^{+}$ and the **CP**$^{-}$ peptides in MES buffer (Figure 4.13 and 4.14). The **CP**$^{-}$ nanosheets (5 mg/mL) were assembled in the presence of calcium(II) ion (4 mM). Statistical analysis of the AFM height measurements (Figure 4.15) indicated an average thickness of 9.4 $\pm$ 1.0 nm for the **CP**$^{+}$ nanosheets, and 9.9 $\pm$ 1.2 nm for the **CP**$^{-}$ nanosheets, respectively. The theoretical monolayer thicknesses were calculated to be 10.3 nm for the structured core of a 2D layer derived from the **CPII** peptide sequence (36 residues x 0.286 nm rise/residue for collagen triple helices).[1] The calculated thickness of the structured core is within experimental error of the measured thicknesses for the respective nanosheet assemblies. The close correspondence of the values suggests that the triads extending from either surface of the assembly might be unstructured under the dry conditions employed for AFM measurements.

Due to the anti-parallel arrangement of adjacent triple helices within the structure (vide infra), the extensions of the asymmetric charged blocks from anti-parallel triple helices should protrude from opposite surfaces of the nanosheet (Figure 4.2). Consequently, in the absence of charge compensation from an oppositely charged triple helix, the extensions may be destabilized due to charge repulsion between similarly charged amino acid residues.

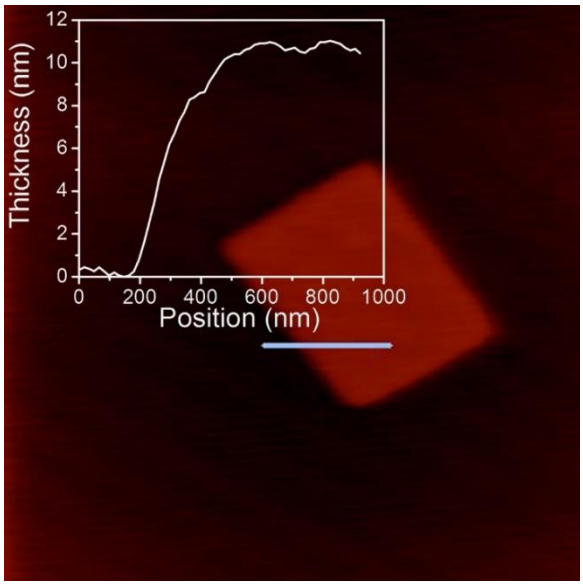

Figure 4.13 AFM image and height profile (insert) of a single-layer nanosheet of **CP**$^{+}$.

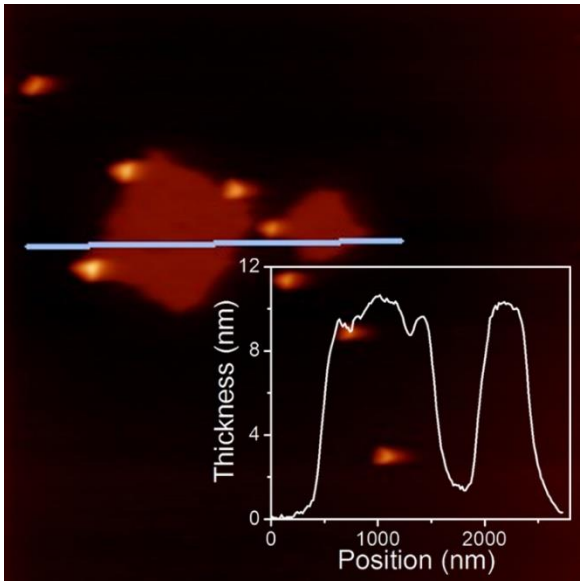

Figure 4.14 AFM image and height profile (insert) of a single-layer nanosheet of **CP**$^{-}$ with Ca^{2+}.

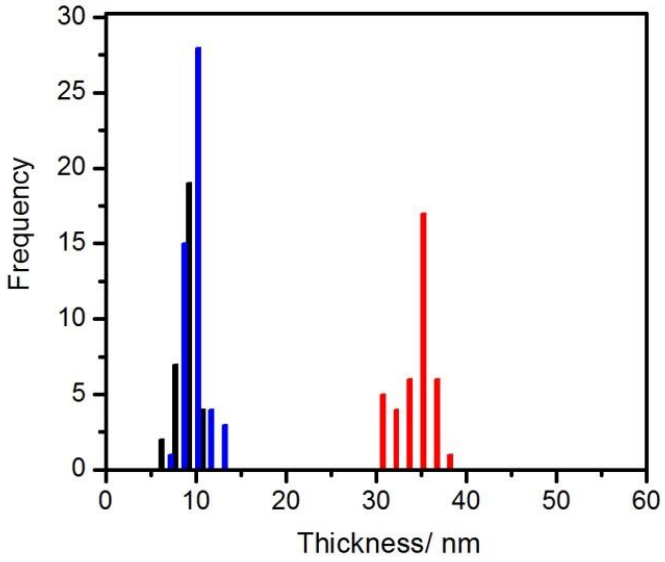

Figure 4.15 Statistical analysis of AFM height measurements for **CP**$^{+}$ nanosheets (black), **CP**$^{-}$ nanosheets with Ca^{2+} (blue), and **CP**$^{+}$/**CP**$^{-}$ multilayer nanosheets at a concentration ratio of 1:2 (red).

4.3.4 Triple layer formation

If indeed these extensions are accessible at the surface of the assemblies, they should be available to interact with oppositely charged triple helices, and nucleate the formation of charge complementary layers on the exposed surfaces of the original nanosheet. Since the **CP**$^{+}$ peptide assembled readily from buffered aqueous solution, the corresponding nanosheets were employed as a substrate to template the growth of nanosheets derived from the **CP**$^{-}$ peptide. The morphologies of resultant structures depended on the initial concentration ratio of unassembled **CP**$^{-}$ peptide with respect to the concentration of the **CP**$^{+}$ peptide in the preformed nanosheets. At concentration ratios of less than 2:1 (**CP**$^{-}$:**CP**$^{+}$), layered structures were observed that appeared as small sheets

located on the surface of larger pre-assembled **CP$^+$** nanosheets (Figure 4.16). At a concentration ratio of **CP$^-$**:**CP$^+$** of 2:1, the nascent nanosheets on the surface of the basal nanosheet were observed to fuse into a single continuous layer that extended over the entire surface of the original nanosheet (Figure 4.17). This controlled growth of nanosheets in the z direction contrasts with the uncontrolled sheet stacking observed for the parent peptide **CPII** (Figure 4.1). These results suggest that the presence of the charged overhangs prevents association between similarly charged nanosheets, as expected on the basis of electrostatic considerations.

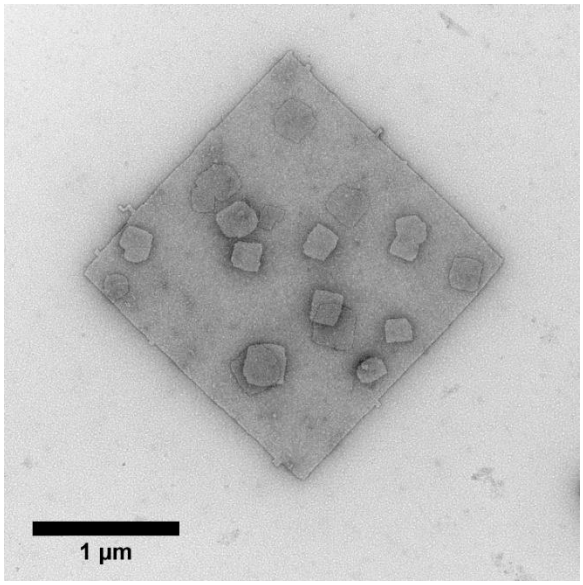

Figure 4.16 Representative negative stain TEM image of a **CP$^-$**/**CP$^+$**/**CP$^-$** assembly from incubation of preformed **CP$^+$** nanosheets with free **CP$^-$** peptide at a **CP$^-$**:**CP$^+$** concentration ratio of 1:5.

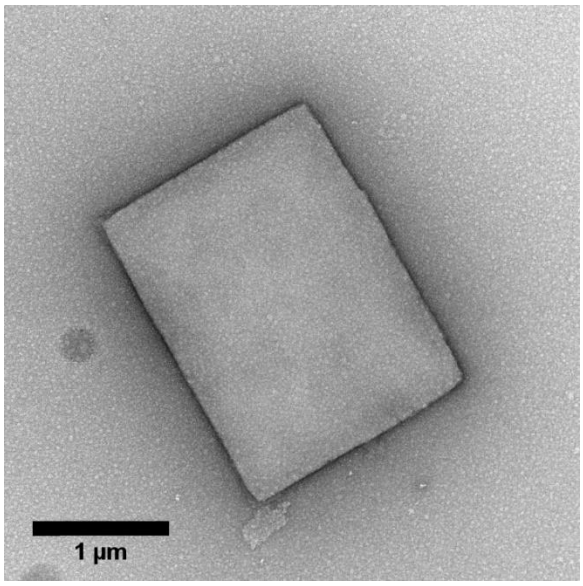

Figure 4.17 Representative negative stain TEM image of a mature **CP**$^{-}$/**CP**$^{+}$/**CP**$^{-}$ assembly from incubation of preformed **CP**$^{+}$ nanosheets with free **CP**$^{-}$ peptide at a **CP**$^{-}$:**CP**$^{+}$ concentration ratio of 2:1.

AFM height measurements of the partially formed nanosheets, assembled at lower **CP**$^{-}$:**CP**$^{+}$ concentration ratios (Figure 4.18), indicated that both the nascent layers and the original nanosheet had thickness values of circa 10 nm, which correlated well with the previously observed height values for the individual monolayer nanosheets. AFM height measurements on the mature nanosheets indicated an average height of 34 ±2.0 nm (Figure 4.19). These height measurements were in agreement with a calculated thickness of 36 nm for a theoretical model consisting of a triple-layer nanosheet (3 x 10.3 nm core layers with 2 structured intersheet regions of 9 residues x 0.286 nm rise/residue). This model for sheet growth is consistent with the proposed anti-parallel orientation of adjacent triple helices within the collagen-based nanosheets,[1,2] which necessitates that the two surfaces are identical and, therefore, equally competent to promote the growth of new layers. Notably,

each of the individual peptides can only support the growth of single-layer nanosheets in isolation, which is presumably a consequence of the high charge density at the surface of the individual nanosheets. Full surface coverage is only observed under conditions in which the concentration ratio of **CP**$^{-}$:**CP**$^{+}$ is $\geq$ 2:1, which would be a pre-requisite for the formation of a triple-layer structure with full surface coverage.

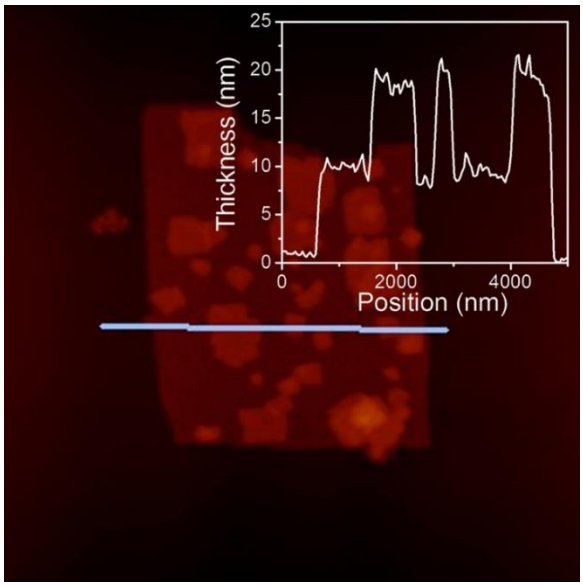

Figure 4.18 Representative AFM image and height profile (insert) of a **CP**$^{-}$/**CP**$^{+}$/**CP**$^{-}$ assembly from incubation of preformed **CP**$^{+}$ nanosheets with free **CP**$^{-}$ peptide at a **CP**$^{-}$:**CP**$^{+}$ concentration ratio of 1:5.

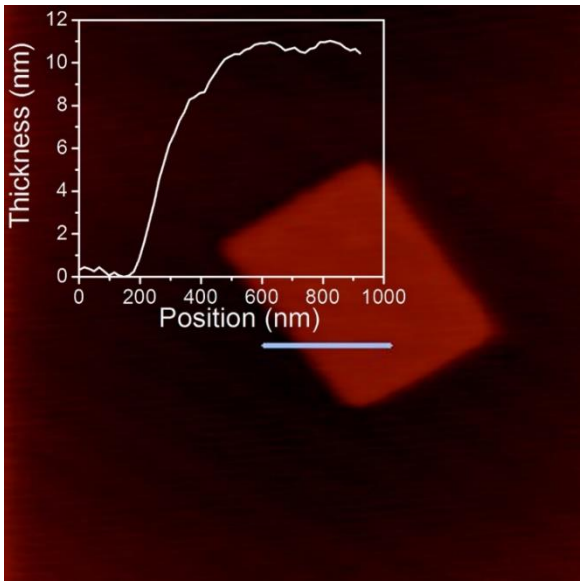

Figure 4.19 Representative AFM image and height profile of a mature **CP**$^{-}$/**CP**$^{+}$/**CP**$^{-}$ assembly form incubation of preformed **CP**$^{+}$ nanosheets with free **CP**$^{–}$ peptide at a **CP**$^{–}$:**CP**$^{+}$ concentration ratio of 2:1.

An important consequence of this proposed mechanism is that the surface charge of the triple-layer structure should be opposite to that of the original nanosheet structure. The preformed **CP**$^{+}$ nanosheet should display a positive surface charge due to the presence of the N-terminal (Pro-Arg-Gly)$_3$ extensions. Since the growth of the triple-layer structure involves lamination with the oppositely charged **CP**$^{–}$ peptide, the corresponding nanosheets should display a negative surface charge due to the presence of the C-terminal (Glu-Hyp-Gly)$_3$ extensions.

4.3.5 Zeta potential measurements

Zeta potentials were determined for individual nanosheets as well as the mature triple-layered nanosheets. The zeta potential of the **CP**$^{+}$ nanosheets (0.1 mg/mL) was measured to be circa +20 mV, and **CP**$^{–}$ sheets (0.1 mg/mL, 0.08 mM Ca^{2+}) was circa -19

mV. As a control, **CP$^-$D$_3$** nanosheets had an observed zeta potential of circa -26 mV (Figure 4.20). These results are in agreement with the assumption that the arginine containing extensions confer a positive surface charge to the **CP$^+$** nanosheets, whereas the glutamate or aspartate extensions provide negative surface charges to **CP$^-$** and **CP$^-$D$_3$** nanosheets. When adding the unassembled **CP$^-$** peptide to pre-formed **CP$^+$** nanosheets in the ratio of 2:1, the zeta potentials of the resultant structures decreased to negative values within hours and stabilized to circa -23 mV after one week of incubation (Figure 4.21). For mixtures of the **CP$^-$**/**CP$^+$** peptides at different concentration ratios, the zeta potentials of the corresponding structures decreased as the concentration ratio of the peptides increased until it reached the limiting value of 2:1 (Figure 4.22). The zeta potential measurements strongly support a triple-layered model in which growth of negatively charged layers occurs on the top and bottom surfaces of the original positively charged nanosheet.

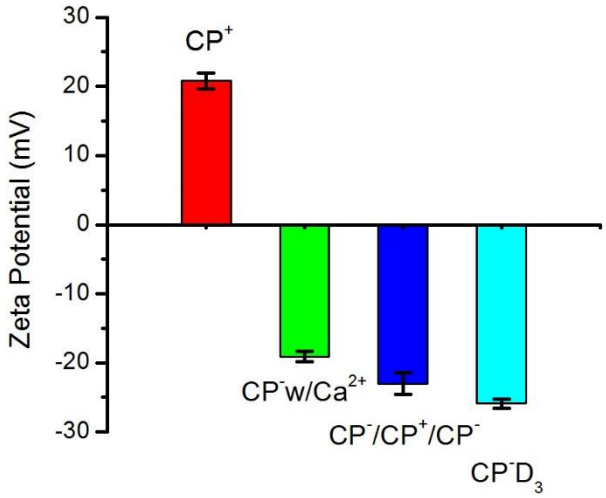

Figure 4.20 Zeta potential measurements of aqueous solutions of **CP$^+$** nanosheets, **CP$^-$** nanosheets with Ca^{2+}, mature **CP$^-$**/**CP$^+$**/**CP$^-$**nanosheets, and **CP$^-$D$_3$** nanosheets.

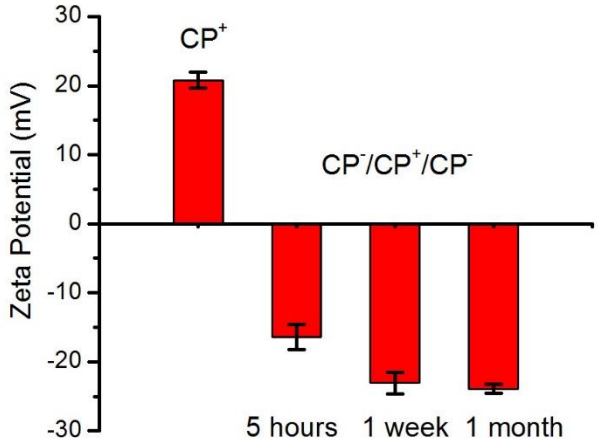

Figure 4.21 Time dependence of the zeta potential for assemblies derived from incubation of pre-formed **CP**$^{+}$ nanosheets with free **CP**$^{-}$ peptide at a **CP**$^{-}$:**CP**$^{+}$ concentration ratio of 2:1.

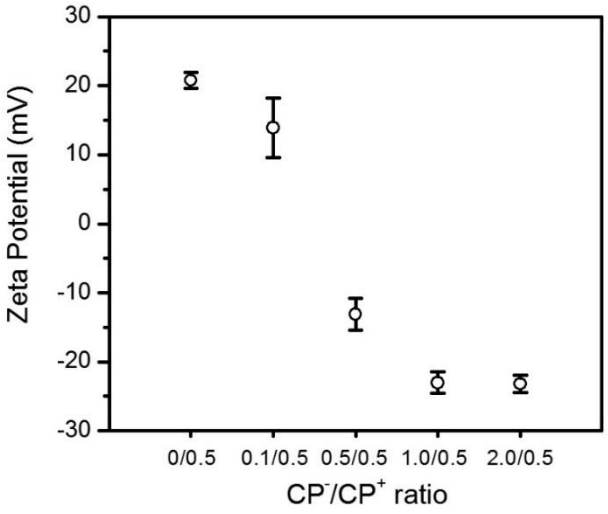

Figure 4.22 Concentration dependence of the zeta potential for assemblies derived from incubation of pre-formed **CP**$^{+}$ nanosheets with free **CP**$^{-}$ peptide at different **CP**$^{-}$:**CP**$^{+}$ concentration ratio.

4.3.6 Gold nanoparticle binding assay

In order to correlate surface charge with nanosheet topology, two complementary methods were investigated. In the first case, gold nanoparticles with charged surface layers were employed as probes to distinguish among the nanosheets on the basis of differential adsorption. These measurements were predicated on the assumption that the excess charged residues on the surfaces of the nanosheets would to be accessible for interaction with oppositely charged gold nanoparticles.[1] Unstained sheets were probed with either cationic gold nanoparticles (10 nm core functionalized with (11-mercaptoundecyl)-N, N, N-trimethylammonium bromide) or anionic gold nanoparticles (9 nm core labeled with mercaptopoly-(ethylene glycol)-carboxylic acid). The resultant TEM images indicated that the anionic gold nanoparticles preferentially stained the positively charged $\mathbf{CP^+}$ nanosheets, which confirmed that these nanosheets displayed a positive surface charge (Figure 4.23). In contrast, the cationic gold nanoparticles preferentially adsorbed to the surface of the $\mathbf{CP^-}$ and $\mathbf{CP^-D_3}$ nanosheets, which confirmed the presence of a negatively charged surface layer (Figure 4.24 and 4.25). The anionic gold nanoparticles were observed to surround the $\mathbf{CP^-}$ nanosheets, probably due to association of excess calcium(II) ions around edges of sheets. The surfaces of the triple-layered nanosheet were densely stained with the cationic gold nanoparticles while being essentially devoid of anionic gold nanoparticles under identical conditions (Figure 4.27). The incompletely layered structures (concentration ratio of $\mathbf{CP^-}/\mathbf{CP^+} < 2$) were observed to interact with both cationic and anionic gold nanoparticles. These results implied the presence of both positively and negatively charged domains on the surface of the nanosheets. However, TEM imaging of

the nanosheets resulting from these the gold nanoparticle binding assays could not generate sufficient contrast to resolve the presence of distinct domains in x-y direction.

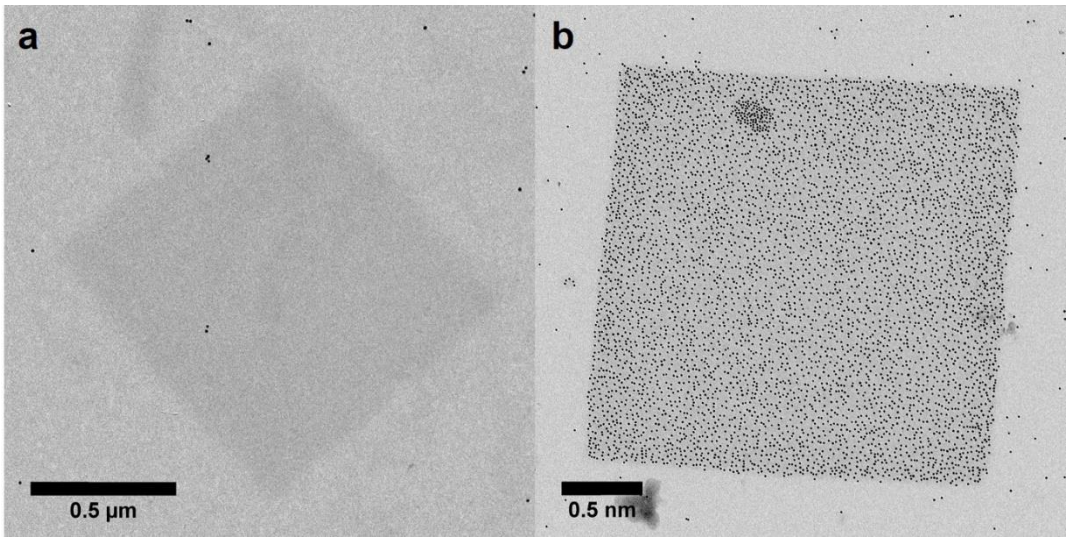

Figure 4.23 TEM images of an unstained nanosheet of **CP**$^{+}$ probed with (A) cationic and (B) anionic gold nanoparticles.

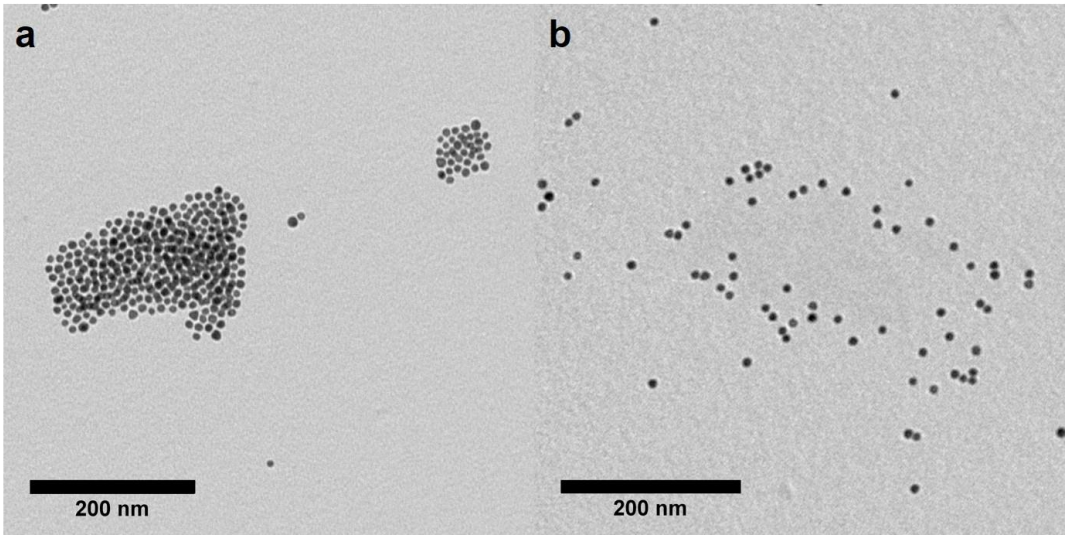

Figure 4.24 TEM images of unstained nanosheets of **CP**$^{-}$ nanosheets with Ca^{2+} probed with (A) cationic and (B) anionic gold nanoparticles.

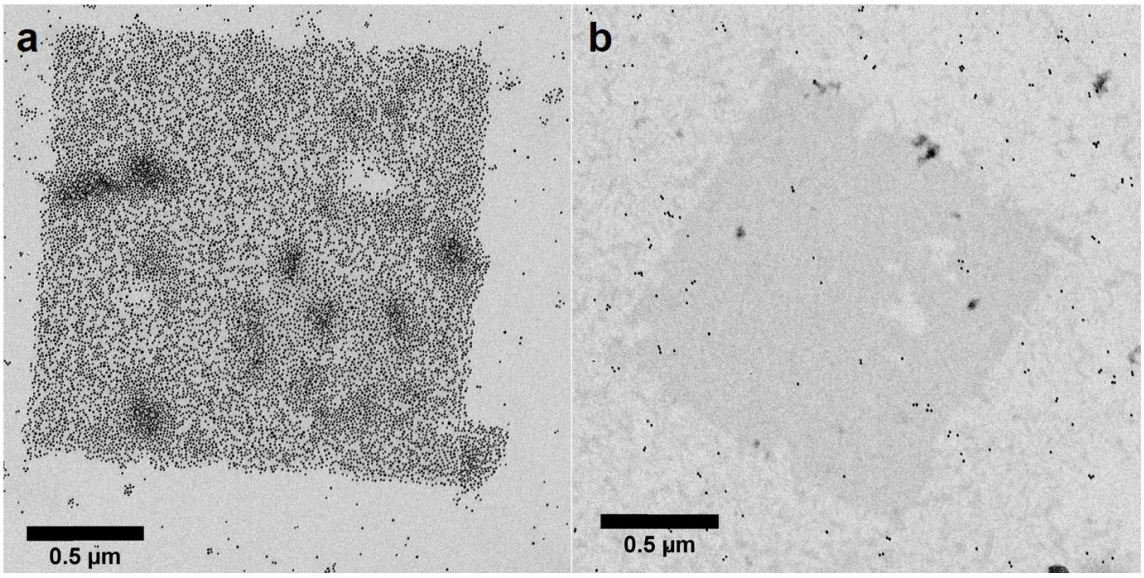

Figure 4.25 TEM images of an unstained peptide nanosheet of **CP$^-$D$_3$** probed with (A) cationic and (B) anionic gold nanoparticles.

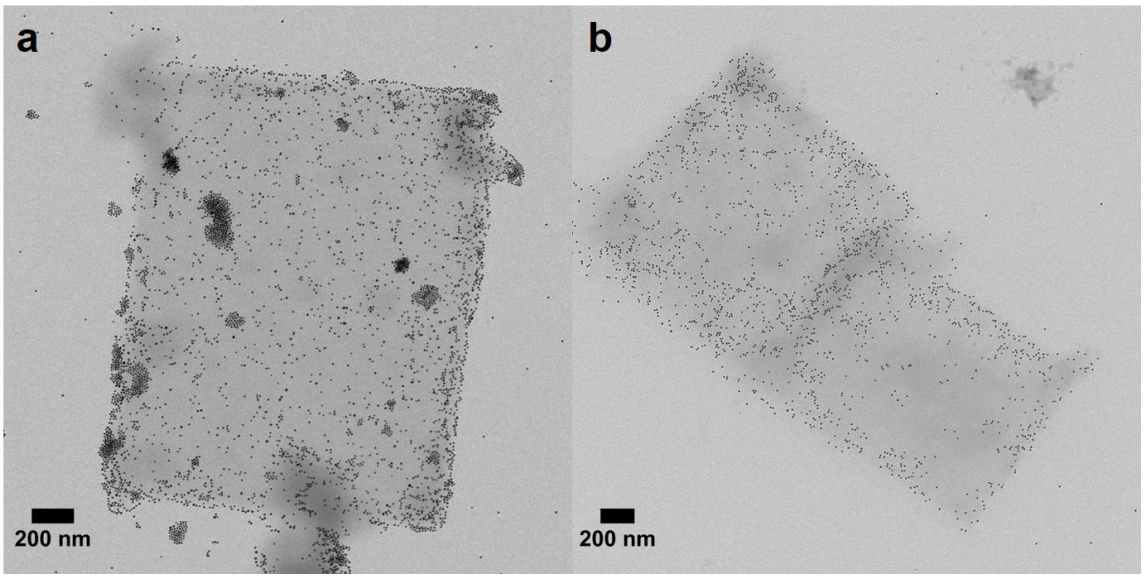

Figure 4.26 TEM images of unstained peptide nanosheets probed with (A) cationic and (B) anionic gold nanoparticles from **CP$^-$**/**CP$^+$**/**CP$^-$** assemblies at a **CP$^-$**:**CP$^+$** concentration ratio of 1:1.

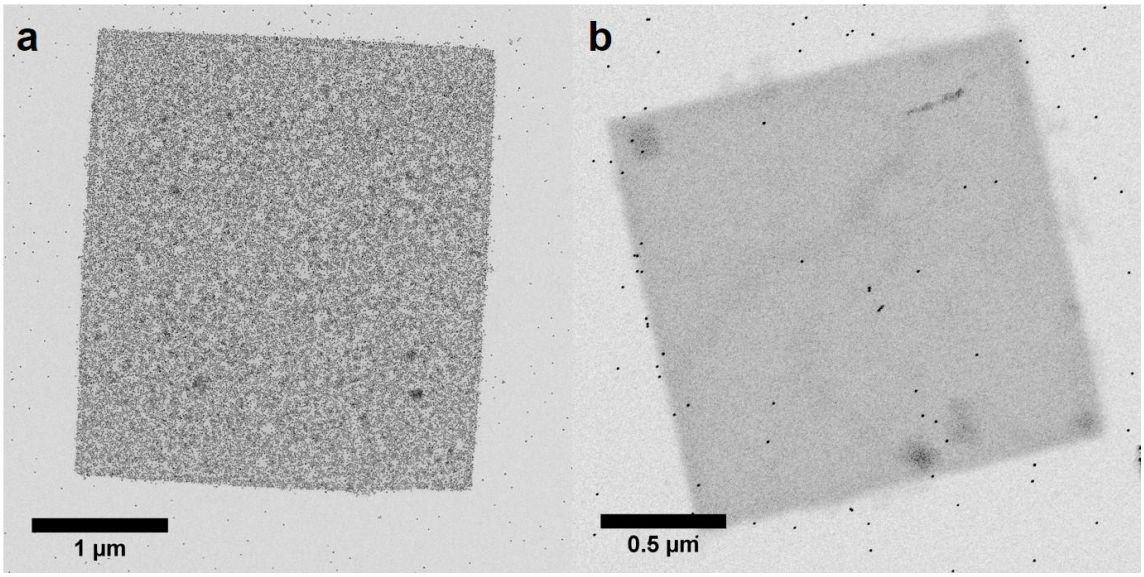

Figure 4.27 TEM images of an unstained triple-layer sheet of **CP$^-$/CP$^+$/CP$^-$** probed with (A) cationic and (B) anionic gold nanoparticles.

4.3.7 Electrostatic force microscopy

The surface charge distributions of the nanosheets were also mapped using ambient electrostatic force microscopy (EFM). EFM images the surface charge distribution that a conductive tip experiences due to electrostatic interactions with a charged substrate. Different charge states on a substrate can be distinguished on the basis of the potential difference with respect to the bias on the tip. This method has been employed in lifted mode to map surface charge within protein [61-64] and peptide [65-68] assemblies based on variation of the phase and amplitude response of an AC signal to the surface from the conductive tip. Using a positive scanning tip bias, oppositely charged substrates appear as dark images on lighter background in EFM amplitude mode and as light images on a darker background in EFM phase mode. For situations in which the interactions between the tip

and substrate are electrostatically repulsive, an opposite pattern of signal contrast is observed for the different EFM imaging modes.

EFM scans of **CP**$^{+}$ nanosheets indicated a repulsive signal in EFM amplitude and phase (Figure 4.28A), as would be expected for a positively charged substrate interacting with a positively biased tip. In contrast, the EFM images of nanosheets derived from either **CP**$^{-}$ or **CP**$^{-}$**D**$_{3}$ displayed an inverse pattern with respect to that of the **CP**$^{+}$ nanosheets, which is consistent with an electrostatically attractive interaction between the tip and substrate (Figure 4.28B and D). The EFM analysis of the triple-layered nanosheets recapitulated the behavior of the negatively charged nanosheets of **CP**$^{-}$ or **CP**$^{-}$**D**$_{3}$ (Figure 4.28C). Moreover, the EFM signal response of the multilayer sheets was much stronger than any of the single-layer nanosheets, irrespective of the surface charged state. This signal enhancement may be attributed to the thermal stability and greater physical robustness of the multilayered nanosheets. The combined data from EFM image analysis, zeta potential measurements, and charged nanoparticle binding assays are in substantial agreement with a negative surface charge state for the multilayer nanosheets. These observations fully support a mechanism in which the positively charged **CP**$^{+}$ nanosheets template the assembly of the **CP**$^{-}$ nanosheets at both exposed surfaces, which results in a triple-layer nanosheet having a compositional distribution of (**CP**$^{-}$/**CP**$^{+}$/**CP**$^{-}$) along the z direction of the assembly.

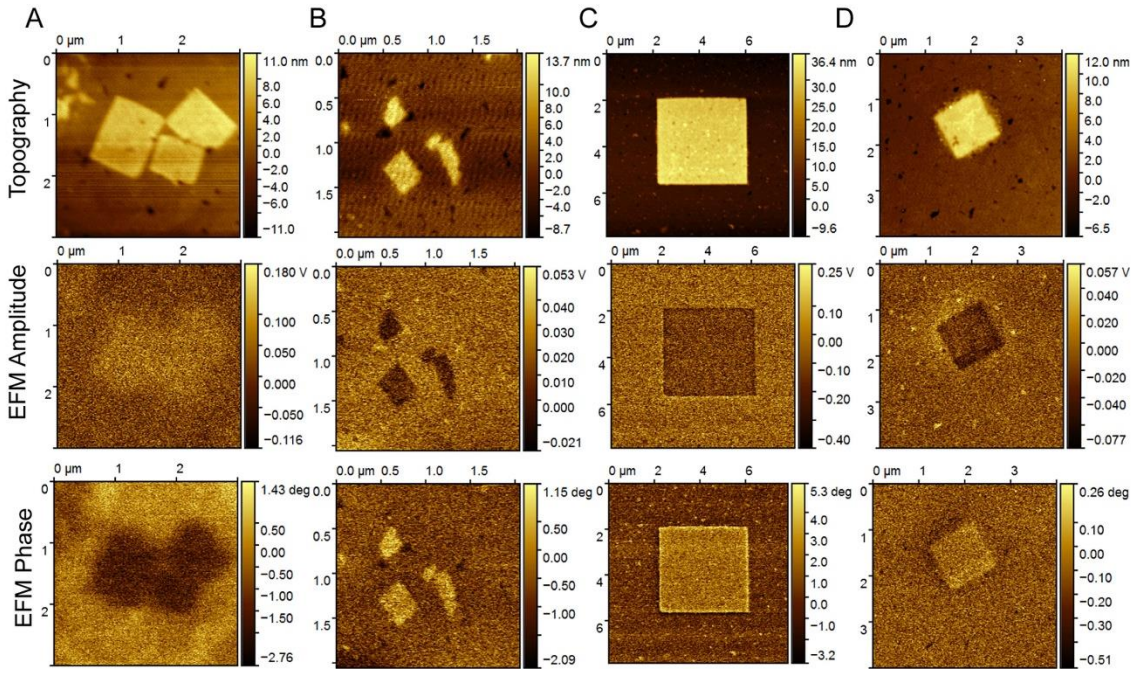

Figure 4.28 AFM topographic (upper row), EFM amplitude (middle row), and EFM phase (lower row) images of nanosheet specimens: (A) **CP**$^{+}$ nanosheets; (B) **CP**$^{-}$ nanosheets with Ca^{2+}; (C) triple-layer **(CP**$^{-}$**/CP**$^{+}$**/CP**$^{-}$**)** nanosheets; (D) **CP**$^{-}$**D**$_3$ nanosheets.

4.3.8 Solution X-ray scattering measurement

Synchrotron SAXS/WAXS measurements provided further evidence of the formation of a triple-layer structure in solution (Figure 4.29). Scattering profiles in the Guinier region could be fit to a model for sheet-like forms.[69] The Guinier fit for the **CP**$^{+}$ nanosheet sample afforded a value of 13.3 nm for the average sheet thickness (Figure 4.29). The sheet-like structure is also reflected in the oscillating feature in scattering curve (q up to 0.3 $Å^{-1}$). However, the oscillation was greatly attenuated and damped due to thickness variation. This thickness variation was estimated as ±3.0 nm through computer simulations (Figure 4.30).[2] The thickness calculated from SAXS measurements in solution is greater than the corresponding thickness value of 9.4 nm from AFM height measurements.

The discrepancy between these measurements presumably reflects the difference in the conformation of the charged triad extensions in solution versus the solid state. The sheet thickness from AFM measurements closely corresponds to the theoretical thickness for the structured core derived from the **CPII** peptide sequence.[1,2,26] Presumably, the three N-terminal (Pro-Arg-Gly) triads are unstructured and collapsed on the surface of the nanosheets under dry conditions, and therefore contribute little to the measured height. In solution, the N-terminal $(Pro\text{-}Arg\text{-}Gly)_3$ sequence presumably extends from surface of the nanosheet in order to promote solvation of the charged amino acid residues. A theoretical limit can be placed on the thickness of the surface layer, which can be correlated with the length of the charged triad extensions in a triple helical conformation. The core thickness of the nanosheet should be circa 10.3 nm, while the fully extended triads can contribute up to 2.6 nm to each side of the nanosheet (9 residues x 0.286 nm rise/residue).[70,71] The theoretical sheet thickness of circa 15.5 nm compares well with the thickness determined from the Guinier analysis, especially in the event that the N-terminal triads may not be fully extended due to the potential for lateral movement on the surface (Figure 4.2).

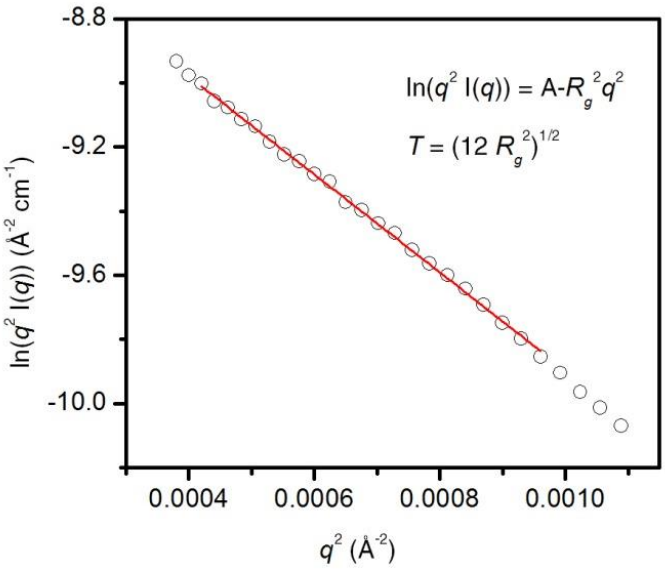

Figure 4.29 Guinier plot of **CP**$^{+}$ nanosheets in aqueous solutions. The red line corresponds to the calculated Guinier fit for a sheet-like form.

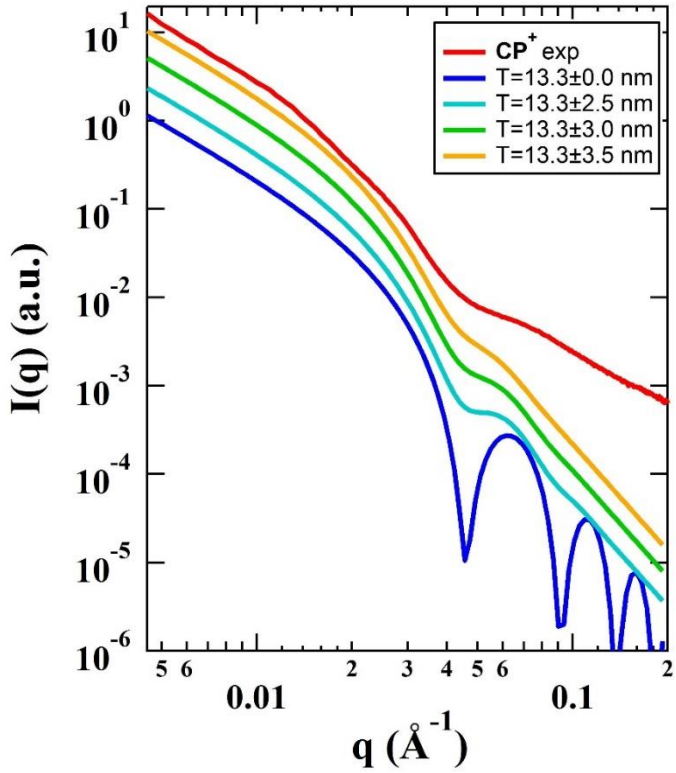

Figure 4.30 Thickness variation analysis for **CP**$^{+}$ nanosheets in aqueous solutions. The red curve is the experimental data, and the others are the simulated SAXS curves using a homogenous disc model with various thickness standard deviation.

A similar situation was observed for the triple-layer sheets, in which the thickness value of 41.4 ± 5.0 nm calculated from the Guinier fit and SAXS curve simulation, was significantly larger than the corresponding value of 34 ± 2.0 nm determined from AFM height measurements (Figure 4.31 and 4.32). Again, this larger value can be rationalized on the basis of the contribution of the surface extensions (5.2 nm) to the core thickness of

the triple-layered nanosheet (circa 36 nm). The measured value of the sheet thickness from SAXS analysis (41.4 ± 5.0 nm) agrees quite well with the calculated value based on the structural model (41.2 nm). In contrast, the Guinier fit and SAXS curve simulation for the **CP**$^{-}$ nanosheets in the presence of calcium nitrate afforded a thickness value of 10.3 ± 2.5 nm (Figure 4.33 and 4.34), which corresponds more closely with the thickness value of 9.9 ± 1.2 nm determined from AFM height measurements than the theoretical value of 15.5 nm for a monolayer sheet with extended (Glu-Hyp-Gly) triads at each surface. This observation suggests that the extended triads may be lying down on the surface of the nanosheet even in the hydrated state, which is presumably due to the coordination of the glutamates by calcium(II) ion.

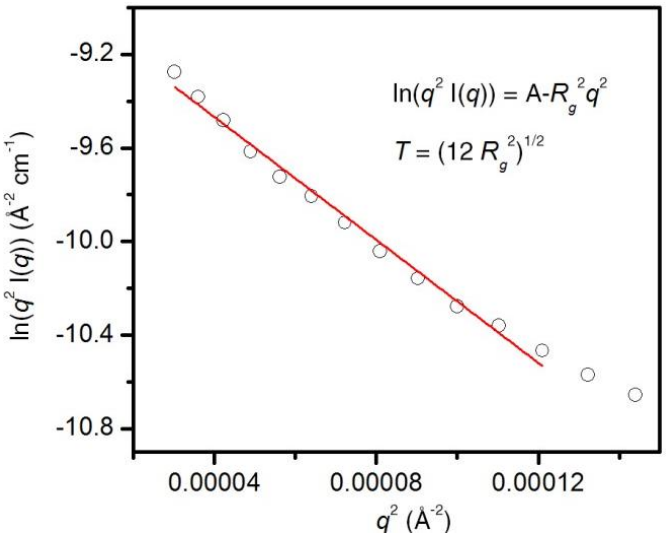

Figure 4.31 Guinier plot of mature **CP**$^{-}$/**CP**$^{+}$/**CP**$^{-}$ triple-layer nanosheets in aqueous solutions at a **CP**$^{-}$:**CP**$^{+}$ concentration ratio of 2:1. The red line corresponds to the calculated Guinier fit for a sheet-like form.

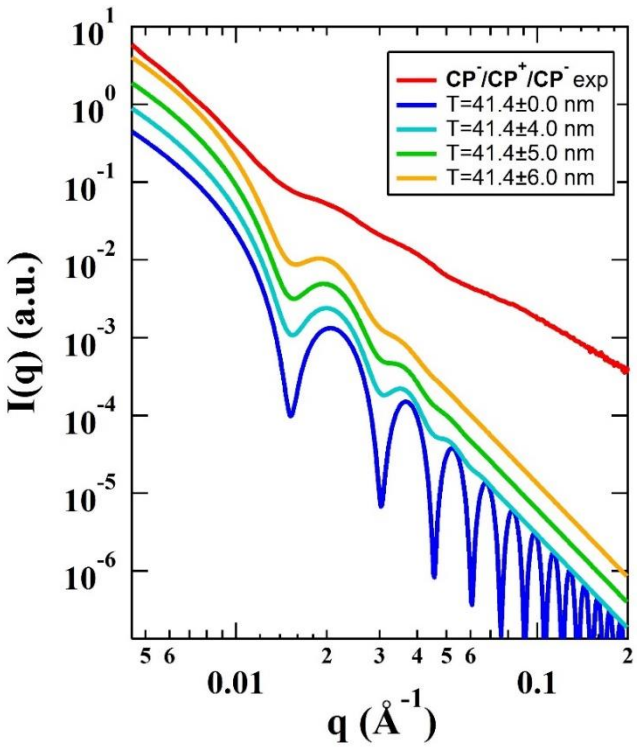

Figure 4.32 Thickness variation analysis for mature **CP**$^{-}$/**CP**$^{+}$/**CP**$^{-}$ triple-layer nanosheets in aqueous solutions, as a **CP**$^{-}$:**CP**$^{+}$ concentration ratio of 2:1.

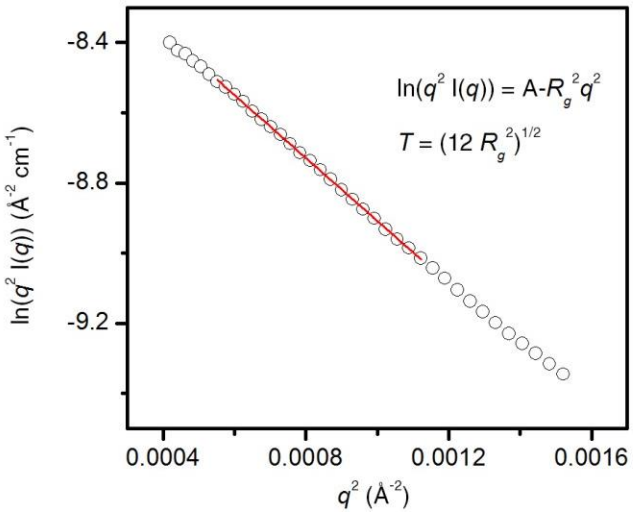

Figure 4.33 Guinier plot of **CP**$^{-}$ nanosheets with Ca^{2+} in aqueous solutions. The red line corresponds to the calculated Guinier fit for a sheet-like form.

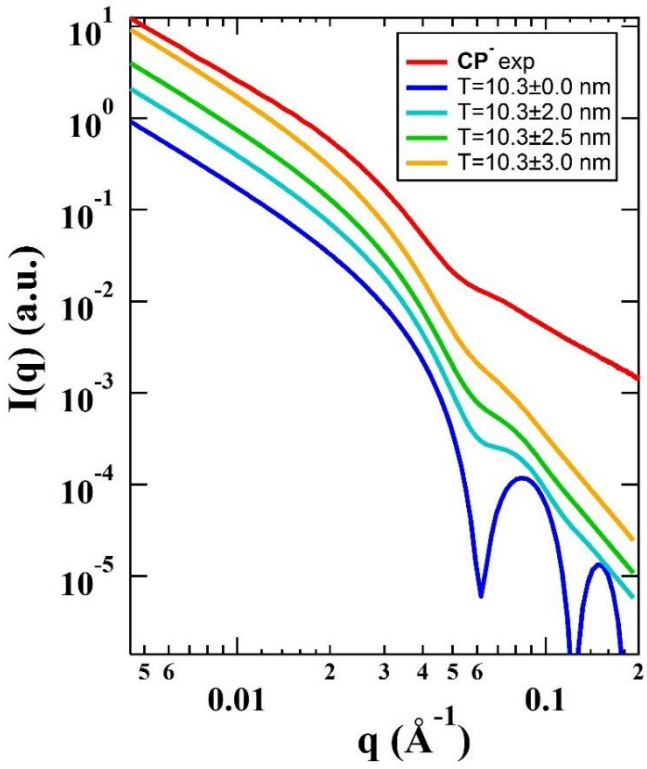

Figure 4.34 Thickness variation analysis for **CP**$^{-}$ nanosheets with Ca^{2+} in aqueous solutions.

In addition to form factor scattering, Bragg diffraction peaks were observed for all three nanosheet specimens in the high momentum transfer (q) region of the scattering curve (Figure 4.35). Three diffraction peaks were observed for the **CP**$^{+}$ and **CP**$^{-}$ nanosheets at q values of 0.305 $Å^{-1}$, 0.430 $Å^{-1}$, and 0.610 $Å^{-1}$, which correspond to d-spacings of 20.6 Å, 14.6 Å, and 10.3 Å. These data suggest that the nearest distance between the centers of triple helices corresponds to 14.6 Å. The geometric relationship between these d-spacings can be interpreted in terms of two tetragonal 2D lattices, a dense tetragonal lattice in the middle portion, and a sparse lattice in the top and bottom portions (Figure 4.36). The former

contributes to diffraction peaks with d-spacings of 14.6 Å and 10.3 Å, while the latter contributes to the d-spacing of 20.6 Å, 14.6 Å and 10.3 Å.

Bragg diffraction peaks were also observed for the (**CP**$^{-}$/**CP**$^{+}$/**CP**$^{-}$) triple-layer sheets at q values corresponding to the d-spacings of 14.6 Å and 10.3 Å, which coincided with those of the monolayer sheets. The peak at a d-spacing of 20.6 Å is expected to be weak in **CP**$^{+}$, **CP**$^{-}$, and **CP**$^{-}$/**CP**$^{+}$/**CP**$^{-}$ nanosheets because the thickness of the sparse lattice at the top and bottom surfaces corresponds to significantly less mass than the core, dense lattice. Presumably, the absence of the 20.6 Å spacing in the SAXS data for the triple-layer nanosheet was due to a weaker signal, as a consequence of a diminished contribution of the sparse surface lattice to the diffraction in comparison to the thicker core lattice.

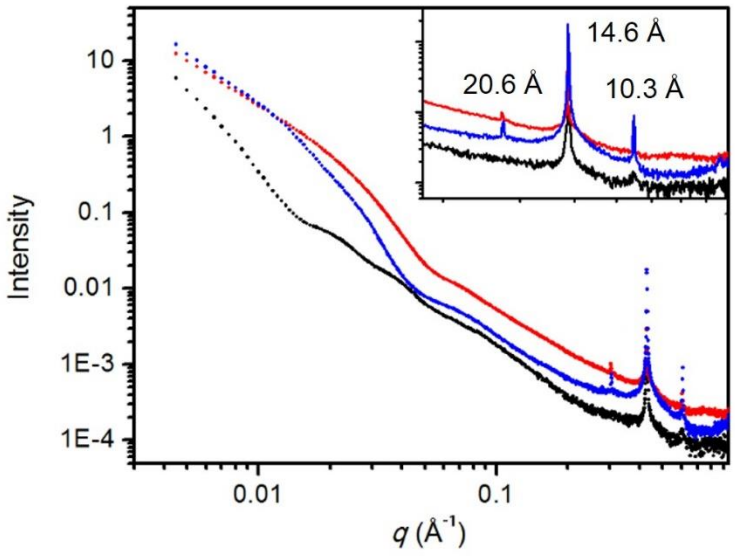

Figure 4.35 Synchrotron SAXS/WAXS scattering profile for **CP**$^{+}$ nanosheets (blue), **CP**$^{-}$ nanosheets with Ca^{2+} (red), and triple-layer (**CP**$^{-}$/**CP**$^{+}$/**CP**$^{-}$) nanosheets (black). Insert: expansion of the diffraction peaks.

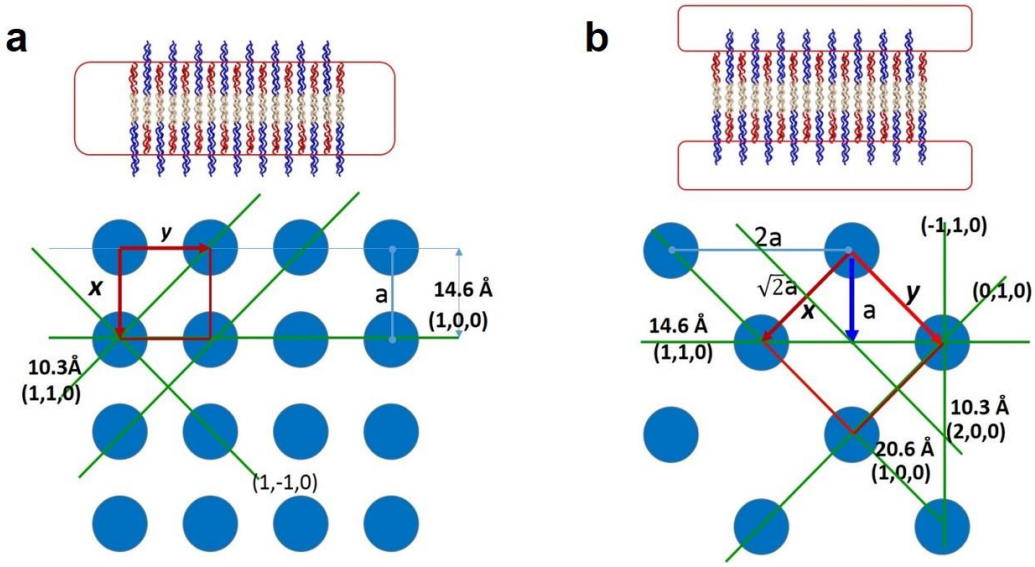

Figure 4.36 The tetragonal lattices formed in the dense core (A) and sparse surface (B) portions of **CP** nanosheets. Red boxes are unit cells for each scenario, and x and y are unit cell vectors. Reflection planes are drawn in green, with notation of (h,k,l).

4.3.9 Electron diffraction measurements

Electron diffraction (ED) analysis on the nanosheets under dry conditions in the TEM instrument confirmed the tetragonal symmetry of the 2D lattice for the **CP**$^{+}$ and triple-layer (**CP**$^{-}$/**CP**$^{+}$/**CP**$^{-}$) nanosheets (Figure 4.37 and 4.38). Sharp diffraction spots were observed at d-spacings of 19.6 Å, 14.0 Å, and 9.89 Å for isolated triple-layer structures, which closely corresponded to the azimuthally averaged lattice spacings determined from SAXS/WAXS measurements. For the **CP**$^{+}$ nanosheets, a single set of diffraction spots was observed for the major diffraction lattice at a d-spacing of 14.2 Å. The diffraction patterns associated with the other lattice spacings were not observed, presumably due to their weaker intensity and the greater sensitivity to beam damage of the monolayer nanosheets.

Fourfold rotational symmetry was observed in all of the electron diffraction patterns, as would be expected for two-dimensional lattices that exhibits tetragonal symmetry. Moreover, the diffraction patterns from the major and minor lattices of the triple-layer nanosheets displayed an angular offset of 45 °, which is consistent the proposed symmetry of the 2D lattice.

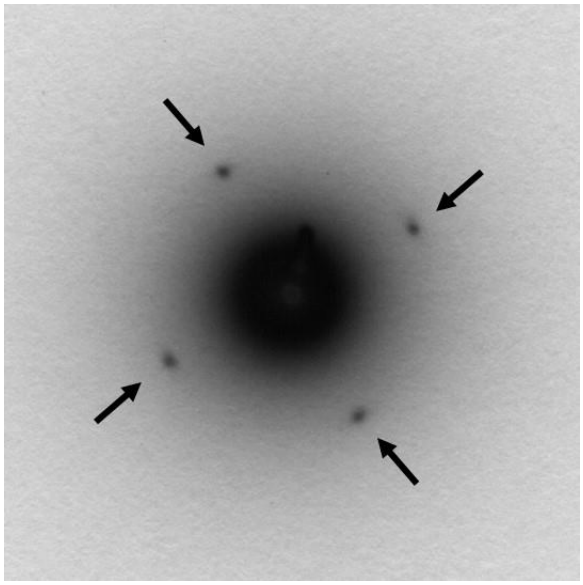

Figure 4.37 Electron diffraction pattern from an isolated **CP**$^{+}$ nanosheet.

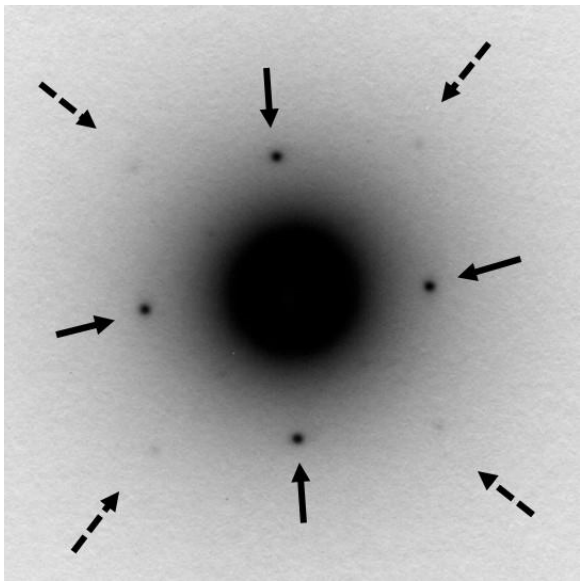

Figure 4.38 Electron diffraction pattern from an isolated mature **CP**$^{-}$/**CP**$^{+}$/**CP**$^{-}$ triple-layer nanosheet.

The SAXS/WAXS measurements and electron diffraction data support a structural model for the **CP-**derived nanosheets that differs from the proposed square 2D lattice of the **NSI** nanosheets.[1] In comparison to the latter system, nanosheets derived from self-assembly of the **CP**$^{+}$ and **CP**$^{-}$ peptides display a longer distance (14.6 Å for **CP**$^{-}$ nanosheets versus 11 Å for the **NSI** nanosheets) for the closest contact between structurally adjacent triple helices in the 2D lattice. This difference in packing density may reflect the different steric requirements necessary to accommodate the 4-(R)-aminoproline and arginine residues in a conformation that would maximize stabilizing electrostatic interactions between adjacent triple helices within the 2D lattices of the **NSI** and the **CP** nanosheets, respectively. Thus, the structure of the charged residues may represent a design parameter that could be implemented to control the underlying dimensions of the 2D lattice of the nanosheets.

Significantly, the lattice spacings associated with the **CP**$^{+}$ monolayer nanosheet and (**CP**$^{-}$/**CP**$^{+}$/**CP**$^{-}$) triple-layer nanosheet coincide almost exactly with each other. Thus, the **CP**$^{+}$ nanosheet can nucleate the controlled growth of the triple-layer nanosheet while preserving the underlying symmetry of the 2D lattice of the template within the nascent layers of **CP**$^{-}$ peptide. Moreover, CD spectropolarimetric analysis of the triple-layer nanosheets indicates similar thermal stability to the **CP**$^{+}$ monolayer nanosheets (Figure 4.39 and 4.40), although the transition is significant broader perhaps due to the mixed composition of the triple-layer nanosheets. In contrast to the aforementioned results, if the **CP**$^{+}$ and **CP**$^{-}$ peptides are mixed (1 mg/mL) and annealed together, structurally and compositionally defined nanosheets are not observed. The CD melting curve is significantly broader than that of the triple-layer nanosheets, presumably as a consequence of compositional and structural heterogeneity (Figure 4.41). TEM analysis of the resultant assemblies indicates the presence of unstructured precipitate rather than well-defined nanosheets (Figure 4.42).

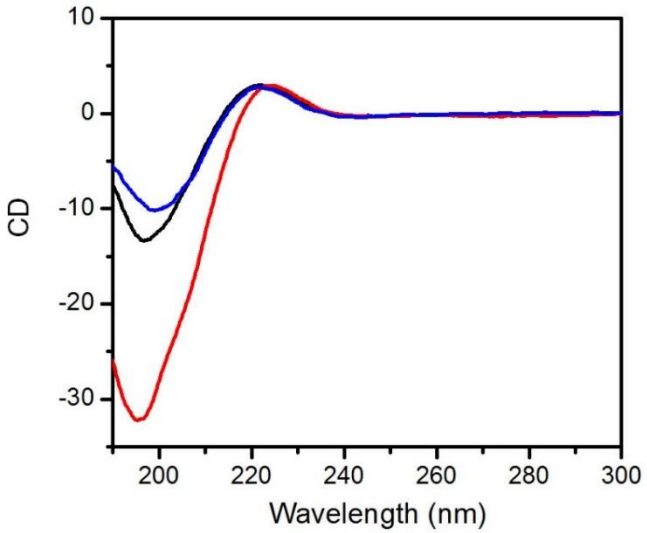

Figure 4.39 CD spectra of aqueous solutions of peptide **CP**$^{-}$ (red), **CP**$^{+}$ (blue), and of **CP**$^{-}$/**CP**$^{+}$/**CP**$^{-}$ triple-layer nanosheets (black).

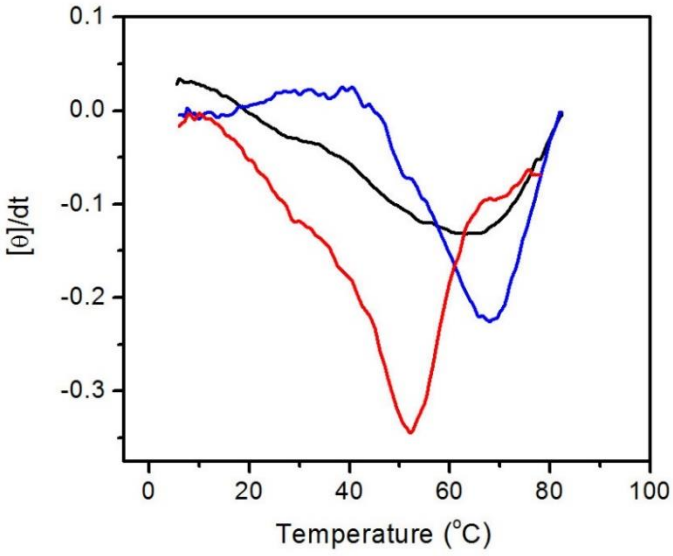

Figure 4.40 First derivative of the CD melting curve derived from monitoring the maximal signal as a function of temperature of aqueous solutions of peptide **CP**$^{-}$ (red), **CP**$^{+}$ (blue), and of **CP**$^{-}$/**CP**$^{+}$/**CP**$^{-}$ triple-layer nanosheets (black).

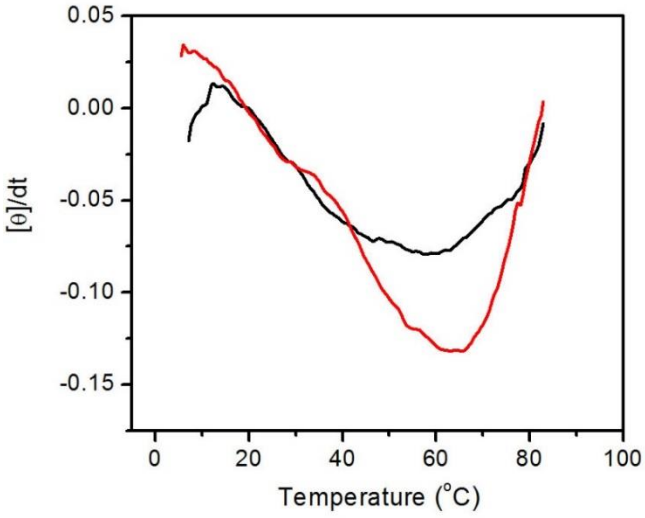

Figure 4.41 First derivative of the CD melting curve derived from monitoring the maximal signal as a function of temperature for a pre-annealed mixture of **CP**$^{-}$ and **CP**$^{+}$ (black), and a solution of **CP**$^{-}$/**CP**$^{+}$/**CP**$^{-}$ triple-layer nanosheets (red).

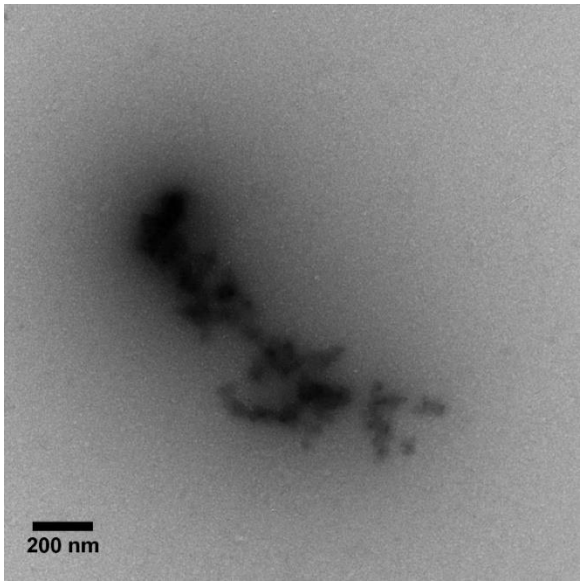

Figure 4.42 TEM image of aggregates from a pre-annealed mixture of **CP**$^{-}$ and **CP**$^{+}$.

4.4 Summary

The fabrication of two-dimensional assemblies presents a significant challenge to current synthetic methods, particularly in terms of structural and compositional control.[18,19] We have described a modified layer-by-layer approach [52] in which nanosheet structures can be assembled with compositional control along the z direction, while maintaining structural order within the 2D lattice. Two collagen-mimetic peptides, **CP**$^{+}$ and **CP**$^{-}$, were designed with macromolecular architectures that comprised an asymmetric distributions of charged triad repeats. If these peptides associated into monolayer nanosheets based on anti-parallel packing of collagen triple helices under mild

conditions in buffered aqueous solution. Based on the structural model for the nanosheets, the charged triad extensions are localized on the surface of the assembly. The excess surface charge prevented further association in the z direction and allowed the nanosheets to be dispersed in aqueous solution.

The positively charged **CP$^+$** monolayer nanosheets assemble more rapidly than the negatively charged **CP$^-$** nanosheets and display greater thermal stability and lateral size. In the absence of calcium ion coordination, the **CP$^-$** peptide forms small nanosheets over a relatively long incubation period. Therefore, the **CP$^+$** monolayer sheets provide an ideal template to nucleate further sheet lamination with the **CP$^-$** peptide. The latent triple helical structure of the charged (Pro-Arg-Gly)$_3$ extensions at the surface of the more stable **CP$^+$** nanosheet is realized in the presence of the electrostatically complementary **CP$^-$** peptide. The resultant interfacial interactions promoted the growth of structurally ordered monolayers derived from the **CP$^-$** peptide at both surfaces of the original **CP$^+$** nanosheet template. Subsequent growth in the z direction is inhibited due to the excess negative charge present at either surface of the mature assemblies. In theory, further growth of the layered nanostructure could occur by successive addition of positively charged **CP$^+$** and negatively charged **CP$^-$** peptides to the triple-layer structure. In practice, the **CP$^+$** peptide assembles rapidly in the absence of template, which results in a complex mixture of monolayer and multi-layer assemblies in the presence of preformed (**CP$^-$**/**CP$^+$**/**CP$^-$**) triple-layer nanosheets.

However, as the self-assembly of the **CP$^-$D$_3$** peptide demonstrates, nanosheet formation can strongly depend on the sequence on the triad extensions, in ways that may be difficult to predict a priori. These results suggest that it may be possible to find positively

charged amino acids that undergo slow self-assembly into nanosheets. Collagen-mimetic peptides that display this self-assembly behavior would be useful substrates for the fabrication of highly laminated nanosheet assemblies with compositional control over an extended length scale in the z dimension. Our experimental results also demonstrate that electrostatic deposition can occur within a given structural context, i.e., the collagen triple helix, which provides a mechanism for assembly of structurally defined 2D nanostructures. This approach has the potential to be extended to peptide-based materials derived from other structural motifs, if suitable noncovalent interactions can be introduced at structurally informed positions within the corresponding amino acid sequence.[72-80]

4.5 Materials and methods

Materials. Chemical reagents were purchased from Sigma Aldrich Chemical Co. (St. Louis, MO) or Anaspec, Inc. (Fremont, CA), unless otherwise noted. Fmoc-Gly-PEG-PS solid phase synthesis resin was purchased from Applied Biosystems, Inc. (Foster City, CA). Template stripped gold chips were purchased from AMS Biotechnology, LLC. (Cambridge, MA).

Peptide Synthesis. Peptides **CP$^+$**, **CP$^-$**, and **CP$^-$D$_3$** were synthesized as the N-amino, C-acid derivatives on a CEM Liberty microwave-assisted synthesizer using the Fmoc-Gly-PEG-PS resin as the solid support. Standard Fmoc protection chemistry was employed with coupling cycles based on HBTU/DIEA-mediated activation protocols and base induced deprotection (20% piperidine in DMF with 0.1 M HOBt) of the Fmoc group. Crude peptides were purified by reverse phase HPLC on a C18 column. The target fractions were collected and lyophilized, followed by purity analysis through MALDI mass spectrometry and analytical HPLC (Figure 4.43-4.48). Peptides were dialyzed against deionized water (MWCO = 2000 Da) and lyophilized for long term storage at -20 ℃. Peptides were dissolved in MES buffer (20 mM, pH 6.0) at the desired concentration. Solution concentrations were determined from the measured mass of the respective peptides. Samples were thermally annealed at 85 °C for 45 min, and gradually cooled to ambient temperature.

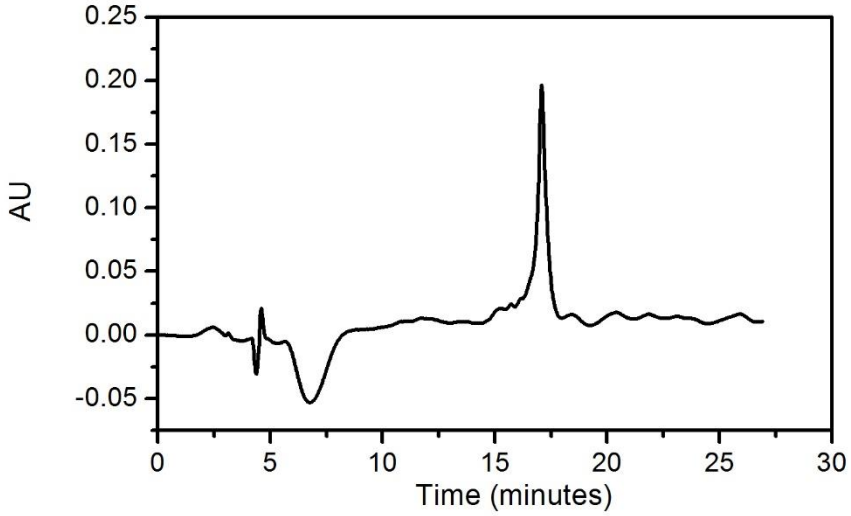

.

Figure 4.43 Analytical HPLC trace of a purified peptide **CP**$^{+}$.

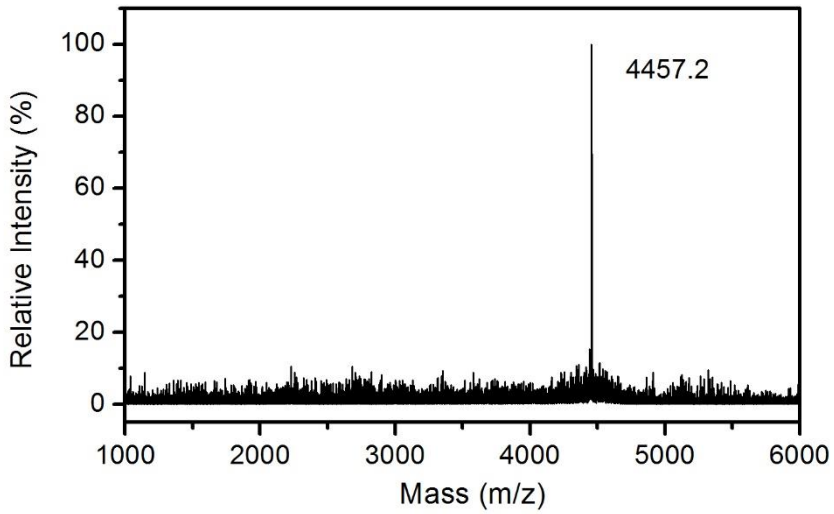

Figure 4.44 MALDI-TOF mass spectrum of a purified peptide **CP**$^{+}$.

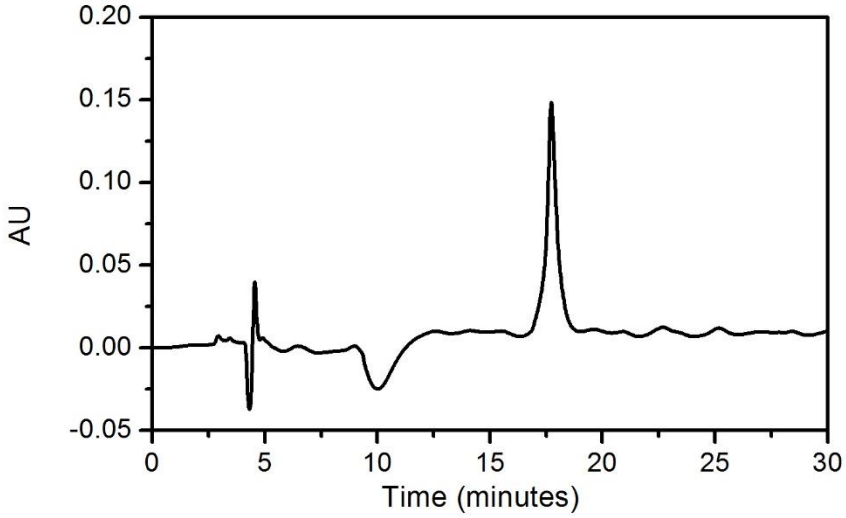

Figure 4.45 Analytical HPLC trace of a purified peptide **CP**$^{-}$.

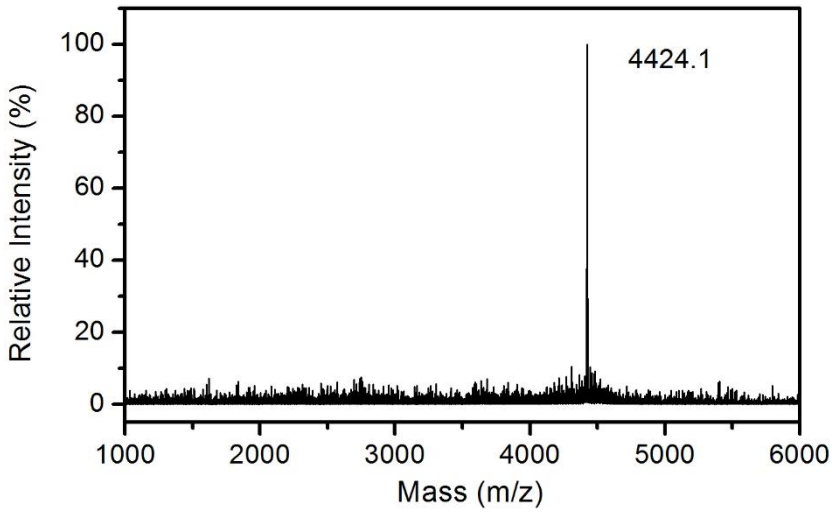

Figure 4.46 MALDI-TOF mass spectrum of a purified peptide **CP**$^{-}$.

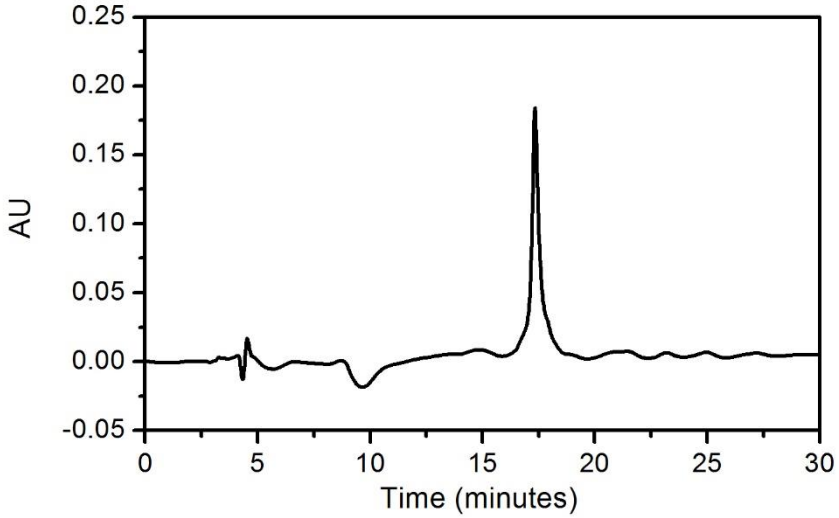

Figure 4.47 Analytical HPLC trace of a purified peptide **CP^{-}D$_3$**.

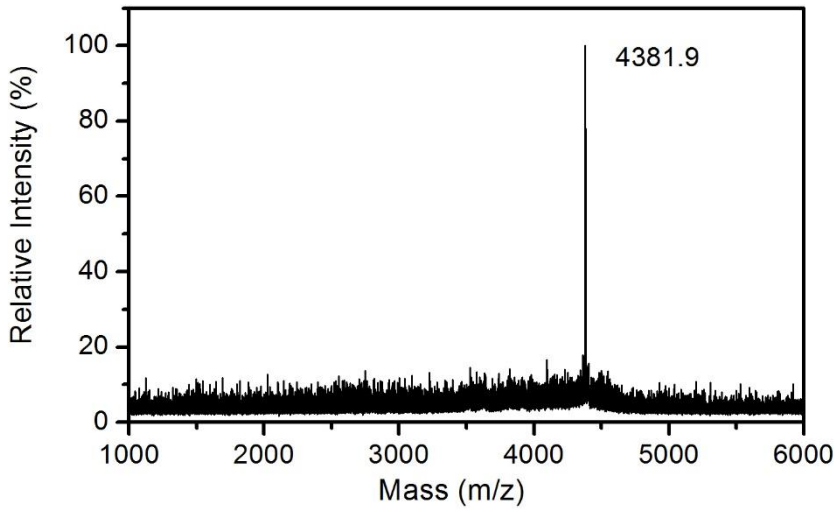

Figure 4.48 MALDI-TOF mass spectrum of a purified peptide **CP^{-}D$_3$**.

Circular Dichroism Spectropolarimetry. CD measurements were performed on a Jasco J-810 CD spectropolarimetry in 0.10 mm quartz cells using samples prepared at the desired concentration in MES buffer (20 mM, pH 6.0). Spectra were recorded from 300

to 190 nm at a scanning rate of 100 nm/min and a resolution of 0.5 nm. CD melting experiments were performed in the temperature range from 5 ℃ to 85 ℃ at a heating rate of 0.1 ℃/min. The intensity of the CD signal at 223 nm was monitored as a function of temperature. Melting temperatures were obtained from the first derivative of the melting curves.

Transmission Electron Microscopy. TEM images were recorded on a Hitachi H7500 microscope with an accelerating voltage of 75 kV. Aqueous peptide solutions were deposited onto 200 mesh carbon coated copper grids (Electron Microscopy Sciences), allowing for 1 min for adsorption of the specimen. Excess liquid was wicked away using filter papers, and the grid was stained with 1 % uranyl acetate for 45 sec. Excess stain solution was wicked away and sample grids were dried in vacuo prior to TEM measurement.

For the binding assay with gold nanoparticles, the supernatant solution from the nanosheet specimens was exchanged with an equivalent volume of fresh MES buffer (20 mM, pH 6.0) immediately prior to sample preparation in order to remove unassociated peptides. The solutions of either cationic or anionic gold nanoparticles were diluted 10 times using MES buffer (0.5 mM, pH 6.0). An aliquot (8 μL) of the diluted gold nanoparticle solutions was added to the nanosheet solution, which was incubated in situ for 30 min at ambient temperature. Specimens were deposited on the TEM grids as described above. The sample grids were washed three times using MES buffer (0.5 mM, pH 6.0), air-dried for 30 min, and imaged in the TEM instrument.

Electron Diffraction. Electron diffraction lattice patterns were recorded on the Hitachi H-7500 transmission electron microscopy using an accelerating voltage of 40 kV. Specimens were prepared as described above for TEM measurements. A camera length of 1.5 m was employed to expose the small reciprocal lattice. The d-spacings were calculated using the equation: $d = \lambda L/R$, in which λ is the electron wavelength, L denotes the camera length, and R represents the distances of diffraction signals. An aluminum polycrystalline standard (Ted Pella, Inc.) was used to calibrate the camera length.

Atomic Force Microscopy. Tapping mode AFM scans were performed on a JEOL-4200 instrument, using a silicon AFM tip with a force constant at 5.4-16 N/m. Aqueous solutions of nanosheet specimens in MES buffer (0.5 mM, pH 6.0) were deposited onto a freshly cleaved mica substrate for 5 min, and dried under a flow of nitrogen gas. The z-axis was calibrated immediately prior to AFM height measurements using a silicon wafer block test grating with step heights of 20 ± 1 nm (TGZ-20 from Ted Pella, Inc.).

Electrostatic Force Microscopy. The ambient EFM measurements were performed on a Park System XE-100, using Pt-Ir coated, electrically conductive cantilevers with a force constant of 2.8 N/m. Aqueous solutions of nanosheets were diluted using MES buffer (0.5 mM, pH 6.0), deposited onto the atomically flat gold substrates (Amsbio, LLC), and air dried overnight. A +2 V AC bias was applied to the cantilever to map the charge distribution in both EFM amplitude and phase modes.

Zeta Potential Measurements. Zeta potential measurements were obtained on a Malvern Zetasizer Nano Z, equipped with a 4 mW, He-Ne laser at 633 nm. The Zetasizer Nano Z uses the laser doppler micro-electrophoresis to measure zeta potential. Aqueous

solutions of nanosheets were diluted to 0.1 mg/mL in MES buffer (20 mM, pH 6.0) at ambient temperature immediately prior to data acquisition.

Small- and Wide-Angle X-ray Scattering Measurements. Synchrotron SAXS/WAXS measurements were performed at the 12-ID-B beamline of Advanced Photon Sources at Argonne National Laboratory, using the methods described previously.[1] SAXS/WAXS data were acquired on aqueous solutions of peptide nanosheets at a concentration of 4 mg/mL in MES buffer (20 mM, pH 6.0) at 25 ℃. A quartz capillary flow cell (1.5 mm diameter) was employed to prevent radiation damage. Twenty images were collected for each sample and buffer. The 2-D scattering images were converted to 1-D SAXS curves through azimuthally averaging after solid angle correction and then normalizing with the intensity of the transmitted x-ray beam, using the software package at beam-line 12ID-B. The 1-D curves of the samples were averaged and subtracted with the background measured from the corresponding buffers.

Detailed analysis of scattering data of SAXS/WAXS in terms of a 2D disc model (illustrated in figure 4.30, 4.32, 4.34): in figure 4.30 for example, the red curve is the experimental data, and the others are the simulated SAXS curves using a homogenous disc model with various thickness standard deviation. The radius of disc was set as 5000 nm. The thickness through the disc is assumed to follow a Gaussian distribution. The thickness is written as (the mean thickness) ± (standard deviation), where the mean thickness can be obtained from Guinier fit, and the standard deviation is the standard deviation of Gaussian distribution. The positions of peaks and/or valleys of the SAXS curve also indicate the sheet thickness. The good match between experimental data and simulated curves of the

valley position between 0.04 and 0.05 $Å^{-1}$ suggests the thickness value obtained from Guinier fit is correct. All curves are vertically offset for clarity, which would otherwise be superimposed in low q range. As demonstrated in the figure, thickness variation attenuates and damps the oscillation in the curves. The slope discrepancy in q of 0.03-0.2 $Å^{-1}$ between experimental data and simulated curves arises from the non-homogenous electron density in the nanosheet, which raises the baseline and further damps the oscillation. Based on this analysis, the thickness of $\mathbf{CP}^{+}$ nanosheets is 13.3 ± 3.0 nm.

Detailed analysis of the diffraction data in terms of a structural model (illustrated in figure 4.36): Red boxes are unit cells for each scenario, and $\boldsymbol{x}$ and $\boldsymbol{y}$ are unit cell vectors. Reflection planes are drawn in green, with notation of (h,k,l). Length a = 14.6 Å. A dense tetragonal packing in the core layer, in which $|\boldsymbol{x}| = |\boldsymbol{y}| = a$. The triple helices seem to scatter similarly under x-ray illumination, presumably due to a same/similar form factor. This middle portion contributes two diffraction peaks with d-spacing of 14.6 Å and 10.3 Å. The d-spacing of 14.6 Å is associated with planes (1,0,0), (0,1,0), (-1,0,0), and (0,-1,0) and the d-spacing of 10.3 Å is associated with planes (1,1,0), (-1,-1,0), (-1,1,0), and (1,-1,0). (B) Sparse packing of triple helices in the top and bottom surface layers, in which $|\boldsymbol{x}| = |\boldsymbol{y}| = 1.414a$. The top and bottom portions contribute three diffraction peaks with *d*-spacings of 20.6 Å, 14.6 Å and 10.3 Å. The d-spacing of 20.6 Å is associated with planes (1,0,0), (0,1,0), (-1,0,0), and (0,-1,0). The d-spacing of 14.6 Å is associated with planes (1,1,0), (-1,-1,0), (-1,1,0), and (1,-1,0). The d-spacing of 10.3 Å is associated with planes (2,0,0), (0,2,0), (-2,0,0), and (0,-2,0).

4.6 Reference

(1) Jiang, T.; Xu, C.; Liu, Y.; Liu, Z.; Wall, J. S.; Zuo, X.; Lian, T.; Salaita, K.; Ni, C.; Pochan, D.; Conticello, V. P. *J. Am. Chem. Soc.* **2014**, *136*, 4300-4308.

(2) Jiang, T.; Xu, C.; Zuo, X.; Conticello, V. P. *Angew. Chem., Int. Ed.* **2014**, *53*, 8367-8371.

(3) Przybyla, D. E.; Chmielewski, J. *J. Am. Chem. Soc.* **2010**, *132*, 7866-7867.

(4) Przybyla, D. E.; Rubert Perez, C. M.; Gleaton, J.; Nandwana, V.; Chmielewski, J. *J. Am. Chem. Soc.* **2013**, *135*, 3418-3422.

(5) Hughes, M.; Xu, H.; Frederix, P. W. J. M.; Smith, A. M.; Hunt, N. T.; Tuttle, T.; Kinloch, I. A.; Ulijn, R. V. *Soft Matter.* **2011**, 10032-10038.

(6) Govindaraju, T.; Pandeeswar, M.; Jayaramulu, K.; Jaipuria, G.; Atreya, H. S. *Supramol. Chem.* **2011**, *23*, 487-492.

(7) Hamley, I. W.; Dehsorkhi, A.; Castelletto, V. *Chem. Commun.* **2013**, *49*, 1850-1852.

(8) Xu, F.; Khan, I. J.; McGuinness, K.; Parmar, A. S.; Silva, T.; Murthy, N. S.; Nanda, V. *J. Am. Chem. Soc.* **2013**, *135*, 18762-18765.

(9) Jang, H. S.; Lee, J. H.; Park, Y. S.; Kim, Y. O.; Park, J.; Yang, T. Y.; Jin, K.; Lee, J.; Park, S.; You, J. M.; Jeong, K. W.; Shin, A.; Oh, I. S.; Kwon, M. K.; Kim, Y. I.; Cho, H. H.; Han, H. N.; Kim, Y.; Chang, Y. H.; Paik, S. R.; Nam, K. T.; Lee, Y. S. *Nat. Commun.* **2014**, *5*, 3665.

(10) McGuinness, K.; Khan, I. J.; Nanda, V. *ACS Nano* **2014**, *8*, 12514-12523.

(11) Brodin, J. D.; Ambroggio, X. I.; Tang, C.; Parent, K. N.; Baker, T. S.; Tezcan, F. A. *Nat. Chem.* **2012**, *4*, 375-382.

(12) Brodin, J. D.; Carr, J. R.; Sontz, P. A.; Tezcan, F. A. *Proc. Natl. Acad. Sci. U. S. A.* **2014**, *111*, 2897-2902.

(13) Nam, K. T.; Shelby, S. A.; Choi, P. H.; Marciel, A. B.; Chen, R.; Tan, L.; Chu, T. K.; Mesch, R. A.; Lee, B. C.; Connolly, M. D.; Kisielowski, C.; Zuckermann, R. N. *Nat. Mater.* **2010**, *9*, 454-460.

(14) Sanii, B.; Kudirka, R.; Cho, A.; Venkateswaran, N.; Olivier, G. K.; Olson, A. M.; Tran, H.; Harada, R. M.; Tan, L.; Zuckermann, R. N. *J. Am. Chem. Soc.* **2011**, *133*, 20808-20815.

(15) Kudirka, R.; Tran, H.; Sanii, B.; Nam, K. T.; Choi, P. H.; Venkateswaran, N.; Chen, R.; Whitelam, S.; Zuckermann, R. N. *Biopolymers* **2011**, *96*, 586-595.

(16) Robertson, E. J.; Oliver, G. K.; Qian, M.; Proulx, C.; Zuckermann, R. N.; Richmond, G. L. *Proc. Natl. Acad. Sci. U. S. A.* **2014**, *111*, 13284-13289.

(17) Olivier, G. K.; Cho, A.; Sanii, B.; Connolly, M. D.; Tran, H.; Zuckermann, R. N. *ACS Nano* **2013**, *7*, 9276-9286.

(18) Govindaraju, T.; Avinash, M. B. *Nanoscale* **2012**, *4*, 6102-6117.

(19) Ariga, K.; Ji, Q.; Hill, J. P.; Bando, Y.; Aono, M. *NPG Asia Mater.* **2012**, *4*, e17.

(20) Babu, I. R.; Ganesh, K. N. *J. Am. Chem. Soc.* **2001**, *123*, 2079-2080.

(21) Umashankara, M.; Babu, I. R.; Ganesh, K. N. *Chem. Commun.* **2003**, 2606-2607.

(22) Siebler, C.; Erdmann, R. S.; Wennemers, H. *Angew. Chem., Int. Ed.* **2014**, *53*, 10340-10344.

(23) Erdmann, R. S.; Wennemers, H. *Angew. Chem., Int. Ed.* **2011**, *50*, 6835-6838.

(24) Kuemin, M.; Nagel, Y. A.; Schweizer, S.; Monnard, F. W.; Ochsenfeld, C.; Wennemers, H. *Angew. Chem., Int. Ed.* **2010**, *49*, 6324-6327.

(25) Siebler, C.; Trapp, N.; Wennemers, H. *J. Pept. Sci.* **2015**, *21*, 208-211.

(26) Rele, S.; Song, Y. H.; Apkarian, R. P.; Qu, Z.; Conticello, V. P.; Chaikof, E. L. *J. Am. Chem. Soc.* **2007**, *129*, 14780-14787.

(27) Ramshaw, J. A.; Shah, N. K.; Brodsky, B. *J. Struct. Biol.* **1998**, *122*, 86-91.

(28) Jalan, A. A.; Hartgerink, J. D. *Curr. Opin. Chem. Biol.* **2013**, *17*, 960-967.

(29) Keshwani, N.; Banerjee, S.; Brodsky, B.; Makhatadze, G. I. *Biophys. J.* **2013**, *105*, 1681-1688.

(30) Persikov, A. V.; Ramshaw, J. A.; Kirkpatrick, A.; Brodsky, B. *Biochemistry* **2005**, *44*, 1414-1422.

(31) Persikov, A. V.; Ramshaw, J. A. M.; Kirkpatrick, A.; Brodsky, B. *J. Mol. Biol.* **2002**, *316*, 385-394.

(32) Kramer, R. Z.; Venugopal, M. G.; Bella, J.; Mayville, P.; Brodsky, B.; Berman, H. M. *J. Mol. Biol.* **2000**, *301*, 1191-1205.

(33) Venugopal, M. G.; Ramshaw, J. A.; Braswell, E.; Zhu, D.; Brodsky, B. *Biochemistry* **1994**, *33*, 7948-7956.

(34) Jalan, A. A.; Demeler, B.; Hartgerink, J. D. *J. Am. Chem. Soc.* **2013**, *135*, 6014-6017.

(35) Fallas, J. A.; Hartgerink, J. D. *Nat. Commun.* **2012**, *3*, 1087.

(36) Fallas, J. A.; Lee, M. A.; Jalan, A. A.; Hartgerink, J. D. *J. Am. Chem. Soc.* **2012**, *134*, 1430-1433.

(37) Fallas, J. A.; Dong, J.; Tao, Y. J.; Hartgerink, J. D. *J. Biol. Chem.* **2012**, *287*, 8039-8047.

(38) O'Leary, L. E.; Fallas, J. A.; Hartgerink, J. D. *J. Am. Chem. Soc.* **2011**, *133*, 5432-5443.

(39) Russell, L. E.; Fallas, J. A.; Hartgerink, J. D. *J. Am. Chem. Soc.* **2010**, *132*, 3242-3243.

(40) Fallas, J. A.; Gauba, V.; Hartgerink, J. D. *J. Biol. Chem.* **2009**, *284*, 26851-26859.

(41) Gauba, V.; Hartgerink, J. D. *J. Am. Chem. Soc.* **2008**, *130*, 7509-7515.

(42) Gauba, V.; Hartgerink, J. D. *J. Am. Chem. Soc.* **2007**, *129*, 15034-15041.

(43) Gauba, V.; Hartgerink, J. D. *J. Am. Chem. Soc.* **2007**, *129*, 2683-2690.

(44) Parmar, A. S.; Joshi, M.; Nosker, P. L.; Hasan, N. F.; Nanda, V. *Biomolecules* **2013**, *3*, 986-996.

(45) Giddu, S.; Xu, F.; Nanda, V. *Proteins* **2013**, *81*, 386-393.

(46) Xu, F.; Zahid, S.; Silva, T.; Nanda, V. *J. Am. Chem. Soc.* **2011**, *133*, 15260-15263.

(47) Xu, F.; Zhang, L.; Koder, R. L.; Nanda, V. *Biochemistry* **2010**, *49*, 2307-2316.

(48) Sarkar, B.; O'Leary, L. E.; Hartgerink, J. D. *J. Am. Chem. Soc.* **2014**, *136*, 14417-14424.

(49) Jalan, A. A.; Jochim, K. A.; Hartgerink, J. D. *J. Am. Chem. Soc.* **2014**, *136*, 7535-7538.

(50) O'Leary, L. E.; Fallas, J. A.; Bakota, E. L.; Kang, M. K.; Hartgerink, J. D. *Nat. Chem.* **2011**, *3*, 821-828.

(51) Xu, F.; Li, J.; Jain, V.; Tu, R. S.; Huang, Q.; Nanda, V. *J. Am. Chem. Soc.* **2012**, *134*, 47-50.

(52) Decher, G. *Science* **1997**, *277*, 1232-1237.

(53) Persikov, A. V.; Ramshaw, J. A.; Brodsky, B. *Biopolymers* **2000**, *55*, 436-450.

(54) Chan, V. C.; Ramshaw, J. A.; Kirkpatrick, A.; Beck, K.; Brodsky, B. *J. Biol. Chem.* **1997**, *272*, 31441-31446.

(55) Shah, N. K.; Ramshaw, J. A.; Kirkpatrick, A.; Shah, C.; Brodsky, B. *Biochemistry* **1996**, *35*, 10262-10268.

(56) Yang, W.; Chan, V. C.; Kirkpatrick, A.; Ramshaw, J. A.; Brodsky, B. *J. Biol. Chem.* **1997**, *272*, 28837-28840.

(57) Okuyama, K.; Haga, M.; Noguchi, K.; Tanaka, T. *Biopolymers* **2014**, *101*, 1000-1009.

(58) Lumb, R. F.; Martell, A. E. *J. Phys. Chem.* **1953**, *57*, 690-693.

(59) Zhou, Y.; Xue, S.; Yang, J. J. *Metallomics* **2013**, *5*, 29-42.

(60) Okuyama, K.; Kawaguchi, T.; Shimura, M.; Noguchi, K.; Mizuno, K.; Bachinger, H. P. *Biopolymers* **2013**, *99*, 436-447.

(61) Malvankar, N. S.; Yalcin, S. E.; Tuominen, M. T.; Lovley, D. R. *Nat. Nanotechnol.* **2014**, *9*, 1012-1017.

(62) Du, H.; Li, D.; Wang, Y.; Wang, C.; Zhang, D.; Yang, Y. L.; Wang, C. *J. Phys. Chem. B* **2013**, *117*, 9895-9899.

(63) Baumann, R. P.; Eussner, J.; Hampp, N. *Phys. Chem. Chem. Phys.* **2011**, *13*, 21375-21382.

(64) Oh, Y. J.; Jo, W.; Kim, S.; Park, S.; Kim, Y. S. *Nanotechnology* **2008**, *19*, 365302.

(65) Li, S.; Sidorov, A. N.; Mehta, A. K.; Bisignano, A. J.; Das, D.; Childers, W. S.; Schuler, E.; Jiang, Z.; Orlando, T. M.; Berland, K.; Lynn, D. G. *Biochemistry* **2014**, *53*, 4225-4227.

(66) Lee, G.; Lee, W.; Lee, H.; Lee, S. W.; Yoon, D. S.; Eom, K.; Kwon, T. *Appl. Phys. Lett.* **2012**, *101*, 043703.

(67) Clausen, C. H.; Dimaki, M.; Panagos, S. P.; Kasotakis, E.; Mitraki, A.; Svendsen, W. E.; Castillo-Leon, J. *Scanning* **2011**, *33*, 201-207.

(68) Clausen, C. H.; Jensen, J.; Castillo, J.; Dimaki, M.; Svendsen, W. E. *Nano Lett.* **2008**, *8*, 4066-4069.

(69) Porod, G. *Small angle X-ray Scattering*; Academic Press: New York, 1982.

(70) Okuyama, K.; Xu, X.; Iguchi, M.; Noguchi, K. *Biopolymers* **2006**, *84*, 181-191.

(71) Okuyama, K. *Connect. Tissue Res.* **2008**, *49*, 299-310.

(72) Xu, C.; Liu, R.; Mehta, A. K.; Guerrero-Ferreira, R. C.; Wright, E. R.; Dunin-Horkawicz, S.; Morris, K.; Serpell, L. C.; Zuo, X.; Wall, J. S.; Conticello, V. P. *J. Am. Chem. Soc.* **2013**, *135*, 15565-15578.

(73) Pandya, M. J.; Spooner, G. M.; Sunde, M.; Thorpe, J. R.; Rodger, A.; Woolfson, D. N. *Biochemistry* **2000**, *39*, 8728-8734.

(74) Ryadnov, M. G.; Woolfson, D. N. *Nat. Mater.* **2003**, *2*, 329-332.

(75) Ryadnov, M. G.; Woolfson, D. N. *Angew. Chem., Int. Ed.* **2003**, *42*, 3021-3023.

(76) Papapostolou, D.; Smith, A. M.; Atkins, E. D.; Oliver, S. J.; Ryadnov, M. G.; Serpell, L. C.; Woolfson, D. N. *Proc. Natl. Acad. Sci. U. S. A.* **2007**, *104*, 10853-10858.

(77) Sharp, T. H.; Bruning, M.; Mantell, J.; Sessions, R. B.; Thomson, A. R.; Zaccai, N. R.; Brady, R. L.; Verkade, P.; Woolfson, D. N. *Proc. Natl. Acad. Sci. U. S. A.* **2012**, *109*, 13266-13271.

(78) Zhang, S.; Holmes, T.; Lockshin, C.; Rich, A. *Proc. Natl. Acad. Sci. U. S. A.* **1993**, *90*, 3334-3338.

(79) Marini, D. M.; Hwang, W.; Lauffenburger, D. A.; Zhang, S. G.; Kamm, R. D. *Nano Lett.* **2002**, *2*, 295-299.

(80) Swanekamp, R. J.; DiMaio, J. T. M.; Bowerman, C. J.; Nilsson, B. L. *J. Am. Chem. Soc.* **2012**, *134*, 5556-5559.

5 Conclusion and outlook

5.1 Conclusion

The purpose of the study in the dissertation is to explore practical strategies for creating custom structures utilizing what nature offers. Due to the relatively more clear sequence-structure correlations for natural collagens, synthetic collagen triple helix has been employed as a building block for designing higher order assemblies.[1] Based on the this structural motif, we introduced charged residues into collagen-mimetic peptides, which effectively directed peptide self-assembly into a series of two-dimensional structures. The studies described here span three major topics. The first one is recoding fibril-forming peptides for nanosheet formation.[2] In chapter two, the construction of peptide nanosheets was described, which involved reprogramming intermolecular interfaces of a fibril-forming peptide. This study represented a design rubric for constructing two-dimensional structures by enforcing a side-by-side packing among protomers. The packing mechanism allowed for chemical modifications on sheet surfaces, which would afford peptide-based functional devices. However, nanosheets in chapter two varied greatly in size at both lateral and vertical directions, which would jeopardize future applications. In the second topic, this concern was addressed by constructing a using molecular frustration.[3] In chapter three, an energy penalty was applied to the nanosheet system, where a local structural distortion was introduced to a sheet-forming peptide. This integrated destabilizing factor resulted in formation of nanosheets with narrow dispersity in size. The studies on those nanosheets endowed us with a maturing ability to move one step forward to pursue more complex self-assembly systems. In the third topic, a rational design of a two-component

assemblies was described in chapter four.[4] A predictable triple-layer structure was achieved from self-assembly of two collagen-mimetic peptides, with compositional and structural control in the vertical directions.

5.2 Future directions

Due to the large Protein Data Bank and the aid of computer simulations, designing and predicting simple structures from first principles is possible nowadays.[5] However, there is still a long way to go to reach what nature has made in cells. For example, many self-assembly systems in cells are dynamic, out-of-equilibrium systems. We believe that constructing dynamic self-assembly systems in vitro will be necessary to decode programming languages of natural self-assemblies, and maximize the potential of self-assembly as a tool to make structures and functions[6]. In our work, it will be fascinating to create non-equilibrium peptide systems that a reversible switch between one- and two-dimensional peptide self-assemblies can be regulated by external stimuli. In cells, nature offers an enormous variety of sophisticated systems that are assembled from multiple components. It will be intriguing to create complex and multicomponent structures consisting of distinct building blocks. The construction of the triple-layer structure in our studies offers a promising strategy (layer-by-layer growth) to achieve the goal. It will be interesting to design a **CP**$^{+}$ analogue with a slower sheet-forming rate. Using the peptides with different sheet-forming kinetics, it may be possible to go beyond three layers, and construct thicker structures containing five, seven, and nine layers of peptides. We envision that it may be an attractive way to build three-dimensional multicomponent architectures based on two-dimensional building blocks.

5.3 Reference

(1) Yu, S. M.; Li, Y.; Kim, D. *Soft Matter.* **2011**, *7*, 7927-7938.

(2) Jiang, T.; Xu, C.; Liu, Y.; Liu, Z.; Wall, J. S.; Zuo, X.; Lian, T.; Salaita, K.; Ni, C.; Pochan, D.; Conticello, V. P. *J. Am. Chem. Soc.* **2014**, *136*, 4300-4308.

(3) Jiang, T.; Xu, C.; Zuo, X.; Conticello, V. P. *Angew. Chem., Int. Ed.* **2014**, *53*, 8367-8371.

(4) Jiang, T.; Vail, O. A.; Jiang, Z.; Zuo, X.; Conticello, V. P. *J. Am. Chem. Soc.* **2015**, *137*, 7793-7802.

(5) Dill, K. A.; MacCallum, J. L. *Science* **2012**, *338*, 1042-1046.

(6) Whitesides, G. M.; Boncheva, M. *Proc. Natl. Acad. Sci. U. S. A.* **2002**, *99*, 4769-4774.